LBL-36087
UC-413

Lawrence Berkeley Laboratory
UNIVERSITY OF CALIFORNIA

Heavy Residues from Very Mass Asymmetric Heavy Ion Reactions

K.A. Hanold
(Ph.D. Thesis)

August 1994

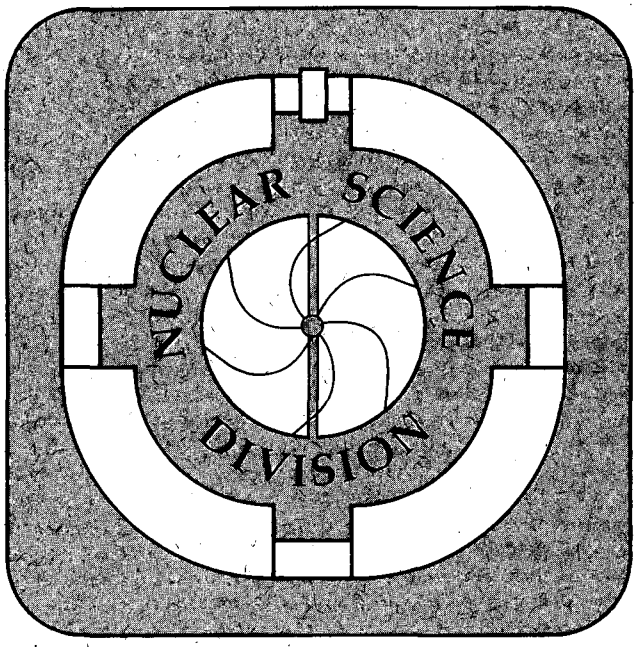

REFERENCE COPY
Does Not
Circulate
LBL-36087
Copy 1
Bldg. 50 Library.

Prepared for the U.S. Department of Energy under Contract Number DE-AC03-76SF00098

DISCLAIMER

This document was prepared as an account of work sponsored by the United States Government. While this document is believed to contain correct information, neither the United States Government nor any agency thereof, nor the Regents of the University of California, nor any of their employees, makes any warranty, express or implied, or assumes any legal responsibility for the accuracy, completeness, or usefulness of any information, apparatus, product, or process disclosed, or represents that its use would not infringe privately owned rights. Reference herein to any specific commercial product, process, or service by its trade name, trademark, manufacturer, or otherwise, does not necessarily constitute or imply its endorsement, recommendation, or favoring by the United States Government or any agency thereof, or the Regents of the University of California. The views and opinions of authors expressed herein do not necessarily state or reflect those of the United States Government or any agency thereof or the Regents of the University of California.

LBL-36087
UC-413

Heavy Residues from Very Mass Asymmetric Heavy Ion Reactions

Karl Alan Hanold
Ph.D. Thesis

Department of Chemistry
University of California

and

Nuclear Science Division
Lawrence Berkeley Laboratory
University of California
Berkeley, California 94720

August 1994

This work was supported in part by the Director, Office of Energy Research, Office of High Energy and Nuclear Physics, Division of High Energy Physics, of the U.S. Department of Energy under Contract No. DE-AC03-76SF00098 and by a National Aeronautics and Space Administration Research Training Grant (NGT-50783) and the University of California.

HEAVY RESIDUES FROM VERY MASS ASYMMETRIC HEAVY ION REACTIONS

By

KARL ALAN HANOLD

B.S. (Michigan State University) 1988

A dissertation submitted in partial satisfaction of the requirements for the degree of

DOCTOR OF PHILOSOPHY

in

CHEMISTRY

in the

GRADUATE DIVISION

of the

University of California at Berkeley

Committee in charge:
Professor Luciano G. Moretto
Professor Stanley G. Prussin
Professor John O. Rasmussen

1994

ABSTRACT

Heavy Residues from Very Mass Asymmetric Heavy Ion Reactions

by

Karl Alan Hanold

Doctor of Philosophy in Chemistry

University of California at Berkeley

Professor Luciano G. Moretto, Chair

The isotopic production cross sections and momenta of all residues with nuclear charge (Z) greater than 39 from the reaction of 26, 40, and 50 MeV/nucleon ^{129}Xe + Be, C, and Al were measured. The isotopic cross sections, the momentum distribution for each isotope, and the cross section as a function of nuclear charge and momentum are presented here. The new cross sections are consistent with previous measurements of the cross sections from similar reaction systems.

The shape of the cross section distribution, when considered as a function of Z and velocity, was found to be qualitatively consistent with that expected from an incomplete fusion reaction mechanism. An incomplete fusion model coupled to a statistical decay model is able to reproduce many features of these reactions: the shapes of the elemental cross section distributions, the emission velocity distributions for the intermediate mass fragments, and the Z versus velocity distributions. This model gives a less satisfactory prediction of the momentum distribution for each isotope. A very different model based on the Boltzman–Nordheim–Vlasov equation and

which was also coupled to a statistical decay model reproduces many features of these reactions: the shapes of the elemental cross section distributions, the intermediate mass fragment emission velocity distributions, and the Z versus momentum distributions. Both model calculations over–estimate the average mass for each element by two mass units and underestimate the isotopic and isobaric widths of the experimental distributions. It is shown that the predicted average mass for each element can be brought into agreement with the data by small, but systematic, variation of the particle emission barriers used in the statistical model. The predicted isotopic and isobaric widths of the cross section distributions can not be brought into agreement with the experimental data using reasonable parameters for the statistical model.

The overall agreement of the data and the model predictions suggests that the heavy residues produced in these reactions arise from compound nuclei formed in incomplete fusion-like reactions. An exception to this conclusion may be the most proton-rich nuclei observed in this study. These proton-rich nuclei are predicted to have less than 50 nanobarn production cross sections by both of these model calculations.

Luciano G. Moretto 8/12/94

Professor Luciano G. Moretto, Chair Date

DEDICATION

I dedicate this work of art to all the sunny days and the waves that have washed ashore during my stay in California.

Contents

LIST OF FIGURES vi

LIST OF TABLES xi

1 Introduction 1

1.1 Nuclear Collisions 1

1.2 Nuclear De-excitation 2

1.3 Reaction Mechanism Studies 5

1.4 Scope of Project 7

1.4.1 γ-ray Spectroscopy Studies 8

1.4.2 Magnetic Spectrograph Studies 9

1.4.3 The Experiment 9

2 Experimental Method 12

2.1 Experimental Setup 12

2.2 Calibration and Isotope Identification 17

2.3 Momentum Distribution Calculation 28

3 Experimental results 36

3.1 Momentum Distributions 36

3.2 Isotopic Distributions 37

3.3 Elemental and Isobaric Yields 52

3.4 Z versus Velocity Distributions 59

3.5 Summary of the Data 59

4 Discussion of data and models 62

4.1 The Velocity as a Function of Z 64

4.2 Model Calculations 70

4.2.1 Incomplete Fusion Calculation 70

4.2.2 Boltzman–Nordheim–Vlasov Calculation 89

4.3 Conclusion 100

5 Conclusions 102

5.1 Reaction Mechanism 103

5.2 Speculation on Future Work 105

A Momentum distributions 107

LIST OF REFERENCES 117

List of Figures

1.1 Figure illustrating the approximate domains of nuclear reaction mechanisms and decay processes. 3

2.1 Schematic layout of the A1200 mass separator. 14

2.2 Schematic electronics diagram for this experiment. 16

2.3 Bend radius calibration for Image #1 of the A1200. 19

2.4 Measured Z versus time of flight for the 50 MeV/nucleon ^{129}Xe + Al reaction. 21

2.5 Calibration spectra for ^{110}In^{46+} at 50 MeV/nucleon. 23

2.6 Typical silicon detector energy calibrations. 25

2.7 Typical Z resolution. 27

2.8 Typical q resolution. 29

2.9 Typical A resolution. 30

2.10 Momentum distribution for ^{104}Sn from the 40 MeV/nucleon ^{129}Xe + Al reaction shown as a solid line. Also shown are the distributions for each charge state. The ion momentum distributions are shown in various textures. 33

2.11 The angular acceptance of the A1200 and calculated angular distributions from the incomplete fusion model. 35

3.1 Momentum distributions for representative light, medium, and heavy isotopes of selected elements for the 50 MeV/nucleon ^{129}Xe+Al reaction. 38

3.2 Same as figure 3.1 but for 50 MeV/nucleon ^{129}Xe+C reaction. 39

3.3 Same as figure 3.1 but for 50 MeV/nucleon ^{129}Xe+Be reaction. 40

3.4 Isotopic cross sections for the 50 MeV/nucleon reactions. 42

3.5 Isotopic cross sections for the 40 MeV/nucleon reactions. 43

3.6 Isotopic cross sections for the 26 MeV/nucleon reactions. 44

3.7 Plots of the three-dimensional surface of the isotopic cross sections. . 45

3.8 Contour plots of the isotopic cross sections in the A versus Z plane for the ^{129}Xe + Be reactions. 46

3.9 Contour plots of the isotopic cross sections in the A versus Z plane for the ^{129}Xe + C reactions. 47

3.10 Contour plots of the isotopic cross sections in the A versus Z plane for the ^{129}Xe + Al reactions. 48

3.11 The average mass and the full width at half maximum (FWHM) of the mass distribution for each element from the 50 MeV/nucleon ^{129}Xe + Be, C, and Al reactions. 50

3.12 Contour plots of the isotopic cross sections in the A versus Z plane. The diamonds on the proton-rich side of the stable isotopes correspond to the data of Chung, Chu, and Porile for the 25, 35, and 45 MeV/nucleon ^{12}C + Ag reactions. 51

3.13 The mass yields from the 50 MeV/nucleon Xe+Al reaction are shown as curves. The mass yields from the 70 MeV/nucleon ^{92}Mo+^{58}Ni reaction are shown as histograms. 53

3.14 The elemental cross sections for each of the ^{129}Xe + Be reactions. . . 55

3.15 The elemental cross sections for each of the ^{129}Xe + C reactions. . . . 56

3.16 The elemental cross sections for each of the ^{129}Xe + Al reactions. . . 57

3.17 The isobaric cross sections for each of the target-beam energy combinations studied in this work. 58

3.18 Contour plots of Z versus velocity for all systems measured in this work. Also shown are results from similar systems. 60

4.1 Schematic representation of the effect of light charged-particle evaporation on the correlation between the velocity and the Z of the incomplete fusion product. 68

4.2 The cross section distributions as a function of Z and momentum for both the present data and the incomplete fusion model. 81

4.3 Experimental and predicted isotopic cross sections for the ^{129}Xe + Al reaction at 50 MeV/nucleon are shown. 83

4.4 The average mass of each element predicted by GEMINI for two different initial nuclei are shown. One system is very proton-rich, Z=67 and A=149, while the other system is very neutron-rich, Z=67 and A=166. 86

4.5 Calculated mean energy of the emitted nucleons as a function of time with the BNV model. 92

4.6 The mass, excitation energy, and velocity of the primary projectile-like fragment as a function of impact parameter from both the BNV (dotted) and ICF (solid curve) models for the reaction of 50 MeV/nucleon ^{129}Xe + Al. 96

4.7 Density distributions from the BNV calculations for the system of 26 MeV/nucleon ^{129}Xe+Al at an impact parameter of b = 5 fm. 98

4.8 Comparison of the BNV and ICF predictions for the 50 MeV/nucleon ^{129}Xe + Al reaction. 99

A.1 Momentum distributions for representative light, medium, and heavy isotopes of all elements from the 50 MeV/nucleon ^{129}Xe+Be reaction. 108

A.2 Same as figure A.1 but for the 50 MeV/nucleon ^{129}Xe+C reaction. . . 109

A.3 Same as figure A.1 but for the 50 MeV/nucleon ^{129}Xe+Al reaction. . 110

A.4 Same as figure A.1 but for the 40 MeV/nucleon ^{129}Xe+Be reaction. . 111

A.5 Same as figure A.1 but for the 40 MeV/nucleon ^{129}Xe+C reaction. . . 112

A.6 Same as figure A.1 but for the 40 MeV/nucleon ^{129}Xe+Al reaction. . 113

A.7 Same as figure A.1 but for the 26 MeV/nucleon ^{129}Xe+Be reaction. . 114

A.8 Same as figure A.1 but for the 26 MeV/nucleon ^{129}Xe+C reaction. . . 115

A.9 Same as figure A.1 but for the 26 MeV/nucleon ^{129}Xe+Al reaction. . 116

List of Tables

2.1 Data and calculated values of energy losses in ΔE1, ΔE2, and ΔE3 for each of the 18 calibration isotopes selected. The errors are shown in parentheses. 26

3.1 Maximum excitation energy possible for each beam energy and target combination (in MeV). 41

4.1 Excitation energy and average residue Z value for the transfer of a ^{6}Li to form ^{135}La in ^{129}Xe + Al reactions. 66

4.2 Excitation energy and average residue Z value for the transfer of a ^{12}C to form ^{141}Nd in ^{129}Xe + Al reactions. 66

ACKNOWLEDGEMENTS

I would like to thank the National Science Foundation for support under a Graduate Fellowship. The support this provided allowed me undertake a number of enjoyable activities that would have been otherwise unavailable.

Many of my friends supported and influenced my efforts during my graduate career. Brett Bush was always there to listen to my incessant, bitter wailing as my work did not go smoothly. Without his encouragement, I would have become skilled in the use of a hammer and been left to make cabinets for public consumption. Martin Umeh and the bite of the vinegar and spices in his famous three-bean salad provided proof that life was still good even at the most bleak of moments. Of great help were all my friends and parents who knew that my work was, at best, an intellectual exercise with absolutely no redeeming value, but supported my efforts toward my degree anyway. I also should thank my friends with whom I played volleyball, softball and ultimate, and went skiing, blading, backpacking, surfing and SCUBA diving as they all helped me keep track of the BIG picture.

I would like to thank all those who have helped me complete my thesis research: Daniel Bazin, Dave Bowman, Nicola Colonna, Nigel Orr, Brad Sherrill, and Kin Tso. Deserving special mention are my silent partners who helped smooth the english in my thesis; David Morrissey, who took a naive, college freshman under his wing and whose influence helped make me what I am today; Gordon Wozniak, for his invaluable help with running experiments and producing this work of art, and finally Luciano Moretto, my thesis advisor, who allowed me to pursue my own research interests.

Chapter 1

Introduction

Heavy ion collisions can be used to study the behavior of nuclei under a wide variety of conditions beyond those commonly found in nature. Nuclei found on Earth are stable or have very long half-lives and exist in their ground states. In contrast, a wide range of unstable and/or excited nuclei can be produced in heavy ion collisions. Studies of these reaction products give information on their nuclear properties and on the collision mechanism that created them.

1.1 Nuclear Collisions

A wide variety of heavy ion reaction mechanisms has been observed. A simplified picture of nuclear reaction mechanisms as a function of bombarding energy and impact parameter is shown in Figure 1.1. At low energies ($E/A < 10$ MeV) and small impact parameters, the two colliding nuclei come together and fuse, provided that the bombarding energy of the projectile is sufficient to overcome the repulsion of the nuclei. The fused product contains all of the protons and neutrons from both reaction partners. This process is called "complete fusion" [bir83]. At large impact parameters and low bombarding energy, the nuclei may just barely touch, form a neck joining

the two nuclei, and then separate. This type of collision is called "deep-inelastic" [hui77,mor81].

At higher beam energies (20 MeV $< E/A <$ 100 MeV) and at impact parameters for which the colliding nuclei do not completely overlap, the collision occurs with such speed that only a piece of the smaller nucleus is absorbed by the larger nucleus [bir83]. Geometrically, only the piece of the broken nucleus that overlaps the unbroken nucleus fuses with the unbroken nucleus. This reaction mechanism, called "incomplete fusion", gives a large range of nuclei with different numbers of protons and neutrons by fusing different fractions of the broken nucleus. There is a strong correlation of excitation energy with absorbed mass with the limit of total absorption (i.e. complete fusion) having the maximum excitation energy.

At high energies ($E/A >$ 30 MeV), nuclear collisions may be so violent that the nuclei break up into many smaller fragments. This process is called "multifragmentation". Ongoing research is attempting to determine if these fragments are emitted simultaneously or sequentially [mor93]. At even higher energies ($E/A >$ 100 MeV) and large impact parameters, the overlapping matter is sheared off both nuclei, forming a third piece of nuclear matter. This third piece has been called the "fireball", since it contains a large amount of excitation energy [wes76,gos77].

1.2 Nuclear De-excitation

Each of these collision processes leaves the resulting product(s) excited. The reaction products are detected several hundred nanoseconds after the reaction and this is enough time for the reaction products to de-excite. It is, therefore, important to account for the effect of the de-excitation process on the products of the reaction.

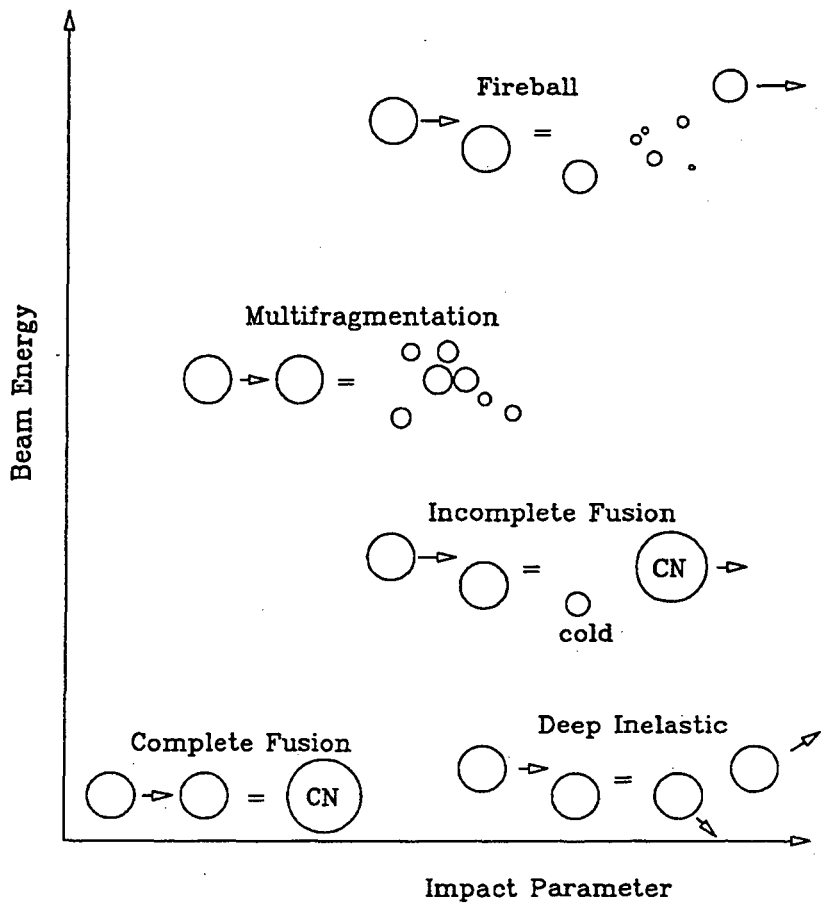

Figure 1.1: Schematic diagram illustrating the approximate energy and impact parameter domains of nuclear reaction mechanisms.

An excited nucleus may distribute its excitation energy among all of its accessible degrees of freedom. If the nucleus achieves this "relaxed" state, it is called a "compound nucleus". The formation of a compound nucleus takes place after the collision phase is over and represents a definite intermediate state between the entrance and exit channels. The relative probability for decay into any specific set of final products is independent of the means of formation of the compound nucleus. This independence was first demonstrated by studies of the p + ^{63}Cu $\rightarrow$ ^{64}Zn and ^{4}He + ^{60}Ni $\rightarrow$ ^{64}Zn reactions [gos50].

Historically, the products from compound nucleus decay have been divided into two distinct classes: light particles (such as neutrons, protons, and alpha particles) and, for heavier systems, fission fragments with masses approximately half that of the fissioning nucleus. Although both classes of products are emitted by compound nuclei, their large difference in mass gave rise to two different statistical theories describing their emission [boh39,wei37].

In the 1950s, fragments with masses between those of the light particles and those of fission fragments were first observed [mil53,sug54,wol56]. These fragments are labeled "complex fragments". Since then, many experiments have studied complex fragment emission over a wide range of bombarding energies and combinations of projectile and target [pos71,hyd71,kor73,zeb75,gos77,mey80,sob83,sob84,mcm85,cha88a,han89,cha90,del91,col89,wil92,wil91] [aug87,cha88b,bou88,chi83,jac83,fie84,fie89,fat87,bor88,bow91a,rou93,riv88,chu91,eth91,pla91,blu91,kin91,bow91b] [des91,mor88]. Initially, the observation of complex fragments was so surprising that many people associated their presence with the onset of a new reaction mechanism. It is possible, however, for compound nuclei to emit complex fragments. In the 1970s, Moretto showed this theoretically by generalizing the model for fission of the com-

pound nucleus to all mass asymmetries [mor72,mor75], thus eliminating the artificial distinction between light particles and fission fragments, and naturally accounting for complex fragment emission. In the 1980s, complex fragment emission was first experimentally observed from compound nuclei formed in low-energy reactions [sob83,mor88].

1.3 Reaction Mechanism Studies

Fission fragments are likely products of compound nuclei formed in nuclear reactions of highly fissile nuclei. Nuclear fission has been exploited to study the dynamics of incomplete fusion [vio89]. In the center of mass of the fissioning system, fission fragments are emitted with a relative angle of π radians. In the laboratory frame, the angle between the two fission fragments depends on the laboratory velocity of the fissioning system and is called the fission fragment folding angle. Thus, the linear momentum and energy transfer of the reaction can be inferred from this folding angle. Studies of the linear momentum transfer as a function of bombarding energy show a systematic evolution of the reaction mechanism from complete fusion to incomplete fusion.

A heavy residue is a more likely product than fission fragments for a low-fissility system. Such a residue can result from the complete or incomplete fusion of the target and projectile followed by light particle emission from the resulting compound nucleus. The velocity distributions of the heavy residue products have been used to determine the degree of fusion (see [bir83] and more recently [gil92,vin90,bec89,hag88,gon87].) The evolution of these distributions as a function of bombarding energy shows a transition from complete to incomplete fusion. This evolution is similar to that seen in the fission fragment studies of heavier systems.

Very asymmetric entrance channels favor complete or incomplete fusion reaction mechanisms. For reactions such as ^{139}La + C, studies have demonstrated the presence of a single source that emits complex fragments [cha88a,bow89]. Information about this source was extracted from coincidence measurements of the complex fragments. The source velocity, $\mathbf{v}_{source}$, is defined as

$$\mathbf{v}_{source} = \frac{\Sigma m_i \mathbf{v}_i}{\Sigma m_i} \tag{1.1}$$

where m_i and $\mathbf{v}_i$ are the mass and velocity, respectively, of the i-th detected complex fragment. Equation 1.1 has been used to identify and characterize sources in both complete and incomplete fusion reactions [bow89,han93,rou93]. The $\mathbf{v}_{source}$ is constructed from the fragments emitted from the compound nucleus. The fragment(s) from any target remnant(s) is(are) not included in this calculation. The observed $\mathbf{v}_{source}$ was shown to be consistent with complete fusion at low beam energies [cha88a] and with incomplete fusion at higher beam energies [bow91a]. The center-of-mass angular distributions ($d\sigma/d\theta$) of the complex fragments were isotropic for a range of fragments with masses between the mass of the projectile and that of the target. These isotropic distributions result from the statistical decay of the fused product. The angular distributions of fragments with Z values near those of the projectile and target have both isotropic and anisotropic components. The anisotropic component results from the deep-inelastic process.

In contrast, more symmetric heavy ion collisions show a more complicated picture. The reaction of ^{139}La + Ni at 18 MeV/nucleon, for example, produces complex fragment velocity distributions that show no well-defined source [col89]. The $\mathbf{v}_{source}$ from this reaction ranges from the velocity corresponding to complete fusion to near the velocity of the beam. The authors showed that it was possible to characterize the

mass and excitation energy of the compound nuclei formed in these incomplete fusion processes. This work was extended to higher bombarding energies for the ^{129}Xe + Ti and Cu reactions at 26 and 31 MeV/nucleon [han93]. An incomplete fusion model calculation reproduced all of the following experimental data: the elemental cross sections, the emission velocities of the decay products, the center-of-mass angular distributions, and the source velocity distributions.

Therefore, it can be said that complex fragment studies have facilitated the characterization of the nuclear reaction mechanisms. At low excitation energies, however, complex fragment emission is quite rare. This implies that studies using complex fragments to determine the reaction mechanism are ill suited to measure the yield of collisions that result in nuclei with low excitation energy. In the interpretation of ^{129}Xe+Ti and Cu and ^{139}La+Ti and Ni collisions, the authors claimed that the source velocity distribution was consistent with incomplete fusion processes; however, no events were observed with v_{source} above 90% of the velocity of the beam. The low-mass-transfer events populating this region were not observed because the product nuclei primarily de-excite via light particle evaporation and result in evaporation residues.

1.4 Scope of Project

Since heavy residues result from compound nuclei with low excitation energy, they should be a good tool to study the small mass transfer limit of the incomplete fusion process. Measurement of residue production resulting from incomplete fusion allows for the quantitative testing of the incomplete fusion model over the entire range of mass transfers. The studies mentioned above, which used a heavy projectile nucleus

and a light target nucleus, were unable to detect fragments with Z values near that of the projectile. The detectors used in these studies were placed at angles larger than 30 mrad to avoid elastically scattered beam particles. The residues with Z values near that of the beam are kinematically constrained to small angles. (Typical laboratory frame emission angles for these residues are less than 30 mrad.) Measurements of the production of heavy residues use two different techniques to avoid problems associated with the intense elastically scattered beam particles near 0 mrad: off-line γ-ray spectroscopy and the use of magnetic spectrometers.

1.4.1 γ-RAY SPECTROSCOPY STUDIES

With the γ-ray spectroscopy technique, the fragment production cross section as a function of nuclear charge, mass, kinetic energy (KE) and emission angles (θ, ϕ) is measured. These measurements are performed using a target surrounded by catcher foils which capture all fragments escaping from the target. The target is irradiated for a period of time and then the catcher foils are moved to a low-background environment. The yields of γ-ray emitting fragments are measured using high-resolution germanium detectors. By segmenting and stacking the catcher foils, angular and energy distributions of the reaction products have been extracted in addition to overall production cross sections.

This technique has many limitations. First, removing and transferring the catcher foils to the low-background counting area takes time (typically not less than ten minutes). This delay allows nuclei with short half-lives ($t_{1/2} < 5$ minutes) to decay. Since many nuclei far from stability have half-lives that are much shorter than 5 minutes, this is a serious limitation. Second, a characteristic γ-ray must be emitted

for nuclear identification. Nuclei not emitting a γ-ray or whose γ-ray lines are not unique can not be identified using this method. Third, very slowly moving fragments that do not escape the target are not detected. Fourth, the production cross section of undetected nuclei must be estimated from the measured cross sections. These estimations may contain large errors.

1.4.2 Magnetic Spectrograph Studies

A magnetic spectrometer can be used to separate the intense primary and elastically scattered beam from the reaction products. With this technique, the production cross section as a function of Z, A, KE, θ and ϕ is measured. In these experiments, high-resolution measurements of the time of flight, the bend radius in a known magnetic field, the rate of energy loss (ΔE), and the total energy of the fragments are made. This information yields unambiguous isotope identification. Since these experiments measure all parameters within 0.2 μs of the collision, all nuclei with a lifetime of 0.2 μs or more are detected. Since nuclear β-decay lifetimes are typically milliseconds, most isotopes meet this lifetime requirement and can be detected. If the reaction is performed using a heavy projectile nucleus on a light target nucleus, all of the heavy residues have sufficient kinetic energy to escape the target. This technique is better suited to measuring heavy residues than the γ-ray spectroscopy technique is, since all isotopes that meet the minimum lifetime requirement are measured.

1.4.3 The Experiment

For asymmetric heavy ion reactions at intermediate bombarding energies, the elemental cross sections for fragments with masses between those of the projectile and the

light particles have been accounted for by a complete or incomplete fusion process followed by statistical de-excitation [han93,bow91a]. Although a systematic study of the cross sections has been carried out for fragments with masses between those of the light particles and the projectile [cha88a,bow89,keh89,rou93,han93], fragments with Z values near or above that of the projectile have not been measured because they are kinematically constrained to very small angles when using a heavy projectile and a light target. Since these heavy residues contain the bulk of the yield for very asymmetric entrance channels, only a small portion of the total reaction cross section for these reactions has been measured. The model calculations that have been successful in predicting the complex fragment production have not been tested over the full range of Z values. In addition, since the isotopic distribution of the complex fragments has not been previously measured, the isotope production predictions of the models have not been tested.

In the present work, the production cross section for heavy residues from the reactions of 26, 40, and 50 MeV/nucleon ^{129}Xe + Be, C, and Al has been measured. To perform this measurement, a magnetic spectrometer was placed at 0 mrad in the laboratory frame and was used to measure the time of flight, the bend radius, the ΔE, and the total energy of each fragment produced in the reaction. The heavy residues were well identified in Z and A. For each isotope, the absolute cross section and momentum distribution were determined.

This study provides a determination of the relative amounts of incomplete and complete fusion that is complementary to that implied in the complex fragment studies. Events with very low excitation energy were easily measured since no fission-like decay was required. The isotopic yields were compared with the predicted yields from

two models. Combining the present data with previous data, experimental cross sections spanning almost the entire range of Z values produced in these reactions have now been measured.

The experimental details of the measurement are discussed in Chapter 2, and the results are presented in Chapter 3. In Chapter 4, model calculations of the measured nuclear reactions are presented and are compared to the experimental data. Chapter 5 contains the conclusions from this work and speculation on further work in this area.

Chapter 2

Experimental Method

2.1 Experimental Setup

In order to carry out the proposed study, an energetic beam of very heavy ions was necessary and a magnetic spectrometer was needed to analyze the products. The National Superconducting Cyclotron Laboratory (NSCL) at Michigan State University is the only facility in the western hemisphere with such beams; but it does not have, at present, a broad range, angle–adjustable spectrometer. The NSCL does have an achromatic fragment separator that can accept fragments near 0 mrad [she90]. Such a device should provide a good measurement of the bulk of the cross section, but not an angular distribution of the residues.

The K1200 cyclotron at Michigan State University accelerated beams of ^{129}Xe ions to 26, 40 and 50 MeV/nucleon. The beam was directed to the medium acceptance target position at the entrance of the A1200 mass separator. The reaction products were transported through the separator to the achromatic focal point. A schematic diagram of the A1200 spectrometer is shown in Figure 2.1. The A1200 spectrometer consists of 14 superconducting quadrupoles and four superconducting dipoles. Four sextupoles are used for higher-order optical corrections. The A1200 spectrometer has

an angular acceptance of 0.8 msr, 3% momentum acceptance, and a maximum rigidity of 5.4 T-m. The beam struck the target at 12 mrad with respect to the central axis of the spectrometer. The acceptance of the spectrometer, thus, ranged from 0 to 24 mrad in the laboratory frame and covered approximately 50% of the solid angle in this angular region.

In this study, the reaction products were identified with a technique similar to that used by Mohar et al. [moh91] and Bazin et al. [baz90]. This technique uses event-by-event measurements of the ΔE, the E_{total}, the time of flight, and the magnetic rigidity to give unambiguous isotope identification.

The ^{129}Xe beams bombarded targets of Be, C, and Al at the object point of the A1200. The reaction products were collected and transported through the mass separator. At the first dispersive focus, labeled Image #1 in Figure 2.1, a gas multistep detector measured the position of each fragment. This detector also provided the start time for the time-of-flight measurement. The multistep detector was similar in design to a detector previously described by D.J. Vieira *et al.* [vie84]. The wire spacing in the detector was 1 mm, and the summed transparency for all wire planes was better than 96%. The filling gas was iso-octane and was maintained at a pressure of 3 torr. This detector is capable of better than 0.4 ns timing resolution and 1.6 mm position resolution, corresponding to one part in 2000 momentum resolution.

In order to measure the Z, KE, θ, and ϕ (nuclear charge, kinetic energy, emission angles, respectively) of each ion, a set of detectors was placed at the focal point of the mass separator. Two parallel plate avalanche counters (PPACs) measured the position of each ion with 1 mm resolution and were separated by 420 mm. The measured positions were used to calculate θ and ϕ. A 0.0001 cm thick Bicron BC404

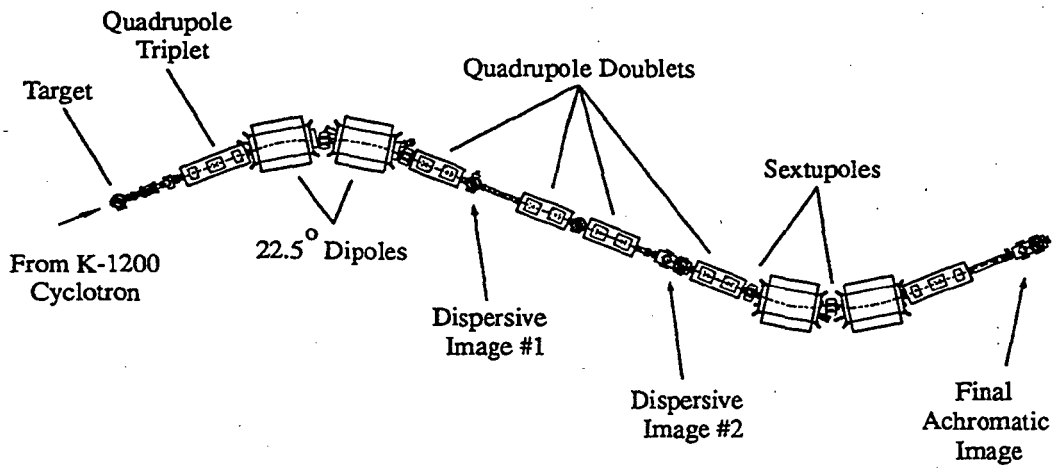

Figure 2.1: Schematic layout of the A1200 mass separator.[she90]

scintillating foil was mounted on a plastic light guide and optically coupled to an RCA RC232 photomultiplier tube (PMT). The PMT signal from this detector was combined with the time information from the multistep detector at Image #1 to measure the time of flight of the ions over the 13.811 m flight path. With this pair of detectors, a time-of-flight resolution of about 0.6 ns was obtained for the reaction products. A four-element silicon detector telescope provided ΔE and total energy measurements for each ion. The silicon detectors, labeled ΔE1, ΔE2, ΔE3, and ΔE4, were 51.4, 51.5, 319, and 540 μm thick, respectively. Detectors ΔE1 and ΔE2 were ORTEC totally depleted planar surface barrier silicon detectors with a thickness uniformity of better than $\pm$0.2 microns. Detectors ΔE3 and ΔE4 were totally depleted surface barrier silicon detectors. ΔE3 suffered radiation damage during the experiment and was replaced part way through the experiment with a 500 μm partially-depleted detector. Each of the silicon detectors had an active area of 300 mm^2. All the silicon detectors were cooled to -20^0 C in order to reduce the thermal noise and thereby improve the signal-to-noise ratios.

A schematic diagram of the electronics setup used for this experiment is shown in Figure 2.2. As many as 33 signals were read by the front-end computer for each event: analog-to-digital converter (ADC) and time-to-digital converter (TDC) signals for each of the four silicon detectors (8); ADC and TDC signals for the right, left, down, and up position signals for each of the four PPAC positions (16); charge-to-digital converter (QDC) and TDC signals for the stop scintillator (2); TDC signals from each of the down, up, right, left, and anode lines from the multistep gas start detector (5); and ADC signals from two time-to-amplitude converters (TACs) (2). The data was collected and written onto magnetic tape by the standard National Superconducting

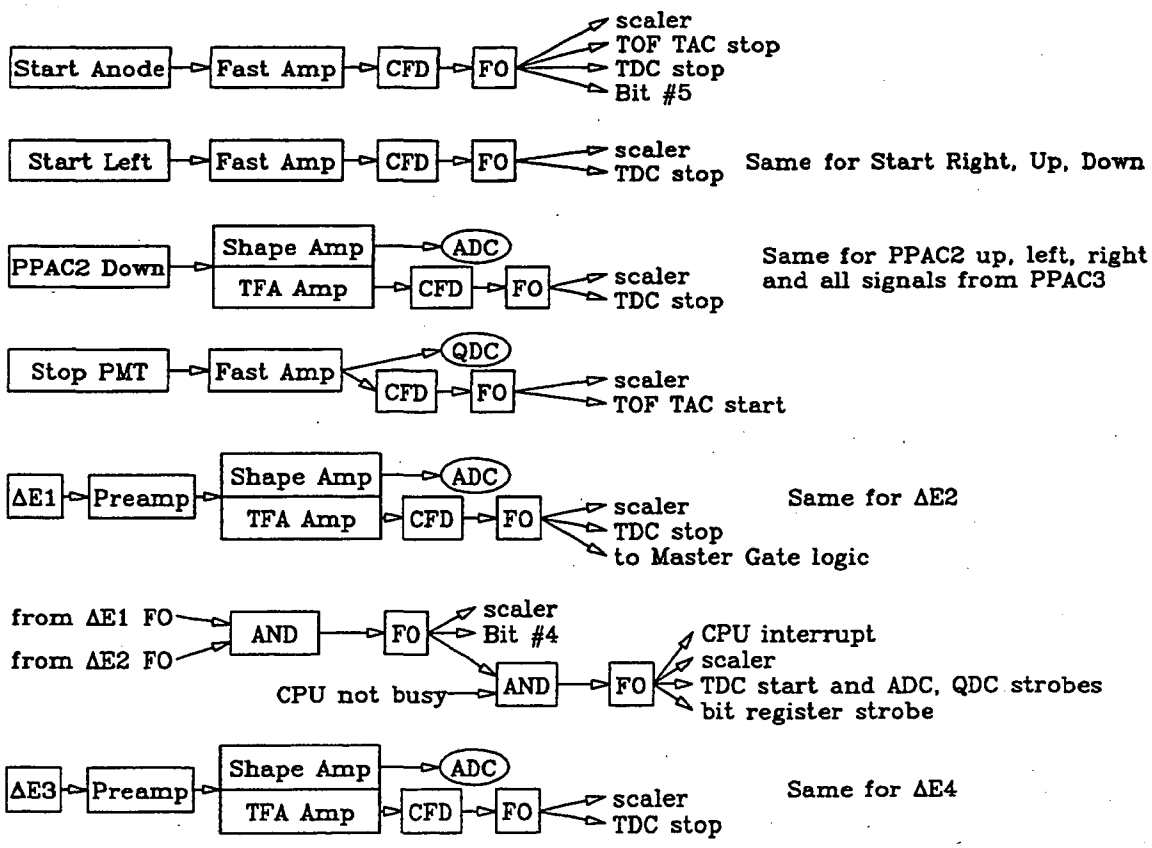

Figure 2.2: Schematic electronics diagram for this experiment.

Cyclotron Laboratory hardware and software systems[fox89]. The event trigger was produced by requiring a hardware coincidence within 30 ns between the constant fraction discriminator signals for ΔE1 and ΔE2. This coincidence was combined with the computer-not-busy signal to produce the master gate. The TDCs were operated in the common start mode. Some of the signals, e.g. the PPAC TDCs and the stop scintillator QDC, were used as diagnostic signals and were monitored only to make sure that the detectors were working properly. Nuclear magnetic resonance (NMR) probes in each of the dipole magnets were used to determine the magnetic fields.

Approximately 24 hours was required at each bombarding energy to collect the required data. Between 8 and 16 magnetic rigidity settings of the spectrometer were needed to cover the momentum range of the reaction products for each reaction.

2.2 Calibration and Isotope Identification

The detection system was calibrated by transporting various primary beam analogues directly through the A1200 spectrometer. These beams have very similar charge–to–mass ratios and are commonly used to calibrate detector systems [mcm86]. Since the reaction products were highly stripped when exiting the target, an Al target was used to strip the calibration beams. These ions with known energies and masses were used to calibrate the Image #1 (horizontal) position measurement (X) versus the rigidity and the detector telescope. From the mass (m), charge (q), dipole field (B), and incident energy, the bend radius (ρ) of each charge state was calculated from the relativistic form of the rigidity:

$$B\rho = \frac{m\beta\gamma}{q} \tag{2.1}$$

where the usual relativistic parameters are

$$\beta = \frac{v}{c} \tag{2.2}$$

$$\gamma = \frac{1}{\sqrt{1-\beta^2}} \tag{2.3}$$

where v is the ion velocity, and c is the speed of light. The bend radius was expanded in terms of the Image #1 X or horizontal position. The linear form was used to obtain the fit shown in Figure 2.3.

The flight time was calibrated by setting all the magnets so that the beam traveled along the central trajectory of the A1200 magnetic spectrometer, where the path length could be determined most accurately. Since the beam energy is known and the path length is fixed, the flight time can be calculated, and thus the time offset from the cable delays. The slope of the time calibration was determined by using a precision time calibrator. The common technique to prevent unnecessary starts of the TAC was used in which the "start" signal for the TAC came from the focal plane detector. In such a setup, time effectively runs backwards in the TAC, since one starts the clock with the focal plane signal and stops the clock with the delayed Image # 1 signal.

The calibration of the silicon detectors was performed in two stages. The initial energy loss calibration relied on ionizing trace impurities in the ECR source that were extracted and accelerated in the K1200 cyclotron. Low beam intensities (100-1000 particles/s) were required since these calibration beams impinged directly on the detector telescope. Beams used were $^{65}Cu^{14+}$, $^{83}Kr^{18+}$, $^{97}Mo^{21+}$, $^{130}Xe^{29+}$, and $^{134}Xe^{29+}$ at 50 MeV/nucleon; $^{84}Kr^{17+}$ and $^{94}Mo^{19+}$ at 40 MeV/nucleon; and $^{86}Kr^{14+}$ and $^{92}Mo^{15+}$ at 26 MeV/nucleon. The energy lost in each detector by each calibration

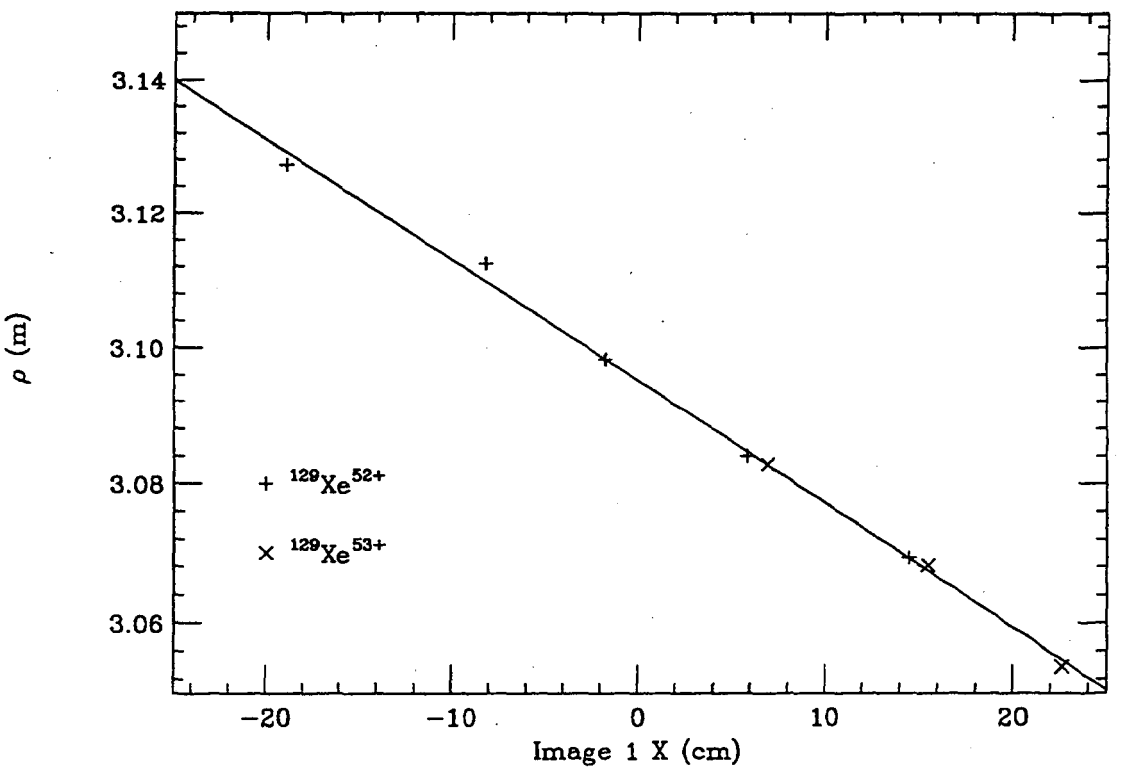

Figure 2.3: Bend radius calibration for Image #1 of the A1200. $\rho = -0.00178902X + 3.09516$ with ρ in m and X in cm.

beam was calculated using standard energy-loss tables [hub80]. These calculated energy losses in each detector were plotted versus the measured peak position. This first stage energy loss calibration proved adequate to provide an initial Z calculation using the equation

$$Z = a \cdot (\Delta E * E_{total})^{\frac{1}{3}} + b \cdot \Delta E \tag{2.4}$$

The Z of each ion was calculated using the ΔE values from both ΔE1 and ΔE2. This procedure provided a redundant Z determination for each ion, and the two calculations were averaged to improve the Z resolution.

The first stage isotope identification and an improved energy loss calibration were obtained by plotting the extracted Z value versus the measured time of flight (see Figure 2.4). This two-dimensional scatter plot shows the resolved elements as horizontal ridges. Since the A1200 accepts a small momentum range (only $\pm 1.5\%$ of the central momentum), the individual isotopes of a given element are separated in time and appear as bumps along each ridge. There is one complication in this simple picture. An ion with a given mass to charge ratio, A/q, is only slightly separated in time-of-flight from ions with the same Z but having $(A+2)/(q+1)$ or $(A-2)/(q-1)$. This separation is about 0.4 ns, which is less than the experimental timing resolution of 0.6 ns. Therefore, it was not possible separate isotopes with very similar A/q by gating on this spectrum only. Elastically scattered beam particles were also present in this spectrum, indicating the position of the ^{129}Xe ions. Furthermore, peaks in the time dimension for each Z were visible and well resolved. For the 40 and 50 MeV/nucleon runs at low rigidity, a vertical line of spots was produced at small time of flight due to a sequence of ions with (A/q)=2. With this characteristic reference line, the peaks for the lower Z values ($20 \leq Z \leq 30$) were easily assigned to a given

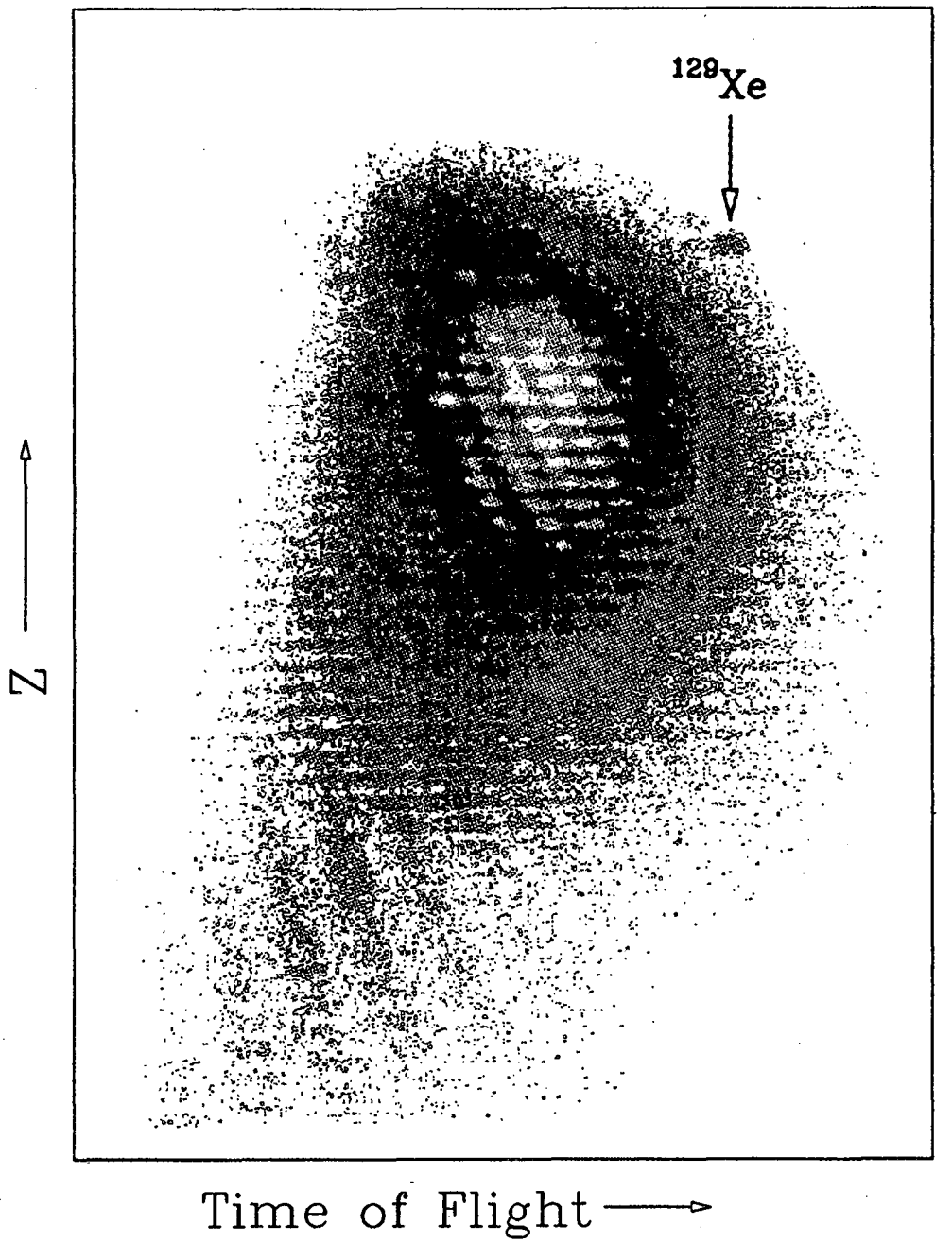

Figure 2.4: Measured Z versus time of flight for the 50 MeV/nucleon ^{129}Xe + Al reaction.

isotope, as these ions should be fully stripped at these high beam energies.

For the second stage of the calibration, eighteen isotopes from various regions of this two-dimensional spectrum were chosen as calibration isotopes. Each selected ion was also required to travel along the central ray of the spectrometer by a software gate on the image #1 position. By requiring this condition, the energy of each ion could be easily calculated and the selected ion separated from other ions with similar A/q values. This software condition restricted ions at the Image #1 X position to be within 3 mm of the central bend radius. Energy spectra from each silicon detector for each selected isotope were obtained and a set of energy spectra for $^{110}In^{46+}$ is shown in Figure 2.5. The small peak at the largest channel numbers in the ΔE3 and ΔE4 spectra arises from a contaminating isotope, $^{112}In^{47+}$. These spectra illustrate the clear separation of adjacent isotopes achieved by gating on Z, time of flight, position, and E_{total} in this experiment.

The times of flight of the selected calibration isotopes were calculated using the equation

$$t_{flight} = \frac{\ell}{c}\left[\left(\frac{3.10711 \cdot A}{qB\rho}\right)^2 + 1\right]^{\frac{1}{2}} \tag{2.5}$$

where ℓ is the path length. This expression can be derived from equation 2.1 using

$$v = \frac{\ell}{t_{flight}} \tag{2.6}$$

The times of flight calculated using this formula were plotted against the channel number from the time-of-flight TAC. The resulting calibration was compared to the time-of-flight calibration obtained from the beam and TAC calibrator. The two time-of-flight calibrations were found to be the same within experimental error.

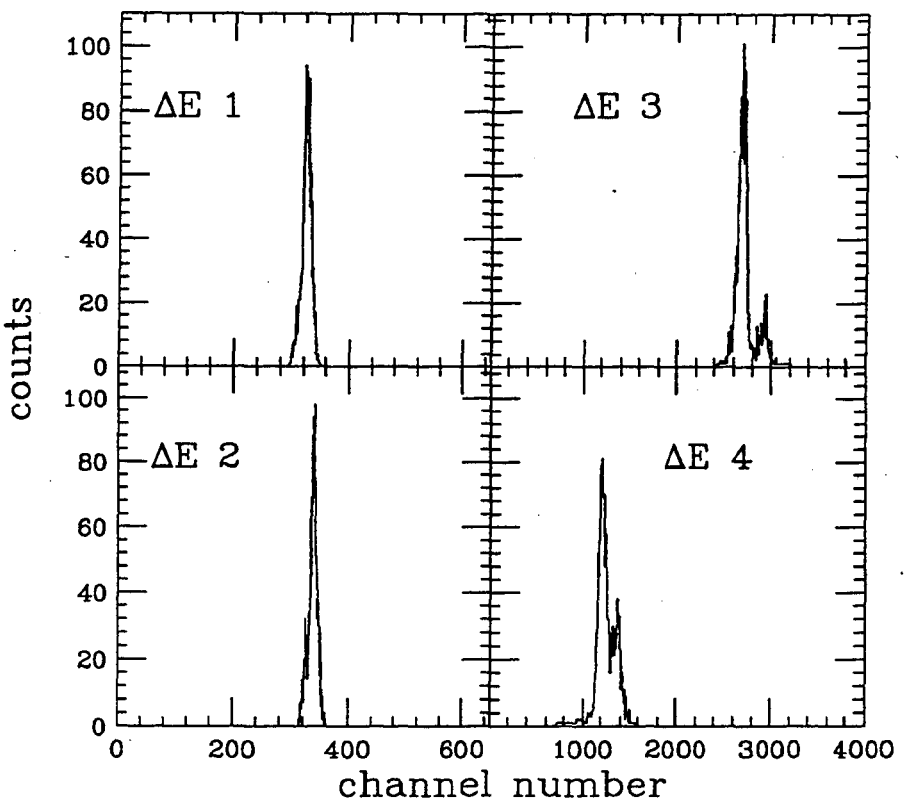

Figure 2.5: Calibration spectra for $^{110}In^{46+}$ at 50 MeV/nucleon. The small shoulder in the $\Delta E3$ and $\Delta E4$ spectra is created by contamination from $^{112}In^{47+}$ ions.

A computer program was created to calculate the energy loss of these selected isotopes as they passed through all the detectors in the device. The input parameters for the program were the magnetic fields for the run and the A, Z, and q of the ion. To calculate the energy of the ion, the computer code assumed that the ion had traveled along the spectrometer's central ray. The program then calculated the energy lost in going through the multistep start detector, the two PPACs, the stop detector's scintillating foil, and each of the silicon detectors until the full energy of the ion had been lost. The calculated value for the energy lost in each silicon detector was compared to the centroid value of the experimental energy loss distribution in each detector. This gave a second stage calibration of energy versus channel number for each silicon detector. These calibrations are shown in Figure 2.6 for the 40 MeV/nucleon data. A comparison of the calculated and experimental energy losses is shown in Table 2.1 for the 40 MeV/nucleon data.

The second stage Z calibration was obtained by using the improved energy loss calibrations. The final experimental Z resolution for the 40 MeV/nucleon data is shown in Figure 2.7 ($\sigma(Z) = .36$ esu). This calibration procedure was repeated for each beam energy and similar KE, Z, A, and Q resolutions were obtained in each case.

The mass of each ion was calculated from its measured total energy and time-of-flight data using the equation

$$A = \frac{E_{total}}{931.496(\gamma - 1)} \tag{2.7}$$

where A is in atomic mass units and E_{total} is in MeV. By substituting this equation

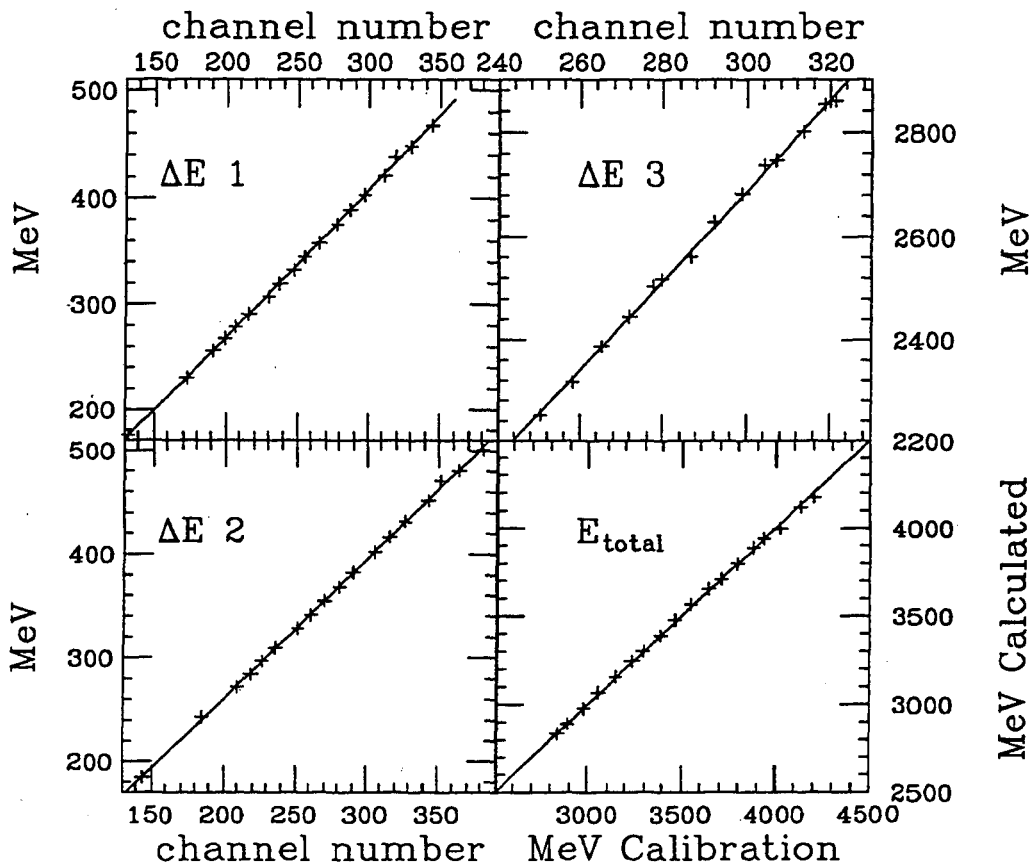

Figure 2.6: Typical silicon detector energy calibrations.

Table 2.1: Data and calculated second stage values of energy losses in ΔE1, ΔE2, and ΔE3 in units of MeV for each of the 18 calibration isotopes selected. The errors are shown in parentheses.

Nuclei	Number of ions	ΔE1 Data	ΔE1 Calc	ΔE2 Data	ΔE2 Calc	ΔE3 Data	ΔE3 Calc	% error Total E
^{78}Sr	65.	230.3	229.8	240.0	243.5	2256	2251	+0.1
^{81}Y	51.	245.7(6.1)	244.7	259.8(4.5)	260.2	2272	2257	0.0
^{83}Zr	124.	256.7(5.8)	255.9	273.4(5.0)	272.1	2331	2317	+0.1
^{85}Nb	120.	267.6	267.4	285.8(4.9)	284.4	2384	2387	−0.4
^{87}Mo	74.	278.4	279.0	295.9(5.0)	297.0	2443	2445	−0.3
^{89}Tc	118.	291.1(6.6)	290.0	309.7(4.7)	309.6	2489	2503	−0.2
^{92}Ru	197.	310.4(4.9)	307.2	329.1(4.9)	328.1	2507	2517	−0.2
^{94}Rh	158.	321.1(5.0)	319.6	342.4(4.6)	341.2	2566	2562	−0.3
^{96}Pd	136.	333.7(5.8)	332.3	354.7(4.5)	354.8	2615	2628	−0.4
^{98}Ag	179.	345.2(5.5)	345.1	369.3	368.6	2673	2683	−0.5
^{100}Cd	119.	359.1(6.9)	358.1	382.2(4.4)	382.6	2726	2738	−0.4
^{103}In	285.	376.8(5.5)	375.8	403.0(5.0)	402.3	2749	2747	0.0
^{105}Sn	302.	389.7(6.8)	389.3	416.2(5.9)	416.9	2801	2801	−0.1
^{107}Sb	227.	403.5(6.1)	403.0	431.3(5.6)	431.7	2849	2853	−0.6
^{110}Te	175.	423.7(5.5)	421.3	454.0(5.3)	452.0	2865	2860	−0.1
^{113}I	302.		440.1		472.8	2892	2867	+0.6
^{116}Xe	224.	449.4(6.3)	448.4	481.3(6.7)	480.2	2983	3053	+0.4
^{119}Cs	419.	469.4(5.9)	467.4	504.2(5.7)	501.6	2988	3059	+0.6

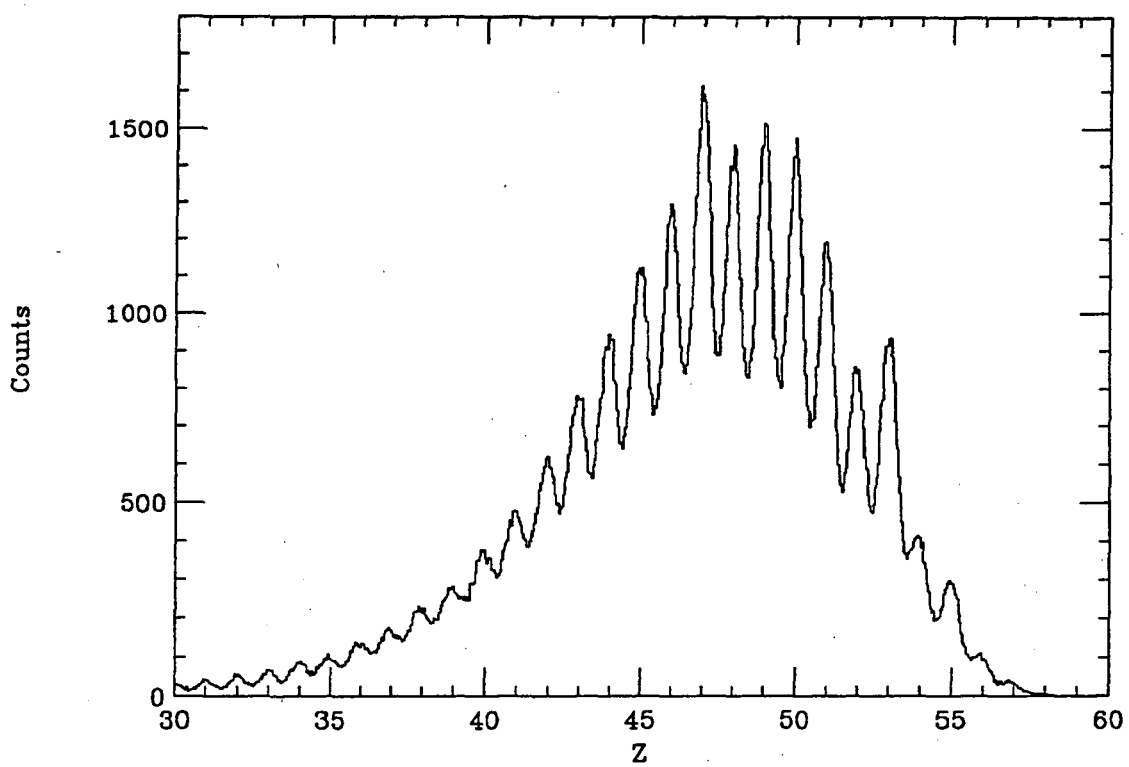

Figure 2.7: Typical Z resolution obtained in the 40 MeV/nucleon ^{129}Xe + Al reaction.

into equation 2.1 and solving for q, one obtains

$$B\rho = 3.10711\beta\gamma\frac{A}{q} \tag{2.8}$$

$$q = \frac{3.10711}{931.496}\frac{E_{total}}{B\rho(\gamma-1)}\beta\gamma \tag{2.9}$$

where q is in units of electronic charge and $B\rho$ is in Tesla-meters. A histogram of the calculated q is shown in Figure 2.8 and indicates the good resolution achieved ($\sigma(q)$=0.28 esu). Since q must be an integer and the mass resolution was limited by the error in the total kinetic energy measurement, the calculated q was rounded to the nearest integer and the mass was recalculated using an integer q in the equation

$$A = \frac{B\rho q}{3.10711\beta\gamma} \tag{2.10}$$

giving A in atomic mass units again. A typical mass spectrum is shown in Figure 2.9 and indicates the good mass resolution achieved ($\sigma(A) = 0.35$ amu).

2.3 Momentum Distribution Calculation

The momentum, p, of each particle was calculated using the equation:

$$p = 931.496\frac{B\rho q}{3.10711 \cdot A} \tag{2.11}$$

where the calculated A and q values are used. The A1200 has a 3% momentum acceptance, and the momentum distributions of the products from these reactions are much wider than the acceptance. To cover the entire momentum range, a number of runs were made using different magnetic field settings. Each run had central momenta differing by 2% from the neighboring runs. The momentum acceptance was not uniform at 100% across the full momentum range. It has been shown [orr92] that the momentum acceptance of the A1200 drops by 10% at 1% from the central ray

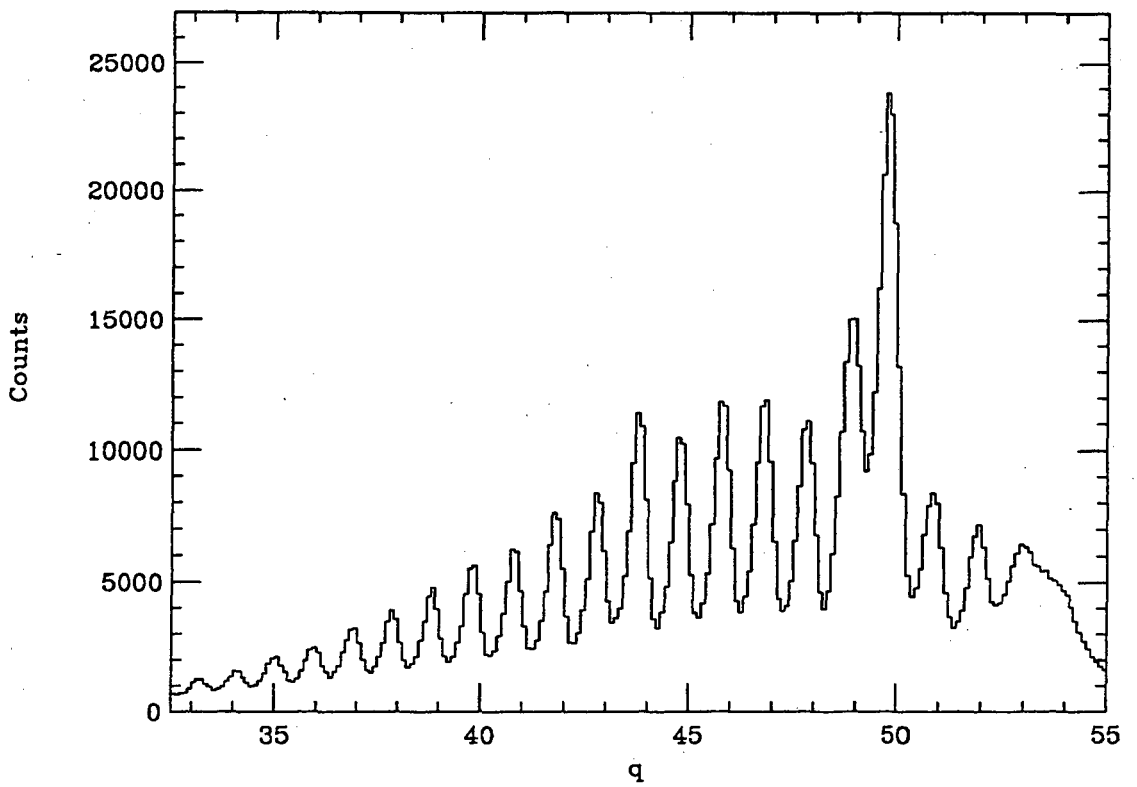

Figure 2.8: Typical q resolution obtained in the 40 MeV/nucleon ^{129}Xe + Al reaction.

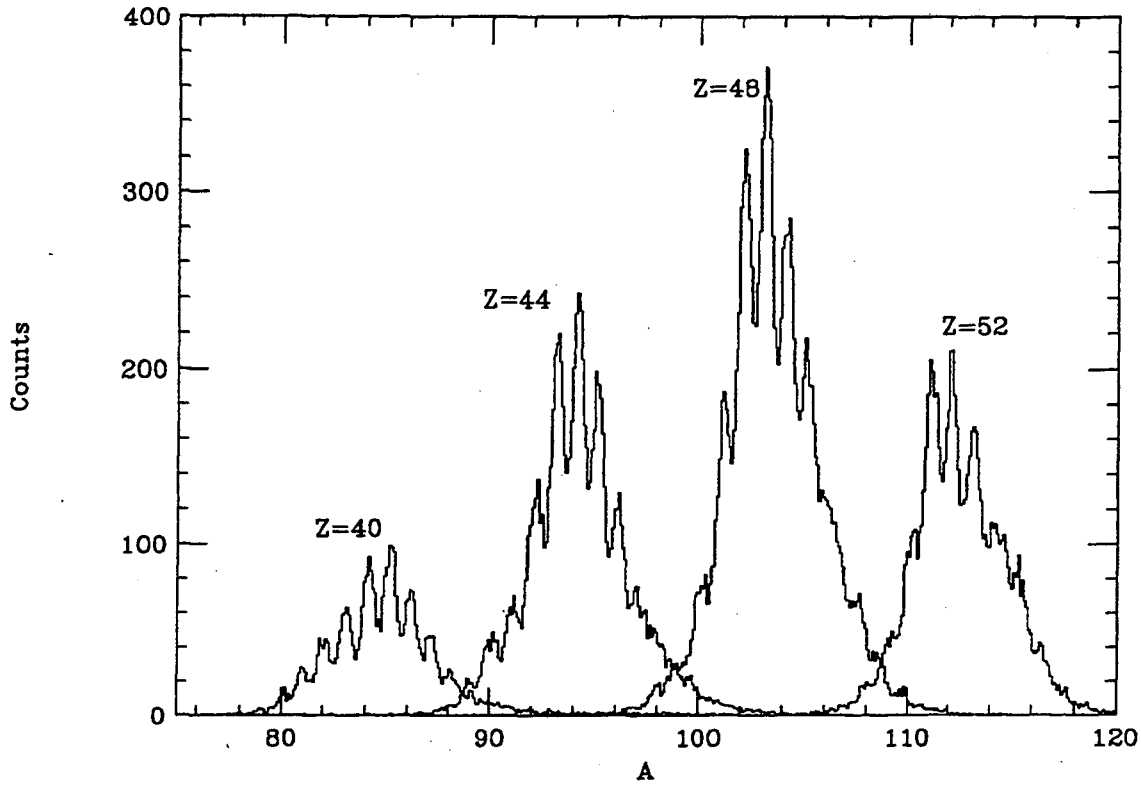

Figure 2.9: Typical A resolution obtained in the 40 MeV/nucleon ^{129}Xe + Al reaction.

and as much as 30% at 1.5% from the central ray. The momentum distribution for each run was multiplied by the reciprocal of the acceptance function to correct for this limited acceptance.

Four PIN diodes were placed symmetrically around the target and were used to measure the beam current. The count rate of the PIN diodes was related to the beam current so that the absolute beam flux for each run was known. The momentum distributions from each run were normalized using the beam flux and then added together. There were regions with no data in the distributions. These gaps arose from the tremendous amounts of scattered beam at a few particular momenta. The edges of the measured momenta were located and each gap was filled by interpolating between the edges. This final correction permitted the compilation of momentum distributions for all the ions with $Z > 39$.

The momentum distributions of interest are actually the distributions for each isotope as it exits the target rather than the distributions of each ion at the focal point. To produce this isotopic momentum distribution, all the momentum distributions for the charge states of each isotope must be summed. Since the ions have passed through the start detector, the charge state of the ion may have been changed at this point. Ion–optical calculations showed that, if the charge state of an ion changed in the start detector, the focus for that ion occurred at a different point at the final image of the spectrometer [she93]. The focus of charge-changed ions was displaced horizontally from the original focal point of the spectrometer by about 4 cm for the case of q=50 and had changed one charge state. The focus was even further away in space if the initial q was lower or the change had been greater than one charge state. Charge-changed ions missed the silicon detector stack and were not observed. To account for this

loss, it was assumed that the start detector recreated the equilibrium charge state distribution. Charge state equilibrium was attained for 50 MeV/nucleon ^{129}Xe in carbon for all thicknesses greater than 1 mg/cm^2. This assumption was checked by measuring the charge state distribution for 1.0, 1.3, and 2.0 mg/cm^2 thick carbon foils. The measured charge state distribution did not change as a function of carbon foil thickness. The lower beam energies attain equilibrium in thinner carbon foils. Since the start detector is made of plastic foils and filled with iso-octane, carbon is a good approximation to its material composition. The areal thickness of the start detector was 1 mg/cm^2, and thus the assumption of the start detector recreating charge state equilibrium is reasonable. To create the final isotopic momentum distribution, the momentum distributions for each charge state of an isotope were summed after the correction for charge change in the start detector had been applied. Figure 2.10 shows each of the momentum distributions for each ion of ^{104}Sn after corrections and the final summed momentum distribution.

This process yields the momentum distribution for the each isotope over the angular range of 0 to 24 mrad. The reaction products were distributed over a wider angular range. Thus in order to extract the absolute yield of an isotope the effects of the limited angular acceptance must be removed. The angular spread of the ions was calculated assuming an incomplete fusion reaction mechanism. (See Section 4.2.1 for a description of the incomplete fusion calculation.) The width of the angular distribution results primarily from evaporation from the fused product. This width was only slightly changed by using a Boltzman–Nordheim–Vlasov model of the reaction mechanism. (See Section 4.2.2 for a description of the Boltzman–Nordheim–Vlasov calculation.) Figure 2.11 shows the angular acceptance in the top frame. The calcu-

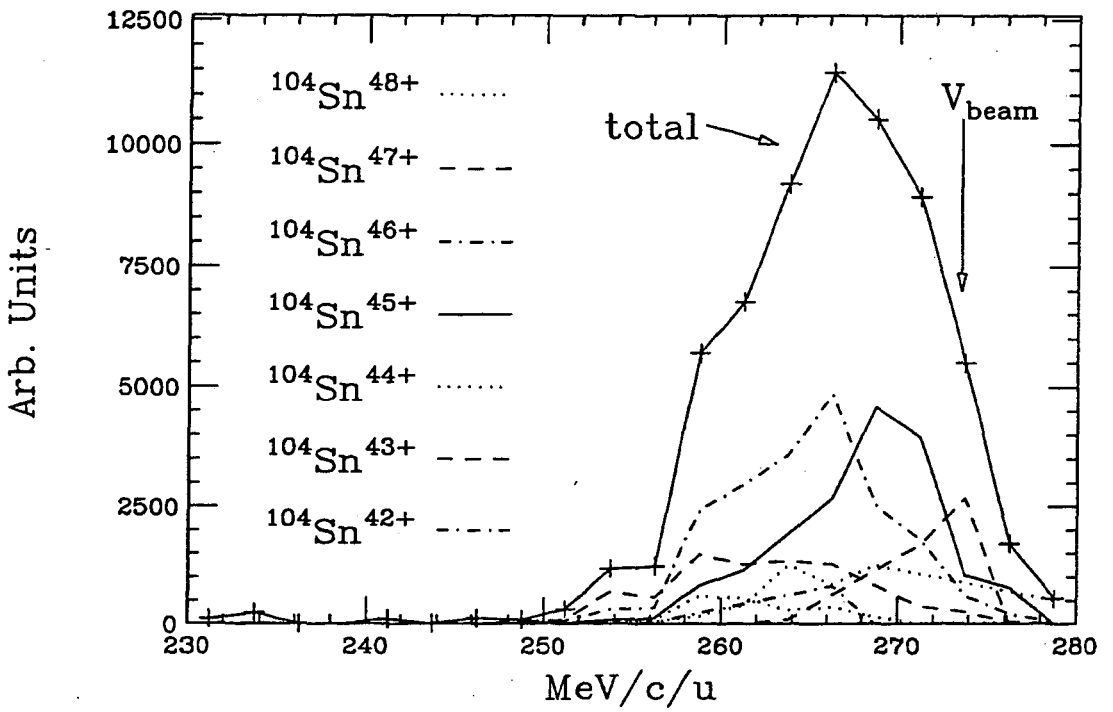

Figure 2.10: Momentum distribution for ^{104}Sn from the 40 MeV/nucleon ^{129}Xe + Al reaction shown as a solid line. Also shown are the distributions for each charge state. The ion momentum distributions are shown in various textures.

lated laboratory angular distributions for various isotopes are shown in the bottom frame. The fraction of the angular distribution that was contained within the angular acceptance of the A1200 was calculated. The yields for each isotope were then multiplied by the reciprocal of the acceptance fraction. This final correction allowed the compilation of the absolute production cross section for each isotope from each reaction. The statistical error in the absolute yield of each isotope from the counting statistics is typically less than 10%. The beam current measurement did not work very well. A factor of four systematic error in the absolute beam flux is possible. This results from a poor normalization of the PIN diode count rate to the beam current.

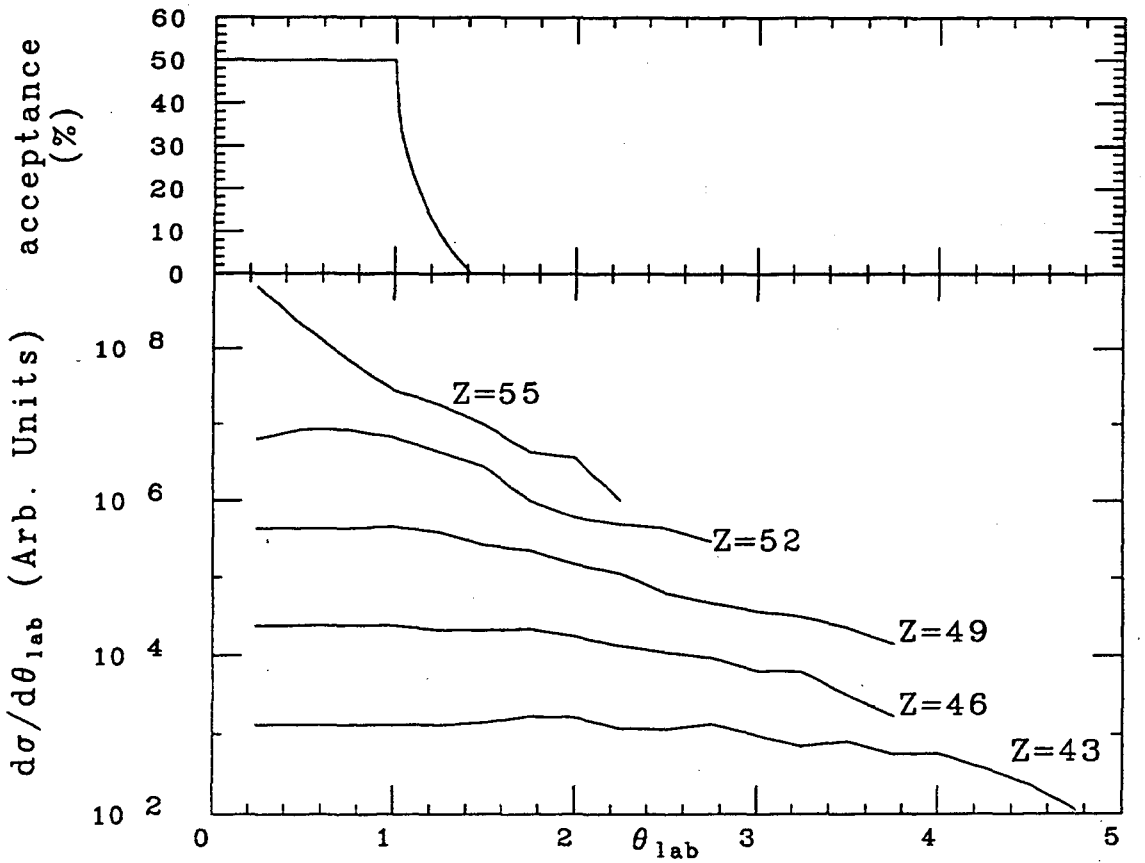

Figure 2.11: The angular acceptance of the A1200 is shown in the top frame. Calculated angular distributions from the incomplete fusion model for selected elements are shown in the bottom frame.

Chapter 3

Experimental results

This chapter presents the experimental results from the current measurement and the method of extracting each result. These results are compared with prior measurements of similar quantities and systems. Qualitative discussion of the data and quantitative comparison with theoretical models is reserved for Chapter 4.

3.1 Momentum Distributions

As indicated in the previous chapter, the momentum of each particle was calculated using the equation

$$p = 931.496 \frac{B\rho q}{3.10711 \cdot A} = 931.496 \beta\gamma c \tag{3.1}$$

where p is the momentum per nucleon in MeV/c/u and u is the atomic mass unit. The $\beta\gamma$ product was not calculated from the time-of-flight measurement but rather deduced from the Bρ calculated from the NMR reading and the bend radius measured at Image #1. This Bρ determination was used because it was more accurate than the time-of-flight measurement. Typical momentum distributions from the 50 MeV/nucleon ^{129}Xe + Be, C, and Al reactions are shown in Figures 3.1 to 3.3 for representative light, medium, and heavy isotopes of selected elements. The fluctu-

ations in the curves are due to low statistics. For a given element, the momentum distributions of the light mass isotopes peak near the momentum per nucleon of the beam, whereas the momentum distributions of the heavier isotopes peak at lower value. The momentum distribution of the heaviest isotope of the elements close to Z=40 extend almost down to the momentum per nucleon corresponding to complete fusion. These differences are most distinct in the data from the ^{129}Xe+Al reaction and are less apparent in the data from the Be and C targets due to the smaller range of momentum between the momentum per nucleon of the beam and that of the center of mass. The data from the two lower beam energies exhibit similar behavior. (Momentum distributions for all elements for the 50, 40, and 26 MeV/nucleon reactions are contained in Appendix A.)

3.2 Isotopic Distributions

The absolute cross section for the production of each isotope was calculated by integrating its momentum distribution. The measured isotopic cross sections for each of the nine target–beam energy combinations are shown in Figures 3.4, 3.5, 3.6, and 3.7 for isotopes with $Z > 39$. The overall dependence of the isotopic cross sections on bombarding energy and target mass is shown in Figure 3.7. The yield for the lighter elements produced in the reaction of the 26 MeV/nucleon ^{129}Xe with the light targets is quite low (as indicated in Figure 3.6), and the cross sections are more uncertain. The low counting statistics lead to the large fluctuations in the data between neighboring isotopes (e.g. a factor of 5 for Z=40 in the 26 MeV/nucleon ^{129}Xe + Be reaction).

A peak at A=129 is clearly visible in the Z=54 curve in Figures 3.4, 3.5, 3.6,

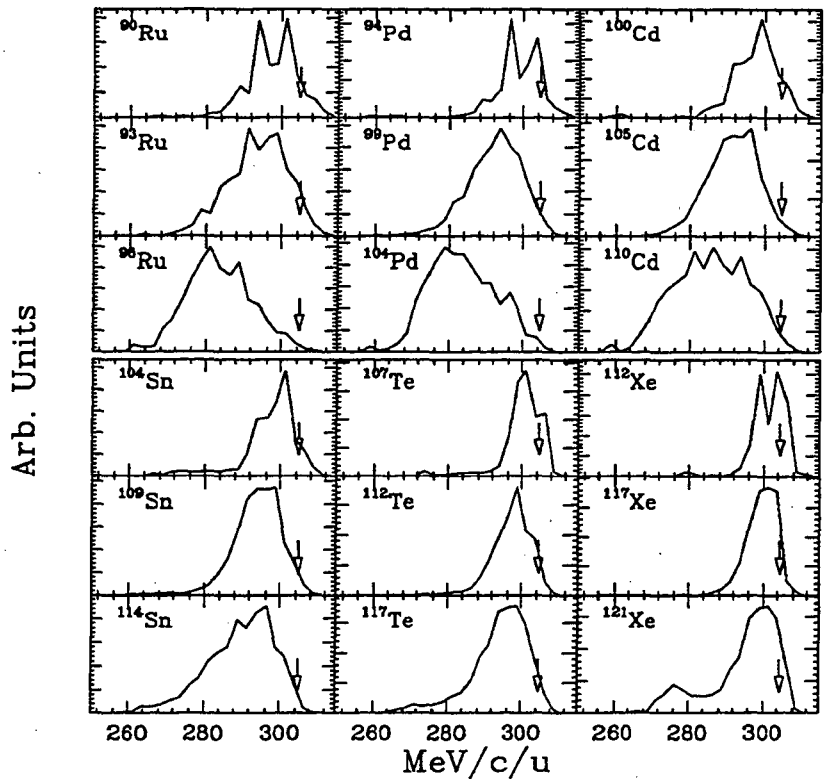

Figure 3.1: Momentum distributions for representative light, medium, and heavy isotopes of selected elements for the 50 MeV/nucleon ^{129}Xe+Al reaction. The arrow is at the momentum of the beam in each frame. The momentum of the center of mass for this system is 251.9 MeV/c/u.

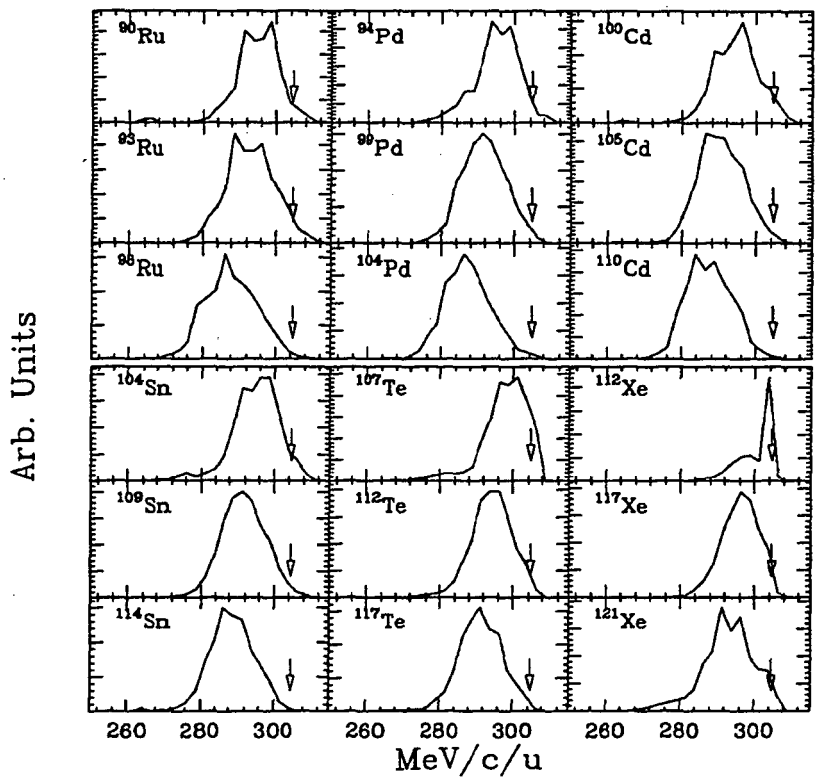

Figure 3.2: Momentum distributions for representative light, medium, and heavy isotopes of selected elements for the 50 MeV/nucleon ^{129}Xe+C reaction. The arrow is at the momentum of the beam in each frame. The momentum of the center of mass for this system is 278.7 MeV/c/u.

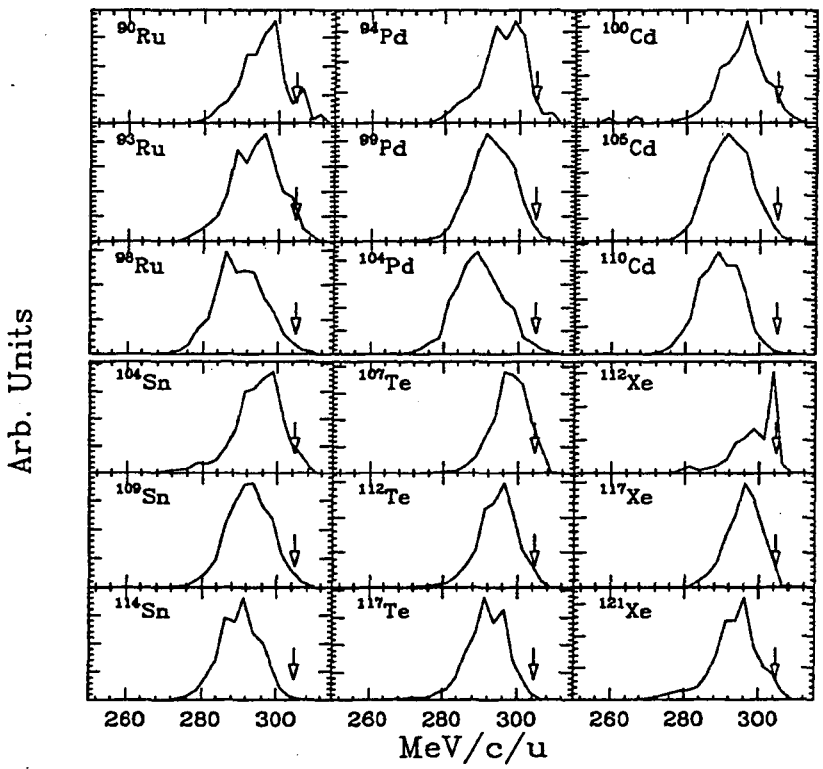

Figure 3.3: Momentum distributions for representative light, medium, and heavy isotopes of selected elements for the 50 MeV/nucleon ^{129}Xe+Be reaction. The arrow is at the momentum of the beam in each frame. The momentum of the center of mass for this system is 284.8 MeV/c/u.

and 3.7. This peak arises from (elastic) scattering of the incident beam. The yield of fragments with low Z values increases as the target mass increases at a given beam energy (see Figure 3.7). The yield of these light fragments also increases as the beam energy increases. Both of these trends parallel an increase in center-of-mass energy, as shown in Table 3.1. Generally, events with high excitation energies emit a larger number of particles while de-exciting than do events with low excitation energies and this leads to increased yields of lower Z value elements.

Table 3.1: Maximum excitation energy possible for each beam energy and target combination (in MeV).

Beam Energy/Target	Be	C	Al
26 MeV/nucleon	220	285	580
40	335	440	890
50	420	550	1115

Figures 3.8, 3.9, and 3.10 show contours of the isotopic cross sections in the A versus Z plane. The stable isotopes are marked with filled squares in these figures. The stair-stepping line indicates the proton-rich limit of the known nuclei. These figures clearly show that the isotopes produced in these reactions all have lower A/Z ratios than the stable nuclei indicating substantial neutron evaporation. Also visible in these figures is the increasing yield of low Z value fragments with increasing center-of-mass energy.

In Figure 3.11, the average mass of each element is shown for the 50 MeV/nucleon ^{129}Xe + Be, C, and Al reactions. In the lower portion of this figure, the width of the mass distribution for each element is shown. This figure shows that the average mass and the width of the mass distribution for each element are independent of the

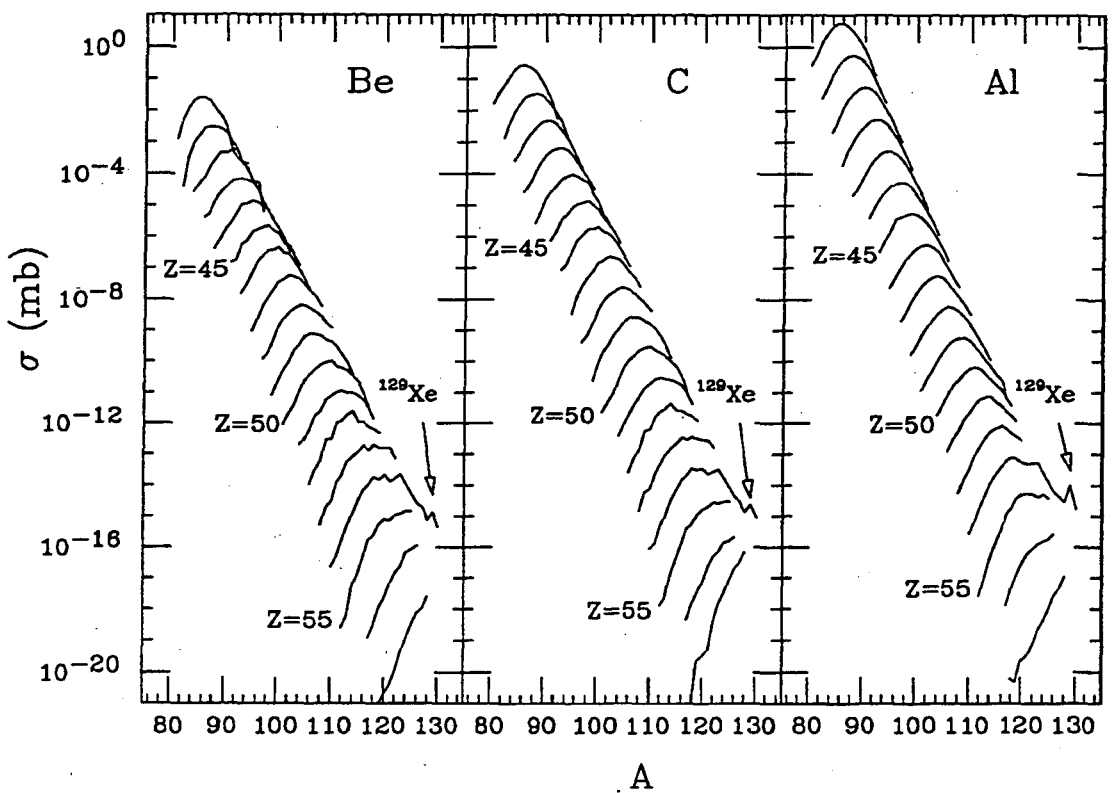

Figure 3.4: Isotopic cross sections for the 50 MeV/nucleon reactions. The curves join the cross sections for all the isotopes of a given element. All curves, except that for Z=40, are offset from their neighbors by an order of magnitude so that they do not overlap.

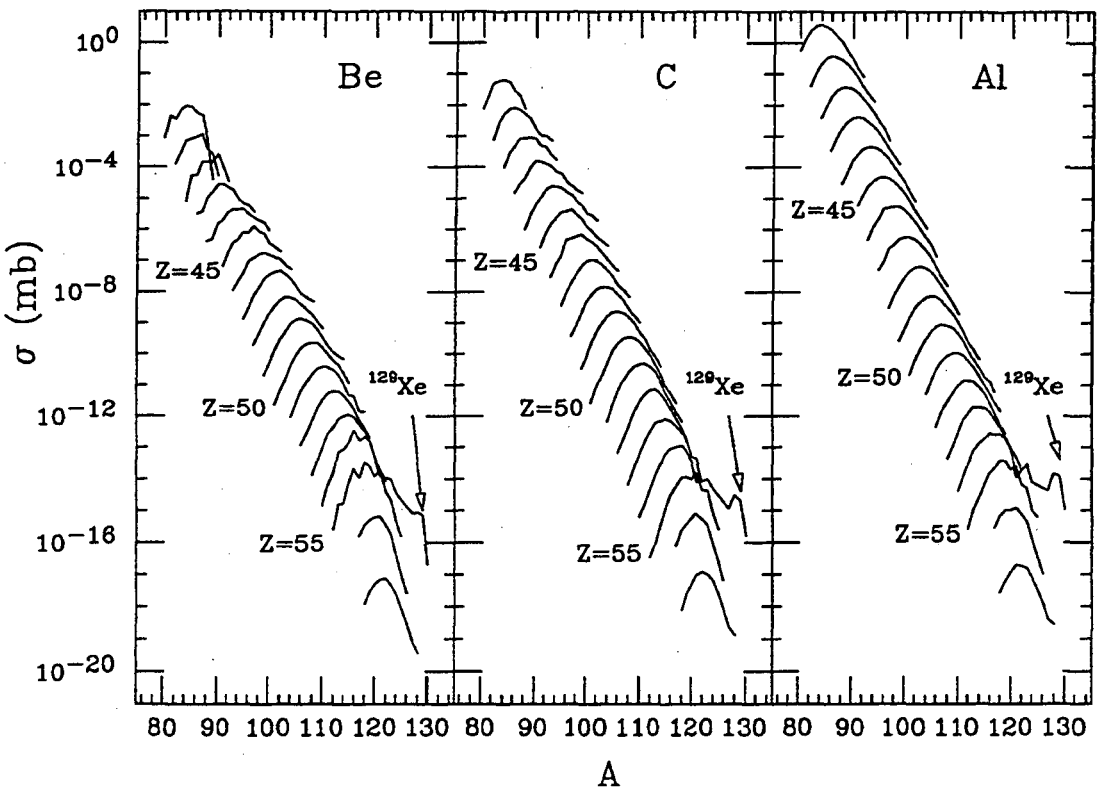

Figure 3.5: Isotopic cross sections for the 40 MeV/nucleon reactions. The curves join the cross sections for all the isotopes of a given element. All curves, except that for Z=40, are offset from their neighbors by an order of magnitude so that they do not overlap.

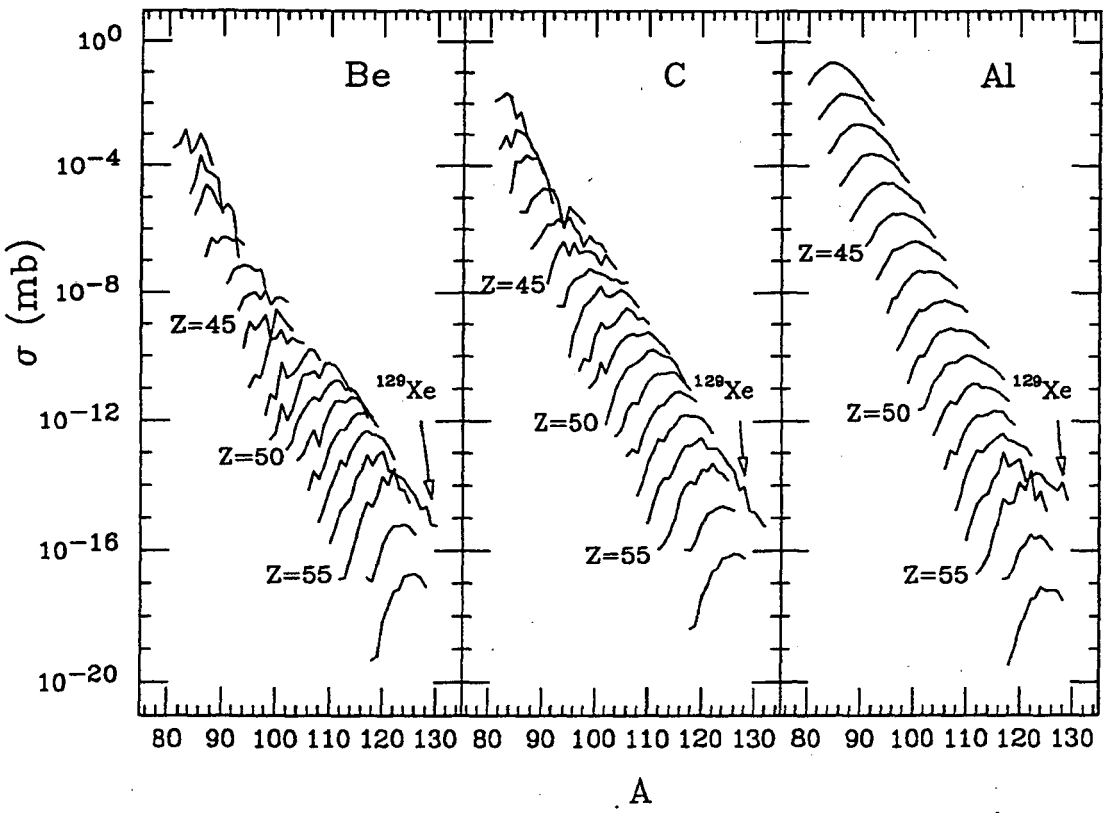

Figure 3.6: Isotopic cross sections for the 26 MeV/nucleon reactions. The curves join the cross sections for all the isotopes of a given element. All curves, except that for Z=40, are offset from their neighbors by an order of magnitude so that they do not overlap.

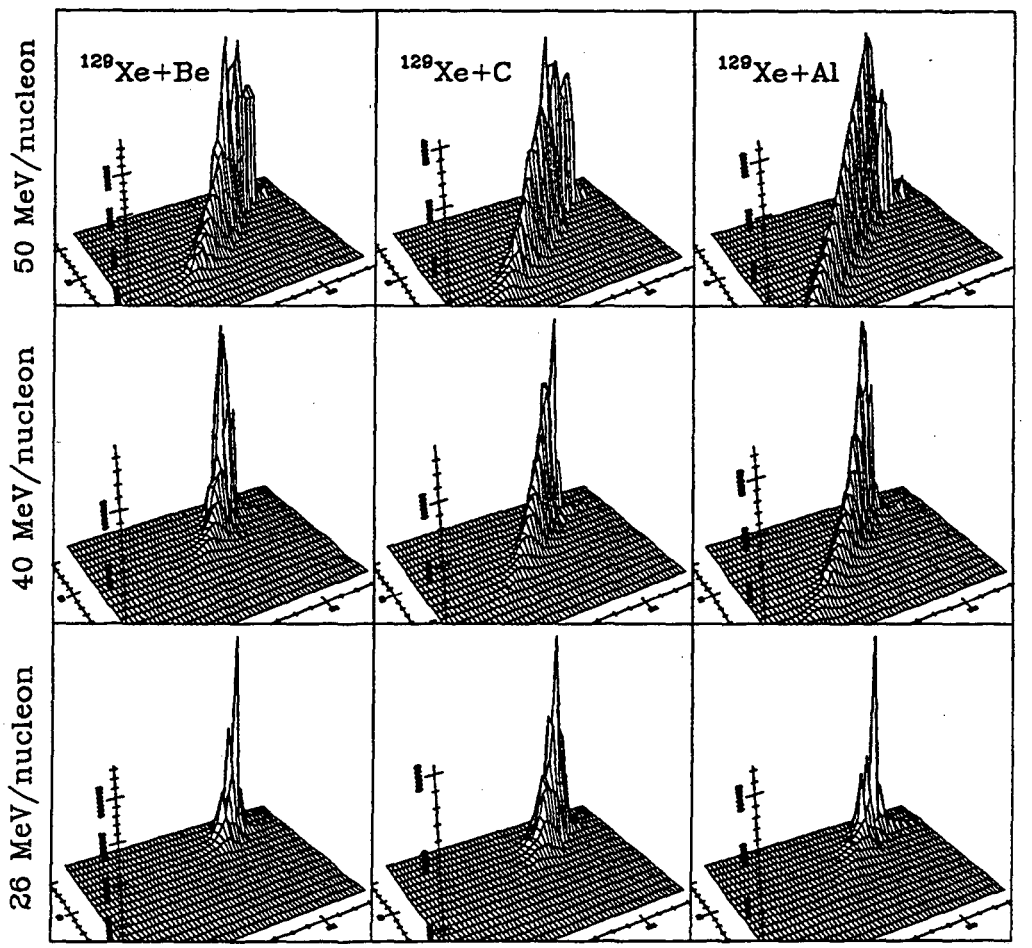

Figure 3.7: The three-dimensional surface of the isotopic cross sections are shown. Note the variation of the shape of the surface with target and bombarding energy. The axis going to the right represents A, that going to the left represents Z, and the vertical axis represents yield.

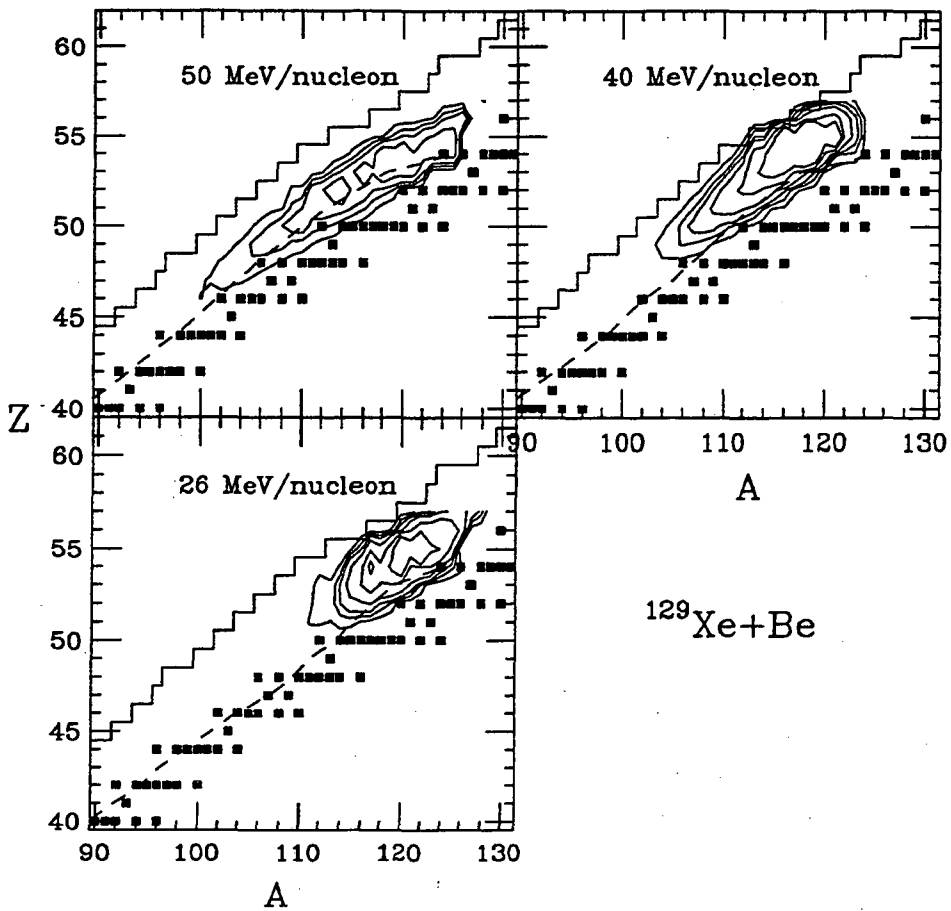

Figure 3.8: Contour plots of the isotopic cross sections in the A versus Z plane for the ^{129}Xe + Be reaction. Filled squares indicate the positions of the stable isotopes. The stair-stepping line shows the proton-rich limit of the known isotopes. The dashed curve just to the proton-rich side of the stable isotopes is the result from an incomplete fusion calculation (see Section 4.2.1).

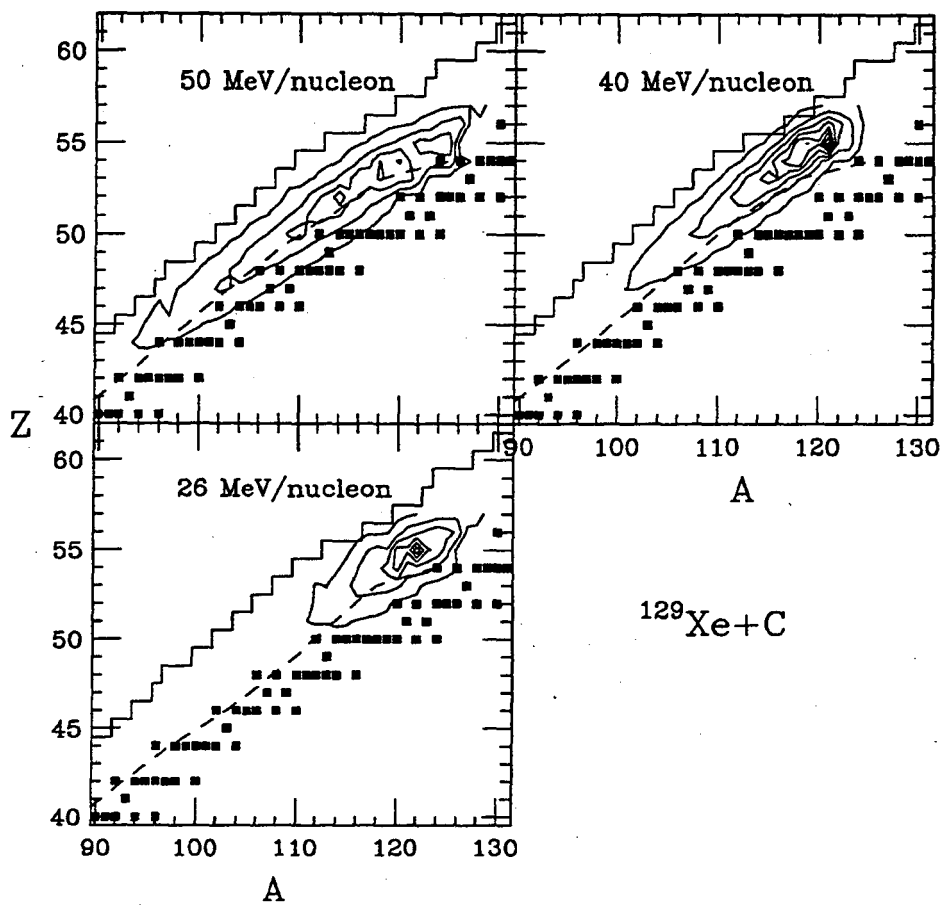

Figure 3.9: Contour plots of the isotopic cross sections in the A versus Z plane for the ^{129}Xe + C reactions. Filled squares indicate the positions of the stable isotopes. The stair-stepping line shows the proton-rich limit of the known isotopes. The dashed curve just to the proton-rich side of the stable isotopes is the result from an incomplete fusion calculation (see Section 4.2.1).

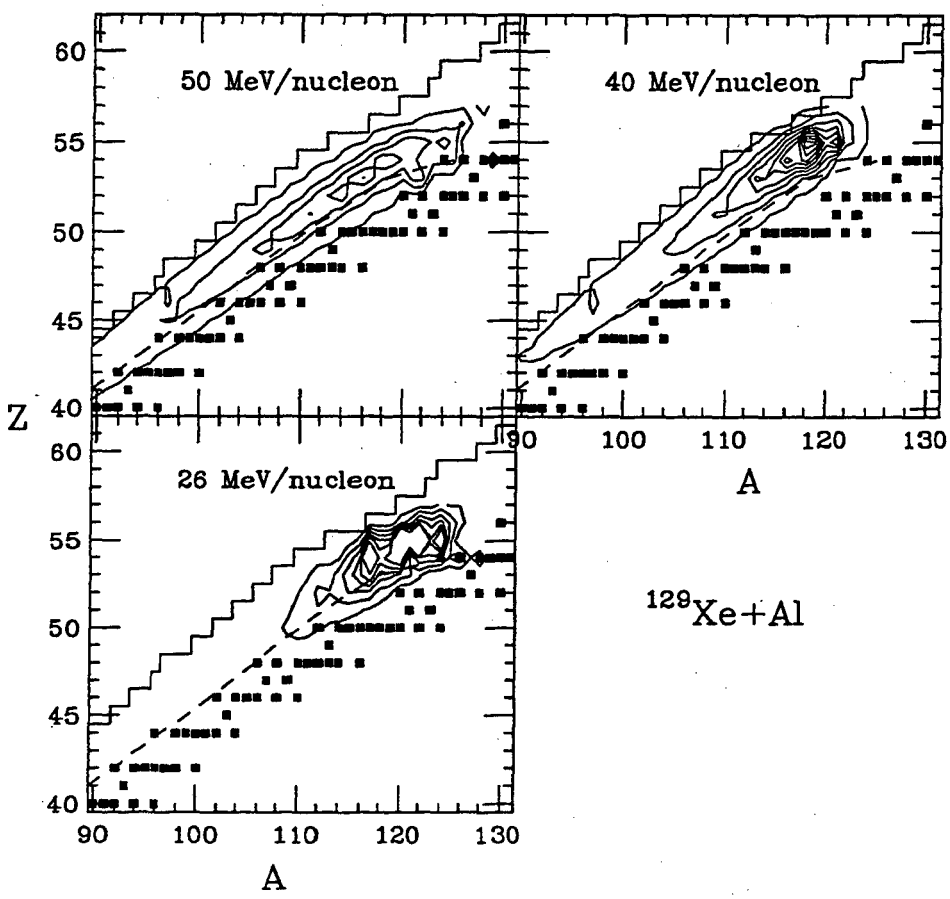

Figure 3.10: Contour plots of the isotopic cross sections in the A versus Z plane for the ^{129}Xe + Al reactions. Filled squares indicate the positions of the stable isotopes. The stair-stepping line shows the proton-rich limit of the known isotopes. The dashed curve just to the proton-rich side of the stable isotopes is the result from an incomplete fusion calculation (see Section 4.2.1).

target. A similar target independence is also seen for the other two beam energies.

Previous γ-ray spectroscopy studies of heavy residues have extracted the average Z value for each isobar. The line following the average Z value for each isobar is comparable to the ridge in the isotopic cross section distribution from the current data set. Similar energy ^{12}C + $^{107-109}$Ag reactions have been studied using γ-ray spectroscopy [chu91]. This allows a comparison between the ^{12}C + Ag data and the present ^{129}Xe + C data. In Figure 3.12, the average Z value for each isobar from the reaction of ^{12}C + Ag [chu91] (diamonds) is compared with the isotopic cross section distributions from the ^{129}Xe + C (contours) reactions measured with the A1200 spectrometer. Although the ranges of elements measured only partially overlap, it is clear that the isotopes produced in the ^{129}Xe-induced reactions are significantly more proton-rich than those produced in the ^{12}C + Ag reaction. The ^{12}C + Ag reaction products become less proton-rich with increasing bombarding energy, whereas the yields from the ^{129}Xe + C data show no such dependence on the bombarding energy. These differences may be the result of the inability of the γ-ray spectroscopy to measure very short-lived nuclei; however, it is difficult to prove that this is the cause of the differences.

A previous study measured part of the isotopic yields from the 70 MeV/nucleon ^{92}Mo + ^{58}Ni reaction [yen92]. These yields are shown as histograms in Figure 3.13. Since this system was studied using a magnetic spectrometer, it is not subject to the experimental restrictions of the γ-ray spectroscopy. (For discussion of these restrictions, see Section 1.4.1.) However, these data were collected over a narrow range of magnetic rigidities and may be biased towards those nuclei with $A = 2Z$. For comparison, the isotopic cross sections for the same elements from the 50 MeV/nucleon ^{129}Xe+Al reaction are shown as continuous curves. The centroid values of these dis-

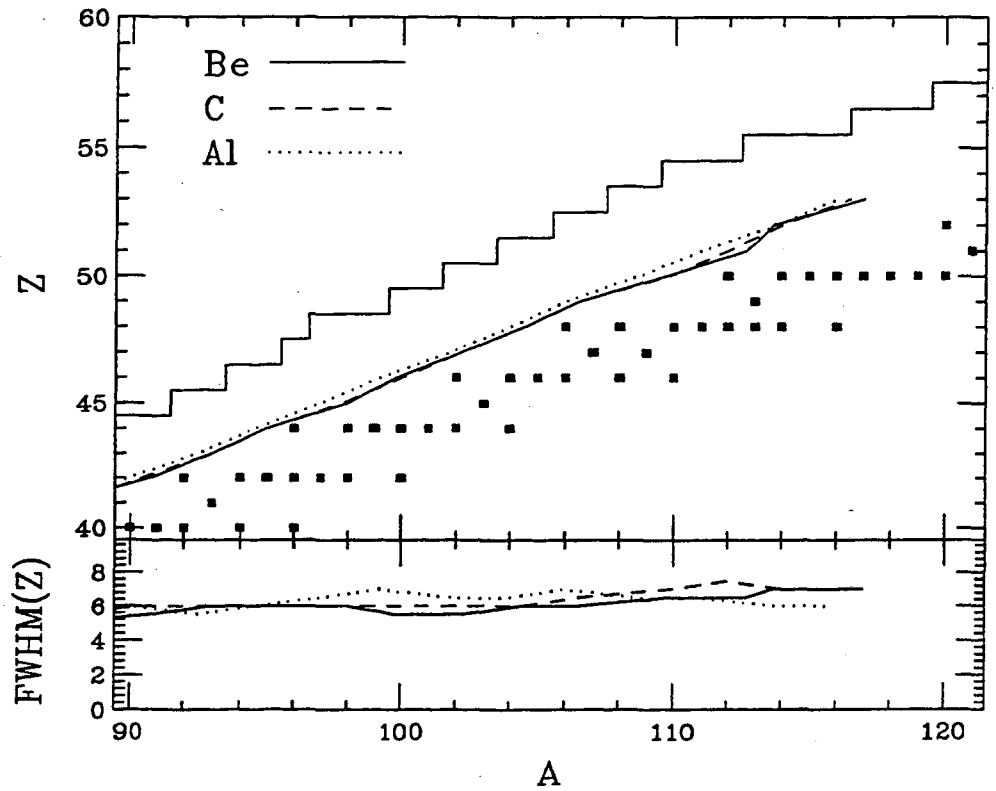

Figure 3.11: The average A and the full width at half maximum (FWHM) of the A distribution for each element from the 50 MeV/nucleon ^{129}Xe + Be (solid), C (dashed), and Al (dotted) reactions. Note the independence of the average and width of the A distribution on the target. The stair-stepping line shows the proton-rich limit of the known isotopes. Filled squares represent the positions of the stable isotopes.

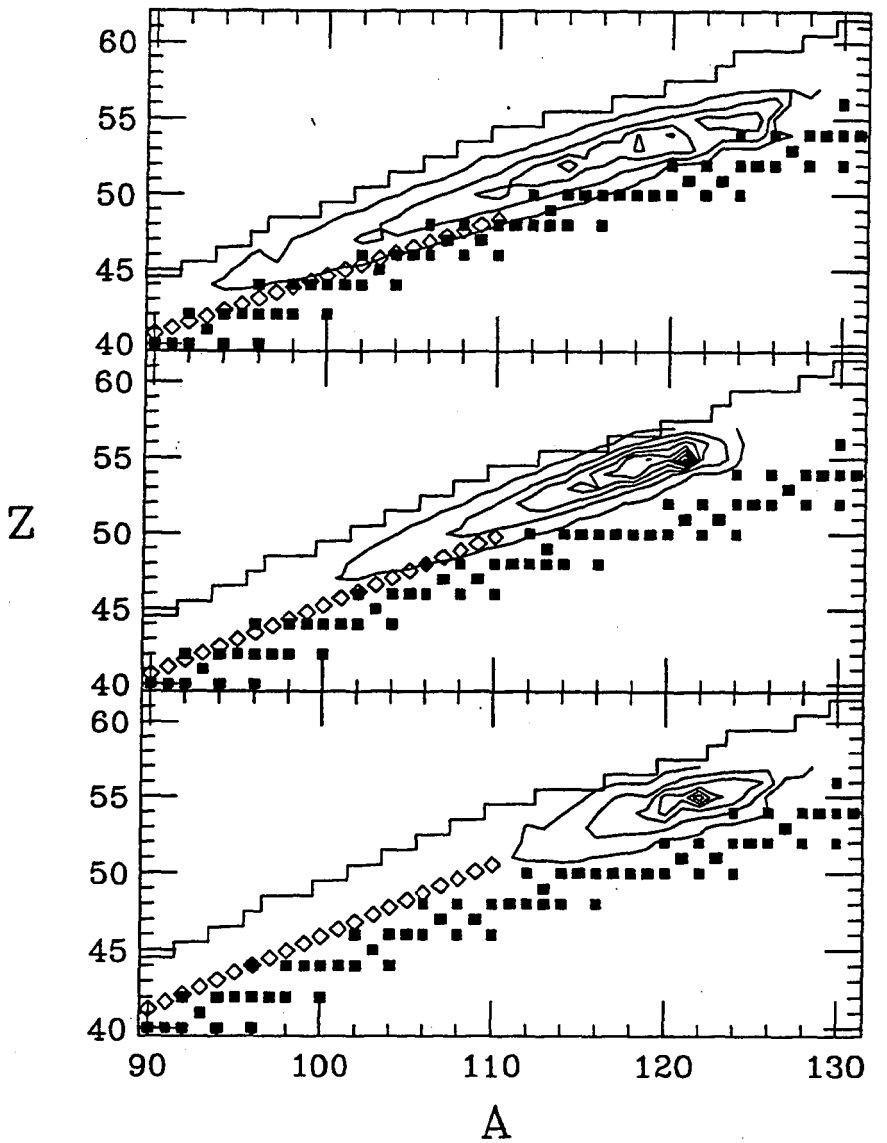

Figure 3.12: Contour plots of the isotopic cross sections in the A versus Z plane. In all three panels, the filled squares represent the positions of the stable isotopes, the stair-stepping line shows the proton-rich limit of the known isotopes, and the diamonds on the proton-rich side of the stable isotopes are the average atomic number for each isobar from the reaction of C + Ag measured by Chung, Chu, and Porile [chu91]. The top frame compares the results from the reactions of 50 MeV/nucleon ^{129}Xe + C and 45 MeV/nucleon ^{12}C + Ag, the middle frame contains the results of 40 MeV/nucleon ^{129}Xe + C and 35 MeV/nucleon ^{12}C + Ag, and the bottom frame shows the results from 26 MeV/nucleon ^{129}Xe + C and 25 MeV/nucleon ^{12}C + Ag.

tributions are similar, but the isotopes produced in the ^{92}Mo + ^{58}Ni reaction are slightly more proton-rich, as might be expected given the more proton-rich target and projectile combination.

3.3 Elemental and Isobaric Yields

Previous studies of similar systems have measured the elemental and isobaric cross sections. In this study, the isotopic cross sections can be obtained by integrating the isotope's momentum distribution. The isotopic cross sections for all of the isotopes of each element can be summed to produce the elemental cross sections. These elemental cross sections are shown by the diamonds in Figures 3.14, 3.15, and 3.16. The elemental cross section distributions become wider at higher beam energies and for heavier target nuclei. This effect was seen in the isotopic yields for isotopes with low Z values. Previous measurements of the elemental cross sections from similar systems are plotted as pluses [han93,bow89,rou93]. Note that the cross sections measured in the present work cover a range of elements not measured in the complex fragment studies. Although the elements that have been previously measured do not significantly overlap the current data, the two data sets seem to be consistent. Notice that a large fraction of the total reaction cross section was missed in the previous studies of complex fragments.

The isobaric cross sections are the most accurately determined yields from γ-ray spectroscopy studies because the calculation of these yields requires the smallest number of assumptions. The isotopic cross sections for all the isotopes of each isobar from the present study were summed to produce isobaric cross sections. These isobaric cross sections are shown by the continuous curves in Figure 3.17. Also shown in

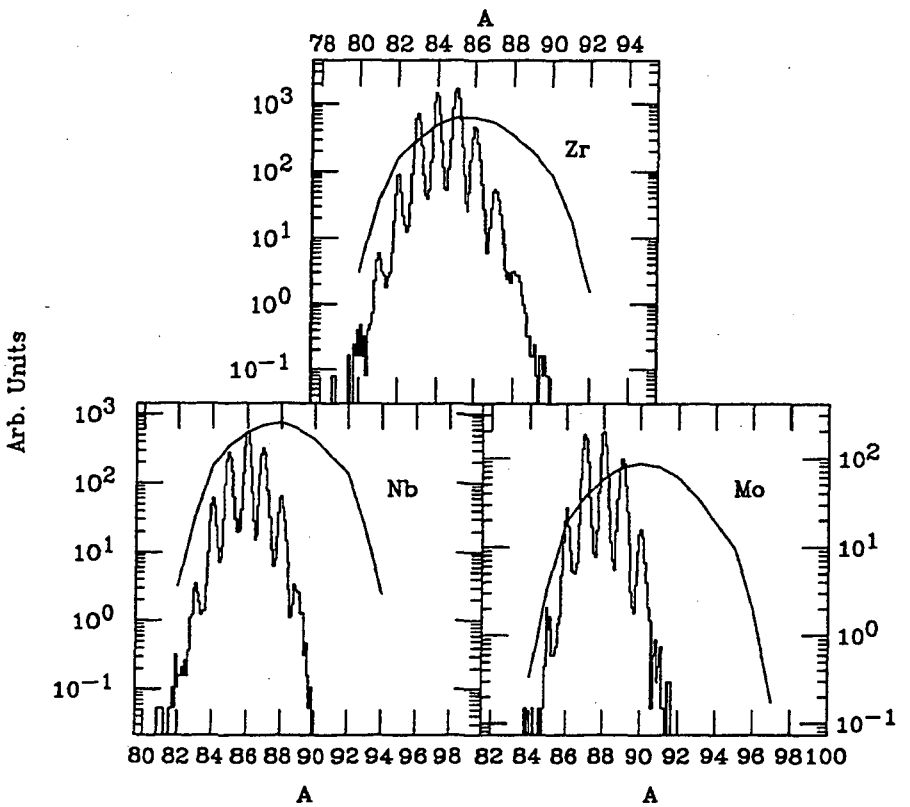

Figure 3.13: The mass yields from the 50 MeV/nucleon Xe+Al reaction are shown by the solid curves. The mass yields from the 70 MeV/nucleon ^{92}Mo+^{58}Ni reaction [yen92] are indicated by the histograms.

Figure 3.17 are the isobaric cross sections (measured using γ-ray spectroscopy) from 30 MeV/nucleon ^{14}N + ^{124}Sn, 49 MeV/nucleon ^{12}C + ^{124}Sn, 30 MeV/nucleon ^{20}Ne + ^{124}Sn, 40 MeV/nucleon ^{20}Ne + ^{124}Sn, 49 MeV/nucleon ^{20}Ne + ^{124}Sn, 27 MeV/nucleon ^{40}Ar + ^{124}Sn, 35 MeV/nucleon ^{40}Ar + ^{124}Sn, and 44 MeV/nucleon ^{40}Ar + ^{124}Sn from Lleres [lle88]. These data sets are shown as pluses and times symbols with the ^{129}Xe-induced reaction from the present work that most closely approximates the ^{124}Sn reaction. Since the reactions presented for comparison have similar target and projectile masses and bombarding energies and the center-of-mass energy is large in all cases, the nuclear structure effects for a particular beam and target combination should be minimized and the resulting isobaric cross sections should be and generally are similar. The ^{129}Xe + Al data compares better with the ^{20}Ne + ^{124}Sn results than with the ^{40}Ar + ^{124}Sn results. This is reasonable because the excitation energy of the compound nucleus rapidly increases with the mass–symmetry of the entrance channel. There remains a deficit in the isobaric yields from the γ-ray spectroscopy studies. Such a deficit maybe due to the difficulty of measuring nuclei near stability with the γ-ray technique.

Figures 3.14, 3.15, 3.16, and 3.17 show that the shapes of the cross section distributions for the present and previous studies are similar. This agreement is consistent within the experimental uncertainties associated with the different measurements. The data from the present study at 26 MeV/nucleon appears to be low in comparison to the previous work. This may be due to the complications of measuring many atomic charge states at the lowest beam energy. Such agreement also gives confidence in proceeding to compare the absolute cross sections with the results of model calculations. (See Chapter 4.)

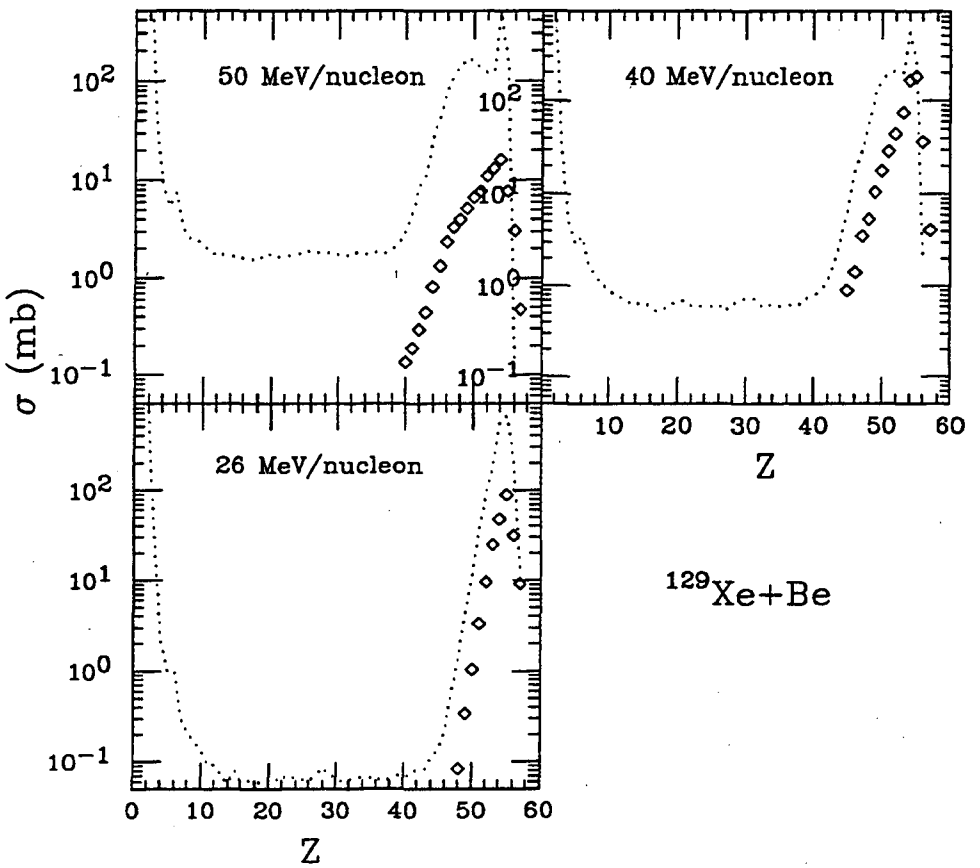

Figure 3.14: The elemental cross sections for ^{129}Xe + Be are shown as diamonds. Shown as a dotted line are the elemental cross sections from an incomplete fusion model calculation (see Section 4.2.1).

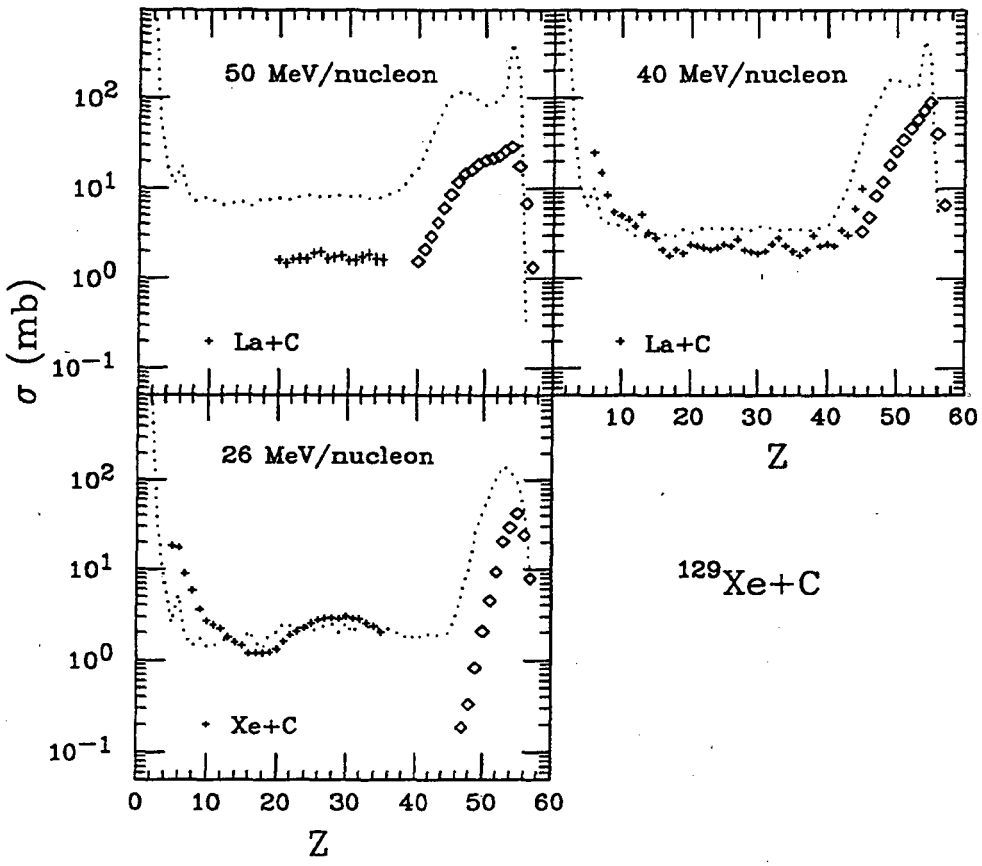

Figure 3.15: The elemental cross sections for ^{129}Xe + C are shown as diamonds. Complex fragment cross sections from 40 and 50 MeV/nucleon ^{139}La + C and 26 MeV/nucleon ^{129}Xe + C are shown as pluses. Shown as a dotted line are the elemental cross sections from an incomplete fusion model calculation (see Section 4.2.1).

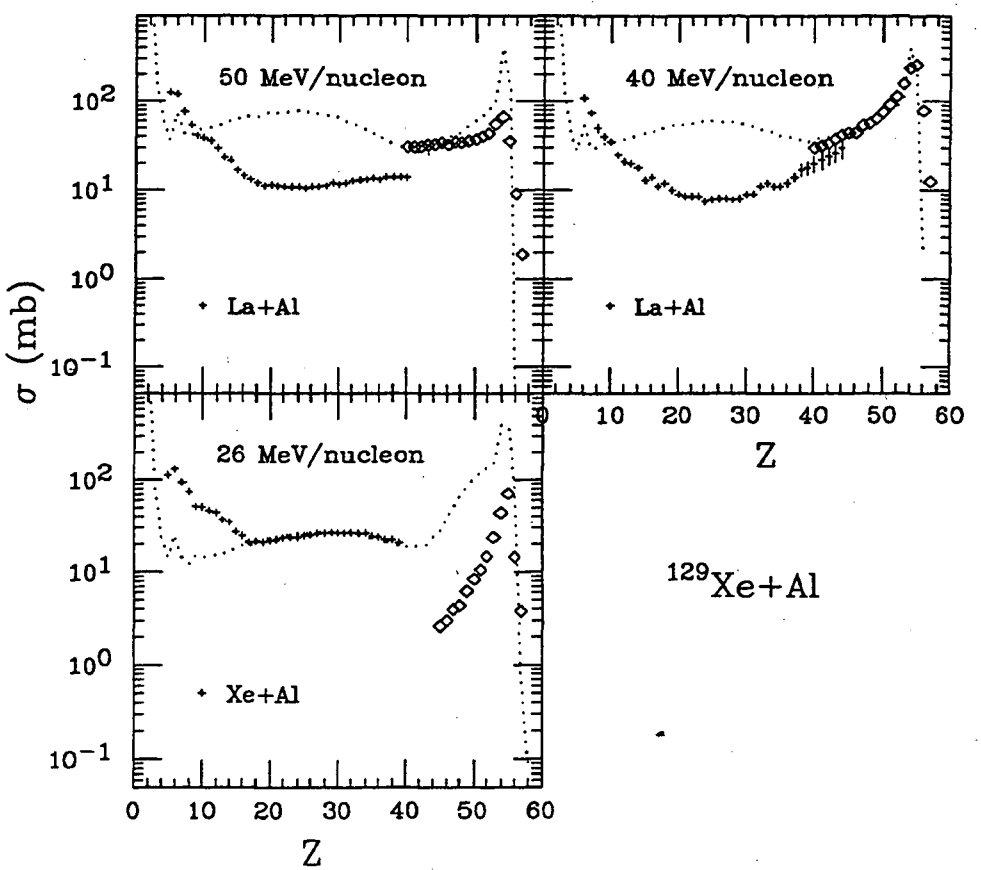

Figure 3.16: The elemental cross sections for ^{129}Xe + Al are shown as diamonds. Complex fragment cross sections from 40 and 47 MeV/nucleon ^{139}La + Al and 26 MeV/nucleon ^{129}Xe + Al are shown as pluses. Shown as a dotted line are the elemental cross sections from an incomplete fusion model calculation (see Section 4.2.1).

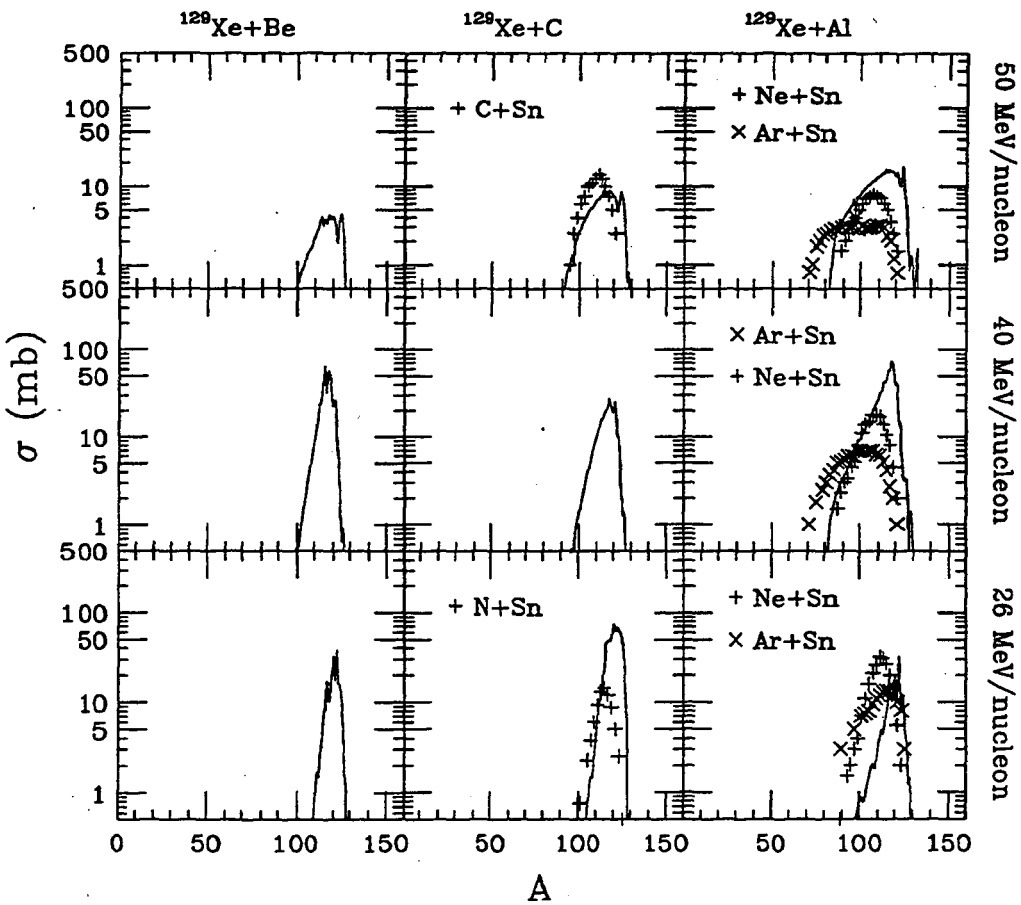

Figure 3.17: The isobaric cross sections for each of the target-beam energy combinations from this work are shown by the curves. Also shown as pluses and times symbols are the cross sections from 30 MeV/nucleon ^{14}N + ^{124}Sn, 49 MeV/nucleon ^{12}C + ^{124}Sn, 30 MeV/nucleon ^{20}Ne + ^{124}Sn, 40 MeV/nucleon ^{20}Ne + ^{124}Sn, 49 MeV/nucleon ^{20}Ne + ^{124}Sn, 27 MeV/nucleon ^{40}Ar + ^{124}Sn, 35 MeV/nucleon ^{40}Ar + ^{124}Sn, and 44 MeV/nucleon ^{40}Ar + ^{124}Sn [Hess] as indicated in each panel.

3.4 Z versus Velocity Distributions

Previous studies of complex fragment emission have presented distributions of Z_{total} versus $\mathbf{v}_{source}$ [col89,han93,del91,rou93]. These distributions were used to determine the velocity of the source of the complex fragments. Similar information about the source of the heavy residues in the present work can be extracted by integrating the isotopic momentum distributions over A and converting momentum to velocity to produce Z value versus velocity distributions. These distributions for all the reaction systems in the present work are shown in Figure 3.18. For comparison, complimentary data taken from 26 MeV/nucleon ^{129}Xe + C and Al [han93], 40 MeV/nucleon ^{139}La + C and Al [rou93], and 50 MeV/nucleon ^{129}Xe + C and Al [pea93] are also shown. (The ^{139}La data has been shifted down by 3 units of Z to account for the difference in Z values between $^{139}_{57}$La and $^{129}_{54}$Xe.) The data at higher velocity in each frame in Figure 3.18 are from this work; the data at lower velocities, noted with "CF", are taken from the referenced complex fragment studies. Figure 3.18 clearly shows the complimentary nature of the present measurements to the studies of the complex fragments. The cross section contours mesh together well and indicate that a complete measurement of the reaction requires both techniques.

3.5 Summary of the Data

The data for the ^{129}Xe–induced reactions was presented and compared to similar data from previous measurements of similar reaction systems. In general, the new data is consistent with the previous data. The new information available in the present data includes the elemental cross sections for the high Z value elements ($Z \geq 39$), the yield

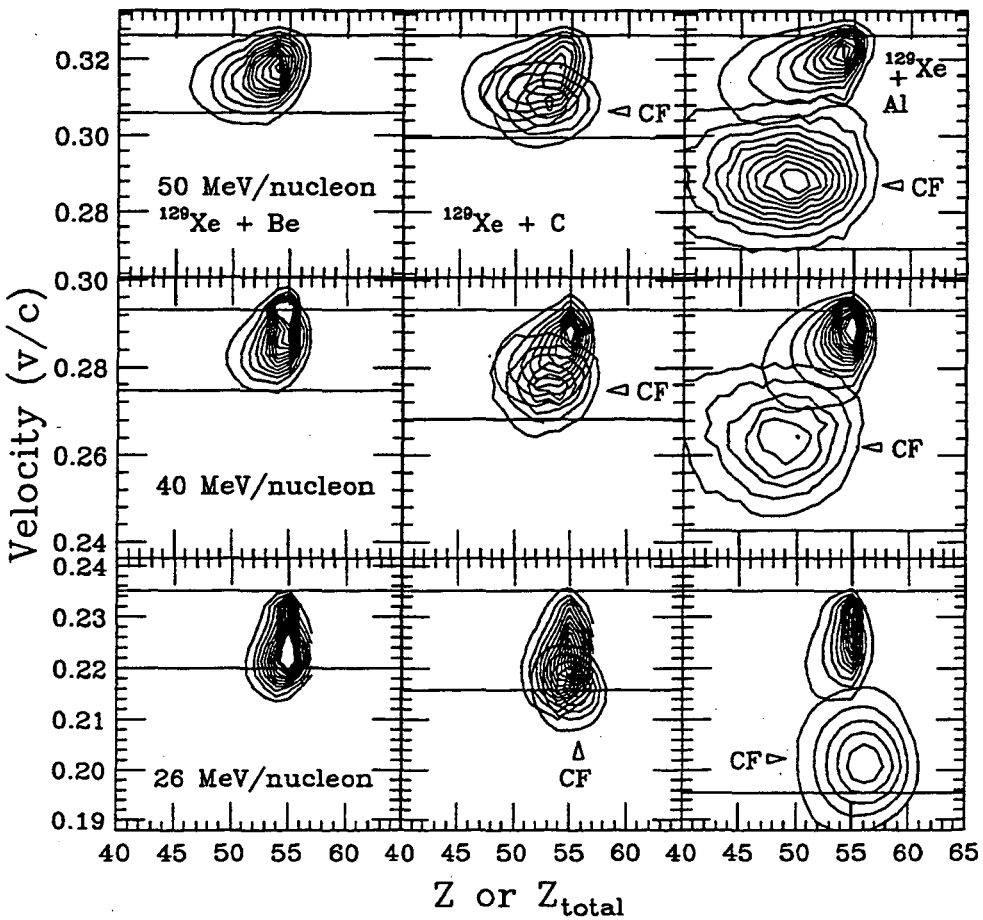

Figure 3.18: Cross section contours in the Z–velocity plane for all systems measured in this work. Also shown are complex fragment ("CF") data from 26 MeV/nucleon ^{129}Xe+C and Al [han93], 40 MeV/nucleon ^{139}La+C and Al [rou93], and 50 MeV/nucleon ^{129}Xe+C and Al [pea93]. The upper horizontal line in each frame lies along the velocity of the beam. The lower horizontal line in each frame lies along the velocity of the center of mass for that system.

of fragments at velocities near that of the beam, the isotopic cross sections for part of the elemental yield range ($Z \geq 39$), and the momentum distributions for the high Z value isotopes. By combining the present data with the previous data, elemental cross sections from Z=6 to Z=57 are available. The present experiment measured fragments with a range of velocities not seen in the complex fragment data.

Chapter 4

Discussion of data and models

Previous studies of the 14 to 50 MeV/nucleon ^{129}Xe + C and ^{139}La + C reactions have demonstrated that one source of complex fragments is the statistical decay of a compound nucleus [cha88a,bow89,rou93,han93]. At low bombarding energies ($E/A < 25$ MeV), the compound nucleus is formed in complete fusion reactions. At higher bombarding energies ($E/A > 30$ MeV), incomplete fusion of the reaction partners forms a range of compound nuclei with different masses and excitation energies. The complex fragments from these reactions have isotropic center-of-mass angular distributions ($d\sigma/d\theta$) and center-of-mass emission velocities dominated by the Coulomb repulsion of the two decay partners. These two features indicate a relaxed and long-lived source (source lifetime $\gg$ rotational period). In addition, the source velocities ($\mathbf{v}_{source}$) extracted from analysis of both single-particle inclusive data and coincidence data are consistent and fall within the range expected from the complete or incomplete fusion reaction mechanism. The $\mathbf{v}_{source}$ is used to calculate the amount of transferred mass and the excitation energy, which in turn is used in a statistical de-excitation model to calculate the complex fragment production cross sections. The agreement between the experimental and predicted cross sections, angular distributions, and emission

velocities shows the validity of the compound nucleus source assumption.

As the present experiment is able to detect all the heavy residues produced in these reactions, several new questions can be addressed:

1. From the experimental standpoint, do the heavy residues come from the same source as the complex fragments, or do they result from a different source?

2. From the theoretical standpoint, if the heavy residues have the same source as the complex fragments, can the models that successfully predicted the complex fragment production also predict the heavy residue production?

3. From the practical standpoint, what is the source of the extremely proton-rich nuclei discovered recently? The newly discovered nuclei are ^{61}Ga, ^{62,63}Ge, ^{65}As, ^{66}Se, ^{69}Br, and ^{75}Sr from 65 MeV/nucleon ^{78}Kr + ^{58}Ni [moh91,win93]; ^{78}Y, ^{82}Nb, ^{84,85}Mo, ^{86}Tc, and ^{89,90}Ru from 70 MeV/nucleon ^{92}Mo + ^{58}Ni [yen92]; ^{94,95}Ag from 70 MeV/nucleon ^{106}Cd + ^{58}Ni [mor94]; and ^{101,102}Sn from 58 MeV/nucleon ^{112}Sn + Ni [lew93]. These nuclei are important to nuclear structure studies, and understanding their production mechanism would facilitate these studies.

To address these questions, the data are first qualitatively examined for signatures of the reaction mechanism (Section 4.1). Then, two models of the reaction mechanism are compared to the previous and present data sets to test how well these models quantitatively describe the data (Section 4.2). It will be shown that the isotopic cross sections and momentum distributions from the present study do, in fact, provide a new, previously unavailable test of reaction model predictions.

4.1 The Velocity as a Function of Z

In previous complex fragment studies, two-dimensional distributions of the cross section as a function of Z_{total} and $\mathbf{v}_{source}$ have been created. Z_{total} and $\mathbf{v}_{source}$ are the total charge and the center-of-mass velocity of the detected complex fragments, respectively. There are typically one to five heavy fragments and many light fragments in the exit channel of the studied reactions. The heavy fragments move relative to one another with a well-defined velocity determined mainly by the Coulomb repulsion energy between the fragments. The evaporation of light particles either preceding or following the heavy fragment emission acts mainly to perturb the sharpness of the $\mathbf{v}_{source}$ distribution. The kinematic skeleton of the source breakup is not altered by isotropic ($d\sigma/d\Omega$) evaporation. Thus, the $\mathbf{v}_{source}$ corresponds to the velocity of the emitting source. For complete fusion reactions, $\mathbf{v}_{source}$ is equal to the velocity of the center of mass ($\mathbf{v}_{cm}$). In incomplete fusion reactions, only a fraction of the lighter nucleus fuses with the heavier nucleus. When the projectile is larger than the target, $\mathbf{v}_{source}$ is larger than $\mathbf{v}_{cm}$ but smaller than the velocity of the beam ($\mathbf{v}_{beam}$). The $\mathbf{v}_{source}$ is near the $\mathbf{v}_{beam}$ for small mass transfers, and the $\mathbf{v}_{source}$ is near the $\mathbf{v}_{cm}$ for nearly complete mass transfers. Therefore, an accurate determination of $\mathbf{v}_{source}$ should allow one to infer the amount of mass transferred.

For the 18 MeV/nucleon ^{139}La+C and the 26 and 31 MeV/nucleon ^{129}Xe + C reactions [col89,cha88a,han93], a single peak was observed in the reconstructed $\mathbf{v}_{source}$ distribution. Its centroid is at $\mathbf{v}_{cm}$. The isotropic center-of-mass angular distributions ($d\sigma/d\theta$), the Coulomb–repulsion–dominated emission velocities, and the elemental cross sections of the complex fragments are all consistent with these reactions being

dominated by complete fusion processes that result in compound nuclei. For the Xe(La) + Al and higher energy Xe(La) + C reactions (18 MeV/nucleon ^{139}La + Al, 26 and 31 MeV/nucleon ^{129}Xe + Al, and 35 to 55 MeV/nucleon ^{139}La+ C, Al reactions [cha88a,han93,rou93,pea93,bow89]), again a single peak in the $\mathbf{v}_{source}$ distribution was observed, but the centroid value was between the values of $\mathbf{v}_{cm}$ and $\mathbf{v}_{beam}$, consistent with an incomplete fusion reaction mechanism. For the Xe(La) + Ti, Ni, and Cu reactions (18 MeV/nucleon ^{139}La + Ti and Ni reactions and 26 and 31 MeV/nucleon ^{129}Xe + Ti and Cu [col89,han93]), a range of values for $\mathbf{v}_{source}$ was observed, suggesting a broad range of mass transfers resulting from incomplete fusion reactions.

In the studies mentioned above, complex fragments emitted from compound nuclei have been detected. However, these compound nuclei can also de-excite by emitting only light particles ($Z \leq 2$), leaving a single cold heavy residue. For low excitation energies, complex fragment emission is an unlikely de-excitation process; thus, experiments that measure only the complex fragment production cross sections have missed a large portion of the primary yield. The Z_{total} versus $\mathbf{v}_{source}$ distribution for complex fragment coincidence events should have the same correlations as the Z value versus velocity distributions for the heavy residues, since both evaporation residues and complex fragments can result from the same nuclear reaction mechanism. The experimentally determined Z value versus velocity distributions for the heavy residues are shown in Figure 3.18. The distributions of Z_{total} versus the $\mathbf{v}_{source}$ derived from the complex fragment coincidence events from similar reactions (26 MeV/nucleon ^{129}Xe + C, Al [han93], 40 MeV/nucleon ^{139}La + C, Al [rou93], and 50 MeV/nucleon ^{129}Xe + C, Al [pea93]) are also shown in Figure 3.18. The $^{139}_{57}$La data have been shifted down by 3 units of Z to account for the difference in the atomic numbers between the $^{129}_{54}$Xe

and $^{139}_{57}$La projectiles.

The shapes of the Z value versus velocity distributions qualitatively support the incomplete fusion reaction mechanism, as illustrated in Figure 4.1. The solid line represents the range of values of velocity and Z value for the primary products that result from the incomplete fusion reactions of a large projectile nucleus with a small target nucleus. The excitation energy of these products increases systematically with decreasing velocity. The amount of excitation energy depends directly on the amount of mass transferred and on the bombarding energy. Tables 4.1 and 4.2 show the excitation energies for ^{6}Li and ^{12}C transfers at 26, 40, and 50 MeV/nucleon in the ^{129}Xe + Al reaction. The excitation energies are calculated using the incomplete fusion model described in Section 4.2.1.1. This excitation energy is lost primarily

Table 4.1: Excitation energy and average residue Z value for the transfer of a ^{6}Li to form ^{135}La in the ^{129}Xe + Al reaction.

Beam Energy (E/A)	Excitation Energy (MeV)	Average Residue Z Value
26 MeV	175	53.5
40	250	52.0
50	310	50.8

Table 4.2: Excitation energy and average residue Z value for the transfer of a ^{12}C to form ^{141}Nd in the ^{129}Xe + Al reaction.

Beam Energy (E/A)	Excitation Energy (MeV)	Average Residue Z Value
26 MeV	320	53.6
40	470	50.6
50	580	48.2

through evaporation. Statistical decay calculations show that, on average, a charge is evaporated for approximately every 50 MeV of excitation energy. Using this result, the average evaporation residue Z value can be calculated. The result of this calculation is also shown in Tables 4.1 and 4.2. Notice that the same mass transfer at a higher bombarding energy results in higher excitation energy and a lower average residue Z value. In Figure 4.1, the dotted line qualitatively indicates the nuclear charge of the incomplete fusion residues after evaporation for a low bombarding energy. As the bombarding energy increases, the excitation energy produced in the reaction increases and the locus of the final fragments rotates clockwise because of increased charged-particle evaporation. The two dashed lines schematically indicate the nuclear charge after evaporation for two higher bombarding energies.

The heavy residue data from the 26 MeV/nucleon reactions have almost no variation in the centroid value of the Z distribution as a function of velocity. This indicates that there is a balance between the charge gained in the incomplete fusion process and the charge lost via evaporation during the de-excitation. In the higher energy reactions, the centroid value of the Z distribution decreases as the velocity decreases, indicating that more charge is lost by evaporation than is gained in the incomplete fusion process.

The incomplete fusion reaction mechanism also qualitatively explains the range of velocities seen for each data set in Figure 3.18. Within a given bombarding energy, small mass transfers result in primary fragments with high velocities, small amounts of excitation energy, and low angular momenta. The low excitation energy and angular momentum give the resulting compound nucleus a low complex fragment emission probability, and thus a large probability of producing an evaporation residue. In

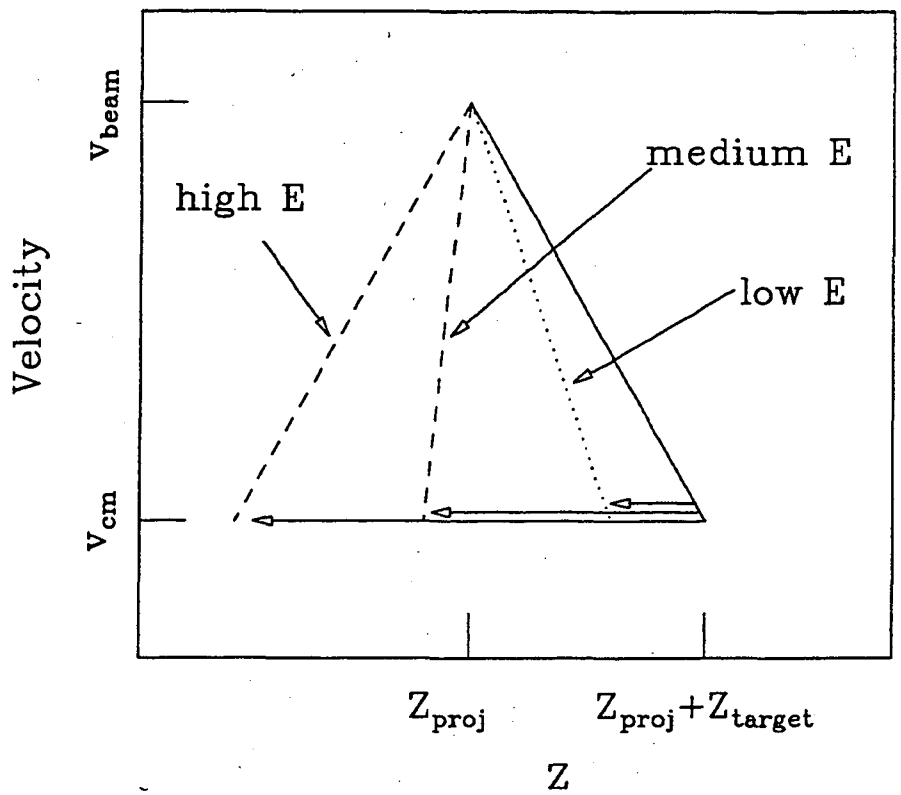

Figure 4.1: Schematic representation of the effect of light charged-particle evaporation on the correlation between the velocity and the Z of the incomplete fusion product. Z_{proj} is the Z value of the projectile. The solid line represents the locus of the velocities of the primary products from an incomplete fusion process. The short horizontal arrow to the dotted line shows the effect of evaporation on these products for low bombarding energies. The dashed lines show the loci of the velocities of the products after evaporation for higher bombarding energies.

contrast, large mass transfers result in primary fragments with lower velocities, higher excitation energies, and higher angular momenta. The higher excitation energy and angular momentum give a higher complex fragment emission probability and a lower probability of producing an evaporation residue.

In the present experiment, when the incomplete fusion product emits a complex fragment, the resulting decay products are rarely detected, as the recoiling nuclei are outside the spectrometer acceptance. Thus, the depletion of heavy residues at low velocities (i.e., near v_{cm}) in the ^{129}Xe+Al reactions results from high excitation energies in the primary fragments. The primary fragments' concomitant high probability of emitting a complex fragment results in their low probability of detection in the current experiment. In contrast, the high probability of emitting a complex fragment gives large mass transfer, low velocity events a higher detection probability in complex fragment experiments. This is why the complex fragment data in figure 3.18 are near v_{cm} for each reaction. Thus, the present Z value versus velocity distributions for the heavy residues fit nicely with the Z_{total} versus v_{source} distributions for the complex fragments (i.e. detecting the heavy residues is a good way to measure the cross section of small mass transfer events and detecting the complex fragments is a good way to measure the cross section of large mass transfer events). The combination of these data sets gives a complete picture of the reaction mechanism that can be understood within the framework of the incomplete fusion reaction mechanism. The qualitative agreement between the model and the data suggests that this reaction mechanism deserves further detailed investigation.

4.2 Model Calculations

In this section, the predictions from two models are discussed. These models are the incomplete fusion (ICF) model and the Boltzman–Nordheim–Vlasov (BNV) model. It has been shown that an incomplete fusion reaction mechanism qualitatively explains the data (see Section 4.1) and both the ICF and BNV models can produce incomplete fusion–like reactions (i.e. the larger nucleus picks up mass from the smaller nucleus). The BNV model is able to simulate pre-equilibrium emission of nucleons, whereas the ICF model can not. Pre-equilibrium emission can have significant effects at the bombarding energies used in the present work and thus the BNV model is a useful companion to the ICF model. Neither of these models is capable of calculating the de-excitation of the excited fragments. To remedy this problem, both models are coupled to a statistical decay model which simulates the de-excitation process.

Both models have been used previously to predict the data from similar reactions. The ICF model [bow89] has been successful in explaining many features of complex fragment emission from the 26 MeV/nucleon ^{129}Xe + C, Al, Ti, and Cu reactions [han93]. The BNV model has been successful in explaining certain aspects of the complex fragment data from the 55 MeV/nucleon ^{139}La + Al [col92a,col92b] and 50 MeV/nucleon ^{129}Xe + C, Al, V, Cu, Y, and Au reactions [bow92].

4.2.1 Incomplete Fusion Calculation

Predicting the final residue products from the incomplete fusion reaction involves two stages. The first stage is the incomplete fusion process. The second stage is the statistical decay of the excited fragments produced in the incomplete fusion process.

(For clarity during this discussion, "ICF model" refers only to the model of the first stage, whereas "ICF calculation" refers to the result of using the primary fragments from the ICF model as input to the statistical decay calculation.)

4.2.1.1 Incomplete Fusion Model

A simple ICF model has been constructed that incorporates kinematics into a geometrical picture of a nucleus–nucleus interaction [mor86,bow89][1]. A nucleus of mass A_1 and velocity v_{beam} collides with a target nucleus of mass A_2 at an impact parameter b. Let the occluded portions of A_1 and A_2 have masses m_1 and m_2, respectively. There are three possible scenarios for a collision (besides complete fusion, which appears naturally at low bombarding energies):

1. m_1 is sheared off and becomes attached to A_2.
2. m_2 is sheared off and becomes attached to A_1.
3. Both m_1 and m_2 are sheared off and remain separate from both A_1 and A_2.

Scenario 3 is the "fireball" process mentioned in Section 1.1 that has been suggested for bombarding energies greater than 100 MeV/nucleon [wes76,gos77]. This process has been studied [gai91] as the so called abrasion-ablation model [bow73,mor78,oli79]. This model is able to calculate the Z, A, excitation energy (E^*), and final spin (J) of each reaction partner. The E* is calculated in the limit that the shearing process happens fast enough that the orbits of the remaining nucleons are unaffected. In this limit, the removed nucleons leave holes in the distribution of filled quantum states of the residue nuclei. The nucleons change states to fill the holes. The energy difference between the

[1]This development of the ICF model follows a prescription by Bowman [bow89].

initially occupied state and the hole is given off during the transition and converted into thermal energy. The velocity of the reaction partners is calculated assuming a frictional force during the shearing process. Since this model uses assumptions which are valid only for reactions at higher bombarding energies than used in the present study, the abrasion-ablation model is not used in this work.

Scenarios 1 and 2 correspond to the incomplete fusion process. These processes are completely kinematical and can be studied without introducing dynamical assumptions, while scenario 3 requires dynamical information, such as restoring forces, to be included. Consider the case of scenario 2 where m_2 attaches itself to A_1 to make $A_1 + m_2$ and $A_2 - m_2$. (Similar equations can be derived in a identical way for scenario 1 where m_1 attaches to A_2. See [bow89].) Assume the force between $A_1 + m_2$ and $A_2 - m_2$ is Ks where s is the distance between $A_1 + m_2$ and $A_2 - m_2$ and K is some constant, then the velocities of the fragments are:

$$\mathbf{v}_{A_1+m_2} = \mathbf{v}_R - \frac{1}{A_1 + m_2} \int Ks \, dt \tag{4.1}$$

$$\mathbf{v}_{A_2-m_2} = \frac{1}{A_2 - m_2} \int Ks \, dt \tag{4.2}$$

where $\mathbf{v}_R$ is the initial velocity given to m_2 by A_1, $\mathbf{v}_R = \frac{A_1}{A_1+m_2}\mathbf{v}_{beam}$. Using $\mathbf{v}_S = \mathbf{v}_{A_1+m_2} - \mathbf{v}_{A_2-m_2}$, one obtains

$$\frac{d\mathbf{v}_S}{dt} = -\frac{1}{m^*} Ks \tag{4.3}$$

where $m^* = \frac{(A_1+m_2)(A_2-m_2)}{A_1+A_2}$. Integrating this equation yields

$$\mathbf{v}_{A_1+m_2} - \mathbf{v}_{A_2-m_2} = \mathbf{v}_R \sqrt{1 - \frac{Ks^2}{m^* \mathbf{v}_R^2}} \tag{4.4}$$

Using momentum conservation

$$A_1 \mathbf{v}_{beam} = (A_1 + m_2)\mathbf{v}_{A_1+m_2} + (A_2 - m_2)\mathbf{v}_{A_2-m_2} \tag{4.5}$$

gives

$$\mathrm{v}_{A_1+m_2} = \mathrm{v}_R\left[1 - \frac{A_2 - m_2}{A_1 + A_2}\left(1 - \sqrt{1 - \frac{2\Delta}{m^*\mathrm{v}_R^2}}\right)\right] \tag{4.6}$$

$$\mathrm{v}_{A_2-m_2} = \mathrm{v}_R\frac{A_1 + m_2}{A_1 + A_2}\left(1 - \sqrt{1 - \frac{2\Delta}{m^*\mathrm{v}_R^2}}\right) \tag{4.7}$$

where Δ is the separation energy of m_2 when fracture of A_2 occurs at maximum elongation s_{max}, $\Delta = \frac{1}{2}Ks_{max}^2$. The momentum of the fragments can now be calculated

$$\frac{P_{A_1+m_2}}{P_{beam}} = 1 - \frac{A_2 - m_2}{A_1 + A_2}\left(1 - \sqrt{1 - \frac{2\Delta}{m^*\mathrm{v}_R^2}}\right) \tag{4.8}$$

$$\frac{P_{A_2-m_2}}{P_{beam}} = \frac{A_2 - m_2}{A_1 + A_2}\left(1 - \sqrt{1 - \frac{2\Delta}{m^*\mathrm{v}_R^2}}\right) \tag{4.9}$$

Full mass transfer occurs when the square root in the above equations equals zero

$$1 - \frac{2\Delta}{m^*\mathrm{v}_R^2} = 0 \tag{4.10}$$

The bombarding energy where this occurs is

$$E = \frac{\Delta(A_1 + m_2)(A_1 + A_2)}{(A_2 - m_2)A_1^2} \tag{4.11}$$

where E is in MeV/nucleon. Complete fusion is predicted to occur below this energy, incomplete fusion is predicted above.

The separation energy Δ is taken to be the energy necessary to create the new nuclear surface. The surface area can be calculated from the geometry of the problem. A simple way to visualize this is to assume that the projectile travels in a straight line, thereby sweeping a cylindrical volume. The surface area created in the collision is the area of the cylinder wall contained within the sphere representing the target. Δ equals $2s_0S$ where S is the created surface area and s_0 is the surface energy constant from the liquid drop model of nuclear masses. The factor of two comes from the fact

that the surface area is created on both pieces of the broken nucleus. Which nucleus gets broken is determined by the amount energy needed to break either one of the nuclei. Less energy is needed the shear the occluded region from the smaller nucleus, since less surface area is created. Thus for $A_1 > A_2$, the smaller target nucleus is broken.

The amount of mass transferred can also be calculated from the geometry of problem. The occluded volume, V_O, is the volume contained by the intersection of the cylinder that is swept by the projectile and the sphere representing the target. All the nuclear matter within V_O is transferred.

The Z, A, and E^* for the fused product are calculated from the equations

$$A = A_1 + \frac{V_O}{V_2} A_2 \tag{4.12}$$

$$Z = Z_1 + \frac{V_O}{V_2} Z_2 \tag{4.13}$$

$$E^* \simeq E_A \frac{\frac{V_O}{V_2} A_2 A_1}{\frac{V_O}{V_2} A_2 + A_1} + s_0 S + Q \tag{4.14}$$

where E_A is the bombarding energy in MeV/nucleon, V_2 is the volume of A_2, Z_1 is the Z value of nucleus A_1, Z_2 is the Z value of nucleus A_2, and Q is the ground state mass difference of the entrance and exit channel fragments. The angular momentum of the fused product is calculated from the relative motions of the centers of mass of the projectile and of the mass transferred from the target. The Z and A of the target remnant are calculated from

$$A = \frac{V_2 - V_O}{V_2} A_2 \tag{4.15}$$

$$Z = \frac{V_2 - V_O}{V_2} Z_2 \tag{4.16}$$

The excitation energy of the target remnant is calculated from the difference in the surface energies of the nucleus in the sheared geometry and in the spherical shape after it relaxes. The angular momentum of the target is assumed to be 0 $\hbar$. The model assumes that the shearing process is fast enough not to induce any spin in the target remnant.

4.2.1.2 Statistical De-excitation Model

In the second stage of the calculation, the large excited primary fragment formed in the incomplete fusion process is assumed to de-excite statistically. The statistical decay of each fragment is simulated by using the Monte Carlo computer code GEMINI [cha88a],[2] in which all possible binary decays of the compound nucleus, from light particle emission to symmetric division, are considered. After each binary division, further decay of the resulting excited fragments is followed until all the available excitation energy is exhausted. Following the emission of a heavy fragment, the remaining excitation energy is divided under the assumption of equal temperatures in the two fragments. To calculate the spin of each fragment, the angular momentum is partitioned in the sticking limit. Thermal fluctuations in both the division of the excitation energy and the partition of angular momentum are incorporated.

The decay width for the evaporation of fragments with $Z \leq 2$ is calculated in GEMINI by using the Hauser-Feshbach formalism [hau52]. The emission of a light particle with nuclear charge Z_1 and mass A_1, of spin J_1, from a system (Z_0,A_0) of excitation energy E^* and spin J_0, leaving the residual system (Z_2,A_2) with spin J_2,

[2]This description of GEMINI is from [cha88a].

has a decay width given by the expression

$$\Gamma_{J_2}(Z_1, A_1, Z_2, A_2) = \frac{2J_1+1}{2\pi\rho_0} \sum_{l=|J_0-J_2|}^{J_0+J_2} \int_0^{E^*-B-E_{rot}(J_2)} T_l(\epsilon)\rho_2(U_2, J_2)d\epsilon \qquad (4.17)$$

In this equation, ϵ and l are the kinetic energy and the orbital angular momentum of the emitted particle, respectively; ρ_0 is the level density of the initial system; B is the binding energy; $E_{rot}(J_2)$ is the rotation plus deformation energy of the residual system; and $\rho(U_2,J_2)$ is the level density of the residual system with thermal excitation energy

$$U_2' = E^* - B - E_{rot}(J_2) - \epsilon \qquad (4.18)$$

The transmission coefficient, $T_l(\epsilon)$, is calculated in the sharp cut-off approximation for a classical system of absorptive radius R as follows:

$$T_l(\epsilon) \quad = 0 \text{ if } \epsilon < E_{coul} + \frac{\hbar^2 l(l+1)}{2\mu R^2} \qquad (4.19)$$

$$= 1 \text{ if } \epsilon \geq E_{coul} + \frac{\hbar^2 l(l+1)}{2\mu R^2} \qquad (4.20)$$

The Coulomb barriers (E_{coul}) are calculated by using the empirical expressions of Vaz and Alexander [vaz84], and the absorptive radius (R) is taken to be

$$R = 1.16 A_2^{\frac{1}{3}} + 2.6 \text{ fm} \qquad (4.21)$$

for proton and neutron emission and

$$R = 1.16 A_2^{\frac{1}{3}} + 3.7 \text{ fm} \qquad (4.22)$$

for alpha emission.

The decay width for the emission of heavy fragments ($Z \geq 3$) is calculated in GEMINI by using the transition state formalism of Moretto [mor75]. The decay width is

given by the equation

$$\Gamma(Z_1, A_1, Z_2, A_2) = \frac{1}{2\pi\rho_0}\int_0^{E^*-E_{sad}(J_0)} \rho_{sad}(U_{sad}, J_0)d\epsilon \tag{4.23}$$

Here ρ_{sad} is the level density of the conditional saddle-point configuration with the thermal energy (U_{sad}) given by

$$U_{sad} = E^* - E_{sad}(J_0) - \epsilon \tag{4.24}$$

$E_{sad}(J_0)$ is the deformation plus rotation energy of the saddle-point configuration, and ϵ is the kinetic energy of the translational degree of freedom.

For heavy fragments, the emission barriers used in these calculations were obtained from the Rotating Finite Range Model [kra79] by using a two–spheroid parameterization of the nuclear shape in the saddle-point configuration. These barriers were shown to be within 2 MeV of the saddle-point energies calculated from a more realistic shape parameterization [dav85] for A=110 [sie86]. To correct for this difference, the two-spheroid saddle-point energies were scaled by a constant factor for all mass asymmetries and angular momenta. The scaling factor was chosen so that the scaled saddle-point energy was equal to the value calculated with the more realistic shape parameterization by Sierk [sie86,dav85] for symmetric division.

The level density is given by the Fermi gas expression [bet36,boh69],

$$\rho(U, J) = (2J+1)(\frac{\hbar^2}{2I})^{\frac{3}{2}}\frac{a^{\frac{1}{2}}}{12}\frac{\exp[2(aU)^{\frac{1}{2}}]}{U^2} \tag{4.25}$$

where I is the moment of inertia, U is the thermal energy of the system, and a is the level density parameter. The level density parameter is related to the single-particle level density, g, by the expression $a = \frac{\pi^2 g}{6}$ and was taken to be equal to $\frac{A}{8.5}$ MeV^{-1}.

4.2.1.3 Incomplete Fusion Calculation Results

An ICF calculation was carried out for each reaction studied in the present work. All the parameters of the statistical decay model were set to standard values. The only adjustable parameter in the ICF model was the radius parameter (r_0), used to calculate the size of the sharp spheres.

$$R_{sharpsphere} = r_0 A^{\frac{1}{3}} \tag{4.26}$$

In this model, sharp-surfaced spheres were used to represent the nuclei. In reality, the nuclear surface is diffuse, so r_0 was assumed to be slightly adjustable.

It has been shown that the ICF calculations are sensitive to the value chosen for the radius parameter [han93]. Hanold et al. used r_0 as a fitting parameter in this ICF calculation to reproduce the complex fragment data from the 26 MeV/nucleon ^{129}Xe + C, Al, Ti, and Cu reactions. The best agreement with the cross sections and the Z_{total} versus v_{source} distributions was obtained with a value of r_0=1.10 fm. In the present study, changing the radius parameter had no effect on the predicted average mass for each element. (The predicted average mass for each element is determined by the statistical decay calculation. See Section 4.2.1.4.) The predicted elemental cross sections, however, were sensitive to r_0, as the cross section for production of the heavy residues increased 20% and the cross section in the $10 \leq Z \leq 30$ region increased 50% when r_0 was increased from 1.10 fm to 1.25 fm. The increased cross section results from the increased range of impact parameters that led to collisions. A greater fraction of collisions led to primary products with high excitation energy when r_0 was 1.25 fm. The high excitation energy gives a higher complex fragment emission probability and thus leads to the larger increase in the complex fragment

cross sections. A radius parameter of 1.10 fm was found to give the best agreement with the data from the previous study, and it also gave good agreement with the present data set.

The results from the ICF calculations can be compared to the cross section data in figures 3.14, 3.15, 3.16, 4.2, 3.8, 3.9, and 3.10 and the momentum distributions in Appendix A. (Figures 3.14, 3.15, and 3.16 show the elemental cross sections from the ICF calculation as dotted curves.) Possible systematic experimental errors make the absolute cross sections uncertain by up to a factor of four. (The error in the magnitude of the yields primarily results from a poor measurement of the integrated beam current.) The magnitude of the cross sections from the ICF calculation is somewhat variable, since r_0 was taken to be adjustable. Therefore, the shape of the predicted elemental cross sections is a more sensitive test of the calculation than the magnitude. For the heavy residues, the cross section distributions predicted by the ICF calculation generally have the same shape as the experimental cross section distributions, but the predicted cross sections are larger in magnitude. The ICF predictions for the ^{129}Xe + C data agree with the complex fragment data at 26 and 40 MeV/nucleon but overpredict the complex fragment yields at 50 MeV/nucleon. The ICF calculation for the ^{129}Xe + Al reaction only agrees with the complex fragment cross sections at 26 MeV/nucleon. The calculation for the 40 and 50 MeV/nucleon ^{129}Xe + Al reactions predicts complex fragment yields within an order of magnitude of the data, but the shape of the distribution is incorrect. Overall, the ICF calculation reproduces all the cross sections except for the complex fragment cross sections from the 40 and 50 MeV/nucleon ^{139}La + Al reactions.

The distributions of cross sections for fragments with $Z > 39$ as a function of

Z value and velocity are shown in the first, third, and fifth rows in Figure 4.2. The second, fourth, and sixth rows show the predictions of the incomplete fusion calculation. The upper horizontal line in each frame corresponds to the velocity of the beam. The lower horizontal line in each frame corresponds to the velocity of the center of mass for that reaction. Notice that the shape of the velocity distribution is closely predicted by the calculation. The ICF calculation also predicts the centroid value of the Z distribution correctly for all the targets and beam energies in this study. The width of the Z distribution for the 26 MeV/nucleon reactions is well reproduced, but the predicted width is too small by almost a factor of 2 for the 40 and 50 MeV/nucleon reactions.

The cross sections as a function of Z value and velocity are consistent with the incomplete fusion reaction mechanism, but the isotopically resolved momentum distributions provide a more detailed test of the model predictions. The momentum distribution for each isotope was extracted from the data, and the results are shown in Figures A.1 to A.9. The shape of the momentum distribution changes slowly with the mass of a given element; therefore, only the momentum distributions for a representative light, average, and heavy isotope of each element are presented. The experimental momentum distributions can be compared to the predictions from the ICF calculations. The calculated momentum distributions are shown as dashed curves on Figures A.1 to A.9. Note that the model predicts the very proton-rich isotopes to have less than 50 nanobarn production cross section in these reactions. This is why there are no predictions shown with the momentum distributions for the proton-rich isotopes. The shape and width of the calculation's distributions are close to the shape and width of the experimental distributions, but the predicted centroid values of the

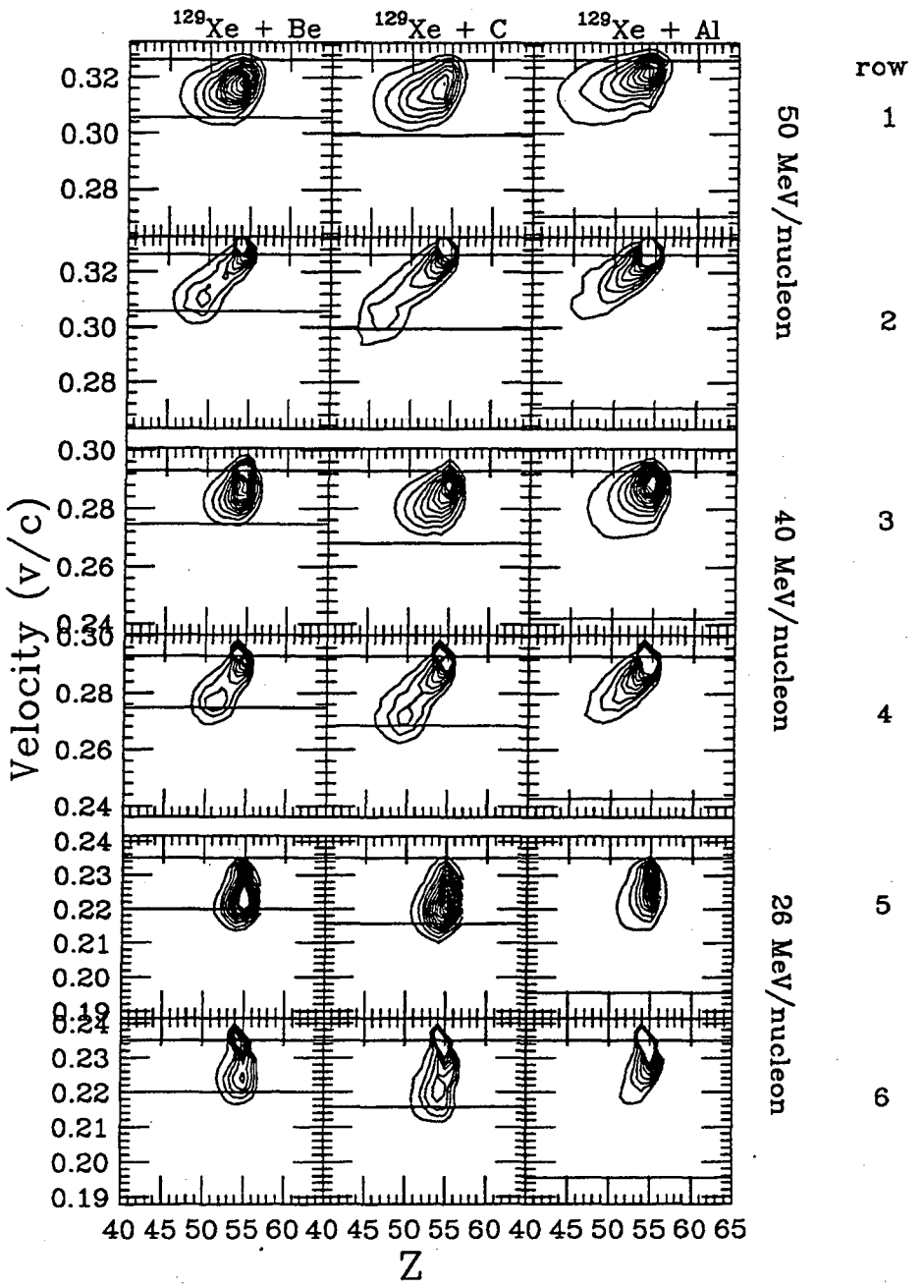

Figure 4.2: The distribution of cross section as a function of Z value and velocity are shown in the first, third, and fifth rows. The second, fourth, and sixth rows show the prediction of the incomplete fusion calculation. The upper horizontal line in each frame corresponds to the velocity of the beam. The lower horizontal line in each frame corresponds to the velocity of the center of mass for that reaction.

momentum distributions for the heavy isotopes are too large.

Figure 4.3 shows the isotopic cross section distributions from the ICF calculation and from the experimental data. (Figures 3.14, 3.15, and 3.16 show that the predicted elemental cross sections from the ICF calculation are too large. This implies that the total of the predicted isotopic cross sections for each element is also too high. The magnitude of the predicted isotopic cross sections shown in Figure 4.3 is scaled to match the maximum heights of the experimental cross section distributions. This was done to allow easy comparison of the centroid values and widths of the predicted and experimental distributions.) The predicted average isotope of a given element has, typically, two more neutrons than the experimentally determined average isotope of that element. (Alternatively, Figure 4.3 could be made to join all the isotopes of each isobar rather than all the isotopes of each element. It would then appear that the calculation's average atomic number for each isobar is one atomic number less than the experimental average atomic number for each isobar.) Furthermore, the predicted width of the mass distribution of each element is smaller than the corresponding experimental width. Figures 3.8, 3.9, and 3.10 show as contours the isotopic cross sections for each reaction studied here. The predicted average mass for each element is shown as a dashed line on these figures. The ridge in each isotopic cross section distribution is comparable to the dashed line. The overprediction of the average mass of each element by 2 amu is seen for each system. Possible solutions of this disagreement are discussed in section 4.2.1.4.

Overall, the ICF calculation gives an acceptable prediction of the results from this experiment. The shapes of the predicted elemental cross section distributions are correct for the heavy residues, and the predicted magnitudes of the cross sections are

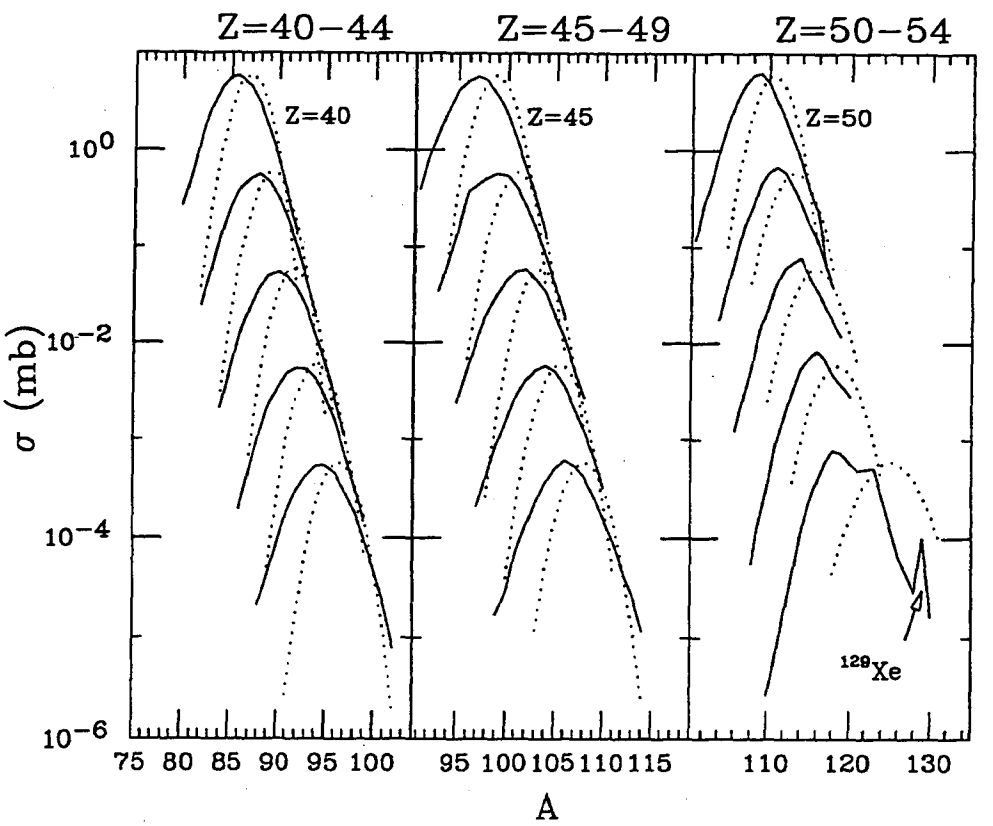

Figure 4.3: Experimental isotopic cross sections for the 50 MeV/nucleon ^{129}Xe + Al reaction are shown as solid curves. The predictions of the incomplete fusion calculation are shown as the dotted curves for the same reaction. The cross section for each element has been offset by an order of magnitude from its neighbors. The magnitude calculation has been scaled in this figure for easier comparison of the centroid values and the widths of the distributions with the data.

larger but are within the experimental uncertainty. The shapes of the cross section distributions as a function of Z value and velocity are closely predicted by the calculation. The calculation reproduces the shape and width of the momentum distribution for most isotopes well. The shapes of the calculated elemental cross sections for the complex fragments are correct for all the ^{129}Xe(^{139}La) + C reactions and for the 26 MeV/nucleon ^{129}Xe+Al reaction. The observed independence of the average mass for each element from the entrance channel (see Figure 3.11) is predicted by the ICF calculation. The average mass of each element, the width of the mass distribution of each element, and the width of the Z distribution as a function of velocity are not well reproduced, however. The causes of these differences are examined further in the next section.

4.2.1.4 GEMINI AND THE ISOTOPE PREDICTIONS

The overprediction of the experimental average mass of each element and the underprediction of the widths of the final fragment distributions are the significant failings of the ICF calculation. Since changing the radius parameter (r_0) of the ICF model had no effect on these predictions, the statistical decay calculation was examined to determine whether it was the cause of these differences.

The A/Z ratio of the final fragments resulting from statistical decay is decoupled from the A/Z ratio of the primary fragment for sufficiently high excitation energies. Charity et al. [cha88a] claimed that this decoupling occurs if the excitation energy is above 1 MeV/nucleon. In the present study, this excitation energy is easily reached for even small mass transfers. For the ICF model at 26 MeV/nucleon, this means transferring merely 4 nucleons, whereas at 50 MeV/nucleon, only 2 nucleons need be

transferred.

To demonstrate the decoupling of the initial and final A/Z ratios at high excitation energies, the average mass of each element was calculated for two different systems. One system was very proton rich (Z=67, A=149, E^*=580 MeV, and J_{max}=110$\hbar$), and the other system was very neutron rich (Z=67, A=166, E^*=580 MeV, and J_{max}=110$\hbar$). The calculation used a $2J+1$ weighting at each J and J ranged from $J = 0\ \hbar$ to J_{max}. For each element, the average residue masses from these two systems differ by less than one mass unit over most of the Z range. This is shown in Figure 4.4. A second, simpler statistical decay model that allowed only the emission of γ-rays and evaporation of neutrons, protons, and alpha particles was run to check GEMINI's predictions. The results from this code (LOTO [tas93]) are consistent with GEMINI's results. Thus, the step in the ICF + GEMINI calculation that determines the average mass for each element is the statistical decay calculation, since the A/Z ratio of the final fragments from GEMINI is decoupled from the A/Z ratio of the initial fragments input into GEMINI.

The isotopes predicted by GEMINI are less proton rich than the isotopes observed in the present work. Increasing the excitation energy of the initial fragments does not make the predicted final fragments more proton rich. Instead, increasing the excitation energy causes more evaporation, and the average residue mass decreases. This may indicate that the binding energy for the neutrons is too high relative to the emission barrier for protons in proton-rich nuclei. The neutron and proton binding energies are unknown for these nuclei, since the masses of many proton-rich nuclei seen in this work have not been measured. An extended liquid drop model [mol81] of the ground state nuclear mass is used by GEMINI to calculate the neutron and proton

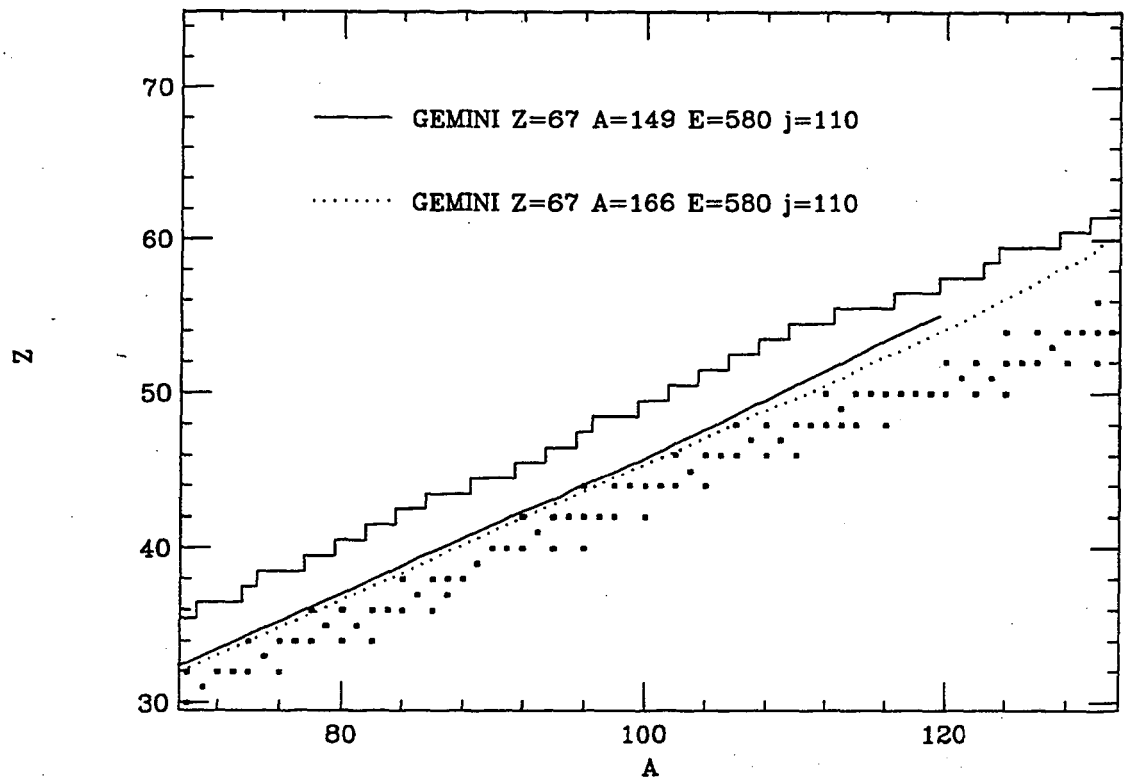

Figure 4.4: The average masses of each element predicted by GEMINI for two different initial nuclei are shown. One system is very proton-rich, Z=67 and A=149 and is shown as a solid line. The other system is very neutron-rich, Z=67 and A=166 and is shown as a dotted line. Shown as the stair-stepping line is the proton-rich limit of the known isotopes. Solid squares mark the positions of the stable isotopes.

binding energies for proton-rich nuclei. This mass model has a root-mean-squared error of 0.863 MeV for the ground state mass of the known nuclei. Small changes in the barriers for particle emission from the proton-rich nuclei may improve the agreement between the calculation and the data. For example, reducing the neutron binding energy of the proton-rich nuclei by 0.3 MeV reduces the average mass of each element by 1 amu. This change in the masses of the proton-rich nuclei is within the mass model's uncertainty, and thus the predicted average mass for each element can be brought into agreement with the experimental value.

In addition, there are other input parameters in the statistical decay calculation whose values are not well known. For example, the level density parameter (a) and the asymmetry parameter of the mass model are not well known. Small adjustments of these parameters may improve the agreement between the calculation and the data.

To investigate the effect of the level density parameter on the widths of the final fragment distributions, a was varied in the GEMINI calculations from $a = A/7$ to $a = A/10$. For $a = A/7$, the predicted average mass for each element decreased slightly ($< A_{a=\frac{A}{8.5}} > - < A_{a=\frac{A}{7}} >$=0.5) and the width of the isotopic cross section distribution decreased ($\sigma_{a=\frac{A}{7}}/\sigma_{a=\frac{A}{8.5}} = 0.75$) relative to the predictions using $a = A/8.5$. With $a = A/10$, the predicted average mass for each element increased slightly ($< A_{a=\frac{A}{8.5}} > - < A_{a=\frac{A}{10}} >$=–0.5) and the width increased ($\sigma_{a=\frac{A}{10}}/\sigma_{a=\frac{A}{8.5}} = 1.2$) relative to the predictions with $a = A/8.5$. When a decreased, the width of the distribution increased, but not enough to reproduce the data. Furthermore, the disagreement between the experimental and predicted average masses of each element became larger. These two opposite effects do not allow the simultaneous reproduction of both the average isotope for a given element and the width of the mass distribution for that element

by solely varying a.

Adjusting the binding energy for the neutrons changes the proton richness of the final fragments. Decreasing a and decreasing the neutron binding energy have opposing effects on the proton richness of the final fragments. The neutron binding energy and a were used together as fitting parameters to make the ICF predictions and the experimental values for the centroids and the widths of the final fragment distributions consistent. Agreement between the model predictions and the experimental data was achieved by reducing the neutron barrier by 2 MeV and setting a equal to $A/15$. This large a variation of these parameters is not physically justifiable.

The mass asymmetry parameter can change the neutron and proton binding energies so that they do not vary as strongly with the A/Z ratio of the decaying nucleus. The final fragment distribution can be made broader by changing this parameter. Unfortunately, this change also destroys the mass model's ability to reproduce the known nuclear masses. This implies that varying the mass asymmetry parameter is not a good solution to the disagreement between the model predictions and the experimental data.

There are a few other options for improving the agreement between the calculations and the data. The A/Z ratio of a nucleus with low excitation energy ($E^* \leq$ 30 MeV) is not changed very much by the de-excitation process. If the model of the collision stage produced a distribution of primary fragments that was similar to the experimental distribution, and these fragments had low excitation energies, then the subsequent de-excitation by GEMINI would not alter the primary distribution. The agreement between the prediction and the data would be improved. Excitation energies this low, however, are produced for only the extremely peripheral collisions

in the ICF model, and these collisions do not yield proton-rich primary fragments. This option is not available within the ICF model.

It was thought that the smaller predicted widths of the mass distribution for each element may result from the lack of fluctuations in the A/Z ratio of the transferred mass in the ICF model. Therefore, fluctuations in the A/Z ratio of the transferred mass were added to the ICF model. They had no effect on the final fragment distributions, however, since the final fragment A/Z ratio from GEMINI is decoupled from the initial fragment A/Z ratio.

It was thus found to be impossible to reproduce the final fragment distributions by using the ICF model coupled to GEMINI. This suggests that the most proton-rich fragments result from collisions that are not described within this model.

4.2.2 Boltzman–Nordheim–Vlasov Calculation

A second, somewhat different calculation was also compared to the data. The Boltzman–Nordheim–Vlasov (BNV) model represents the nucleons as an ensemble of test particles [bon90a,bon90b]. The test particle ensemble is used to make the calculated self-consistent mean field smooth. The BNV model follows the evolution of the test–particle density in phase space under the influence of a mean field and of collisions of the test particles. The BNV model allows for direct scattering and the resulting pre-equilibrium emission of nucleons. Prediction of the detectable products from the BNV model involves two stages that are similar to the stages in the ICF calculation. The first stage is the dynamic stage of the collision. The second stage is the statistical decay of the excited fragments produced in the first stage. (For clarity during this discussion, "BNV model" refers only to the BNV model of the first stage, while "BNV

calculation" refers to the result of coupling the BNV model to the statistical decay model.)

4.2.2.1 Boltzman–Nordheim–Vlasov Model

In the BNV model [bon90a,bon90b][3], the dynamic first stage of the collision was simulated by solving the BNV equation:

$$\frac{\delta f_1}{\delta t} + \frac{p_1}{m}\nabla_r f_1 - \nabla_r U \nabla_p f_1 = \int dp_2 dp_3 d\Omega \frac{|p_1 - p_2|}{m} \sigma_{NN}[f_3 f_4 (1-f_1)(1-f_2) - f_1 f_2 (1-f_3)(1-f_4)]\delta(p_1 + p_2 - p_3 - p_4) \quad (4.27)$$

where f is the one-body Wigner function, p is the momentum of a nucleon, and σ_{NN} is the nucleon–nucleon cross section with the energy and angular dependence included. The indices 1, 2, 3, and 4 are used to label the quantities associated with two nucleons before and after they collide (ie. 1+2⇒3+4). The mean field, U, includes the Coulomb interaction between protons plus a nuclear potential approximated by a density-dependent Skyrme-like interaction given by:

$$U_{nuc}(\rho) = A\left(\frac{\rho}{\rho_0}\right) + B\left(\frac{\rho}{\rho_0}\right)^{\sigma} + C\left(\frac{\rho_n - \rho_p}{\rho_0}\right)\tau_z \quad (4.28)$$

Here ρ,ρ_p, and ρ_n are the local nucleon, proton, and neutron densities, respectively, and τ_z is the isospin operator with eigenvalues of +1 and −1 for neutrons and protons, respectively [tsa85]. The parameters A, B, C, and σ are chosen to reproduce nuclear matter saturation properties and a compressibility coefficient of K=200 MeV.

The BNV equation is solved using the test particle approach in a "full ensemble" method [ber84,ber88]. In this method, the one-body Wigner function of a system (composed of A_p projectile and A_t target nucleons) is described as an ensemble of

[3]This description of the BNV model follows a outline by Bertsch [ber88].

$N_g(A_p+A_t)$ test particles that collide with a cross section of σ_{NN}/N_g, where N_g is the number of test particles per nucleon. To ensure a reasonable mapping of the phase space and to avoid difficulties from numerical fluctuations, each nucleon is represented by $N_g = 50$ test particles. The Wigner function (f) is approximated by

$$f(r,p,t) = (2\pi\hbar)^2 \sum_{i=1}^{N_g(A_p+A_t)} \delta(r-r_i)\delta(p-p_i) \tag{4.29}$$

where δ is the Dirac delta function. In the test particle approach, f is a solution of the BNV equation, provided the position (r_i) and momentum (p_i) are solutions to the equations of the motion for the test particles. The test particles propagate according to Hamiltonian dynamics under the influence of an acceleration term generated by the gradient of the self-consistent mean field potential.

The test particles are initially assigned random positions in a sharp sphere. Momentum is also assigned randomly to the test particles within a local sphere in momentum space of radius p_f.

$$p_f = (3\pi^2\rho)^{\frac{1}{3}}\hbar \tag{4.30}$$

where ρ is the local density. Finally, the test particles in the target and projectile are boosted toward each other, their center-of-mass momenta being determined by the incident energy and the projectile and target masses.

The collision is followed as a function of time until the slope of the mean kinetic energy of the emitted nucleons versus time curve has changed. This sudden change of the slope is taken to indicate the transition from pre-equilibrium emission to evaporation from an equilibrated source. The sudden change in slope is visible in Figure 4.5. At the relaxation time (about 110 fm/c), where the slope of the emitted nucleons' mean energy versus time curve changes, a clustering procedure is used to calculate

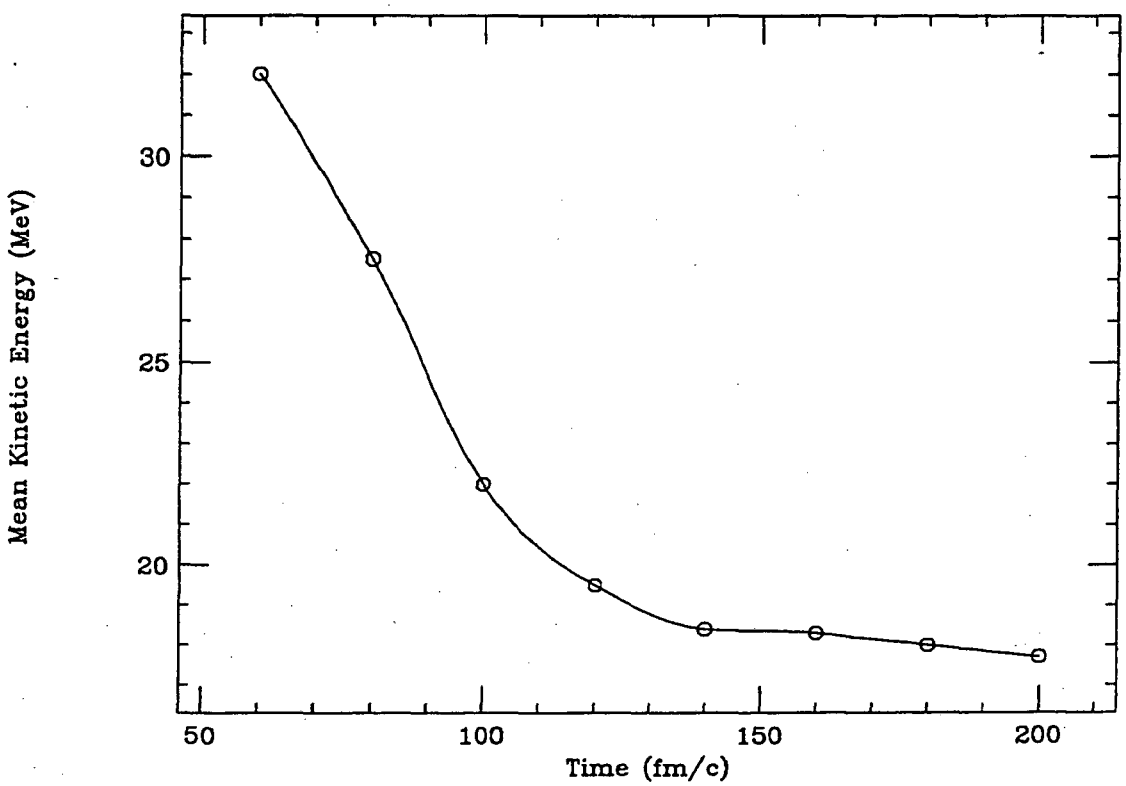

Figure 4.5: Calculated mean energy of the emitted nucleons as a function of time with the BNV model for the 50 MeV/nucleon ^{129}Xe + Al reaction at b = 3 fm.

the Z, A, E^*, and J of each fragment. This procedure forms clusters from the test particles that satisfy the condition $\mid r_i - r_j \mid < D$, where r_i and r_j are the positions of the i-th and j-th test particles. D is set to the minimum value that allows the clustering procedure to reproduce the target and projectile masses at the start of the calculation (D = 1.5 fm). The angular momentum of the cluster is determined by summing the angular momentum of each particle:

$$J = \Sigma \, \mathrm{r}_i \times \mathrm{p}_i \tag{4.31}$$

in the cluster center of mass. The cluster excitation energy is

$$E^* = E_{kin} + E_{nmf} + E_{coul} - E_{gs} \tag{4.32}$$

where E_{kin} is the total kinetic energy, E_{nmf} is the nuclear mean field energy, E_{coul} is the Coulomb energy, and E_{gs} is the ground state total energy calculated from the static solution used as the initial condition for the BNV calculation. The Z, A, E^*, and J of the excited primary fragments at the relaxation time are then used as input values for a statistical decay code (in this case, GEMINI) to simulate the de-excitation process. This calculation is carried out for the entire range of impact parameters. The results for all the impact parameters are combined to give a prediction of the entire reaction.

In practice, the clustering procedure sometimes gave incorrect results at the relaxation time, because the primary fragments were not well separated. Fragments that were only slightly separated were frequently clustered together. To overcome this problem, the BNV calculation was extended to longer times (130 fm/c) where the clusters were clearly defined. The clusters' Z, A, E^*, and J were determined as a function of time. The functions for Z, A, E^*, and J were extrapolated back to

the relaxation time to obtain the Z, A, E^*, and J of the separated fragments at the relaxation time.

The BNV model allows some Pauli-blocked nucleon–nucleon collisions to occur. This results from the model's not including the nucleon quantum states exactly. Instead, the model uses an approximate Pauli-blocking calculation. The number of spurious collisions decreases with increasing test particle number. The number of spurious collisions increases with increasing time. It also increases with decreasing bombarding energy because of the larger overlap of the nuclei's Fermi spheres at low bombarding energy and the resulting stronger Pauli blocking. Violation of the Pauli blocking frees some energy that is released in the form of evaporation. As a demonstration of this problem, a BNV calculation for a nucleus in its ground state (i.e., without reaction) predicts that the nucleus loses mass and attains a negative excitation energy. In other words, a stable nucleus decays (which is impossible). The problem with this example is that it contains only nucleon–nucleon collisions within one nucleus, and the error is larger in the case of a collision between two nuclei. Another example of this problem is found in the 50 MeV/nucleon ^{129}Xe + Al collision at an impact parameter of 6 fm. The calculated excitation energy of the projectile-like fragment becomes negative approximately 200 fm/c after the start of the collision. This is an impossible result. To minimize the Pauli-blocking violation, this model should be used only for short time scales (less than 150 fm/c).

An error has recently been reported to exist in an earlier version of the BNV code [col93]. It allowed double counting of the nucleon–nucleon collisions. This problem was removed from the present code. Using the earlier version of the BNV code, Colonna et al. [col92a] found that the calculation for the 55 MeV/nucleon ^{139}La + Al reaction

at an impact parameter of 3 fm showed a fast fission-like reaction. With the corrected BNV code, the fast fission was not seen.

4.2.2.2 Boltzman–Nordheim–Vlasov Calculation Results

The BNV model produces one primary fragment for central collisions at 26 to 50 MeV/nucleon. The BNV model produces two primary fragments for very peripheral collisions at 40 and 50 MeV/nucleon. Figure 4.6 shows a comparison of the calculated values for the mass, excitation energy, and velocity of the primary projectile-like fragments from both the BNV and the ICF models for the 50 MeV/nucleon ^{129}Xe + Al reaction. The crosses with the error bars represent the results and the uncertainties from the BNV model at each impact parameter. The uncertainty in the BNV result arises primarily from determining the relaxation time. The error bars represent variation of the relaxation time by ± 5 fm/c. The BNV model predicts smaller masses and excitation energies than the ICF model because pre-equilibrium emission is allowed in the former and not in the latter. The shapes of the velocity, mass, and excitation energy distributions for the primary projectile-like fragments, however, are very similar for both models (see Figure 4.6). This similarity is seen for all the 40 and 50 MeV/nucleon ^{129}Xe + Be, C, and Al reactions.

The BNV model predicted the formation of very elongated, rotating objects at 26 MeV/nucleon and large impact parameters. (See Figure 4.7.) Even at times greater than 300 fm/c, the shape did not relax. Since the shape of the primary fragment had not relaxed by this time, the model result was not consistent with the assumption of equilibration within the model's usable time scale. In addition, the excitation energies for all impact parameters at 26 MeV/nucleon became negative between 160 fm/c and

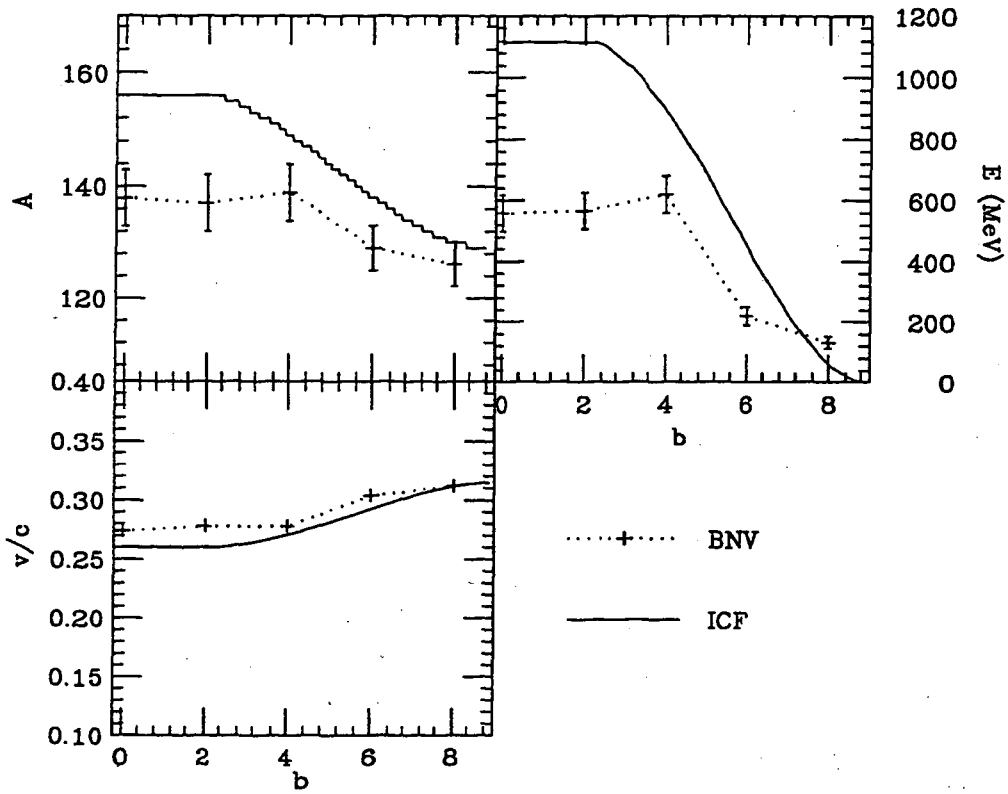

Figure 4.6: The mass, excitation energy, and velocity of the primary projectile-like fragment as a function of impact parameter from both the BNV (dotted) and ICF (solid curve) models for the reaction of 50 MeV/nucleon ^{129}Xe + Al. The crosses with error bars are the results and uncertainties from the BNV calculation at each impact parameter.

220 fm/c after the start of the collision because of violation of the Pauli principle in the BNV model. The slope of the emitted nucleons' mean kinetic energy curve did not change until 120 fm/c to 130 fm/c. This required that the BNV model be run for longer times than it was for the 40 and 50 MeV/nucleon reactions. The longer time requirement, combined with the lower bombarding energy and increased overlap of the Fermi spheres, means that the Pauli-blocking violation is large. Therefore, the BNV calculations were not run for the 26 MeV/nucleon reactions.

Overall, the BNV model produced an incomplete fusion-like reaction (i.e. the projectile nucleus picked up mass from the smaller target nucleus). The excited primary fragments from the BNV model were coupled to a statistical decay model to determine the final fragments. The results of these coupled model calculations are shown in Figure 4.8 for the 50 MeV/nucleon ^{129}Xe + Al reaction. Also shown in Figure 4.8 are the predictions from the ICF calculation and the experimental data. The predicted Z value versus velocity distributions and elemental cross sections from the BNV + GEMINI calculations are very similar to those from the ICF + GEMINI calculations. Both models give similar results for the average mass for each element, the width of the mass distribution for each element, and the momentum distributions for each isotope for all the 40 and 50 MeV/nucleon reactions studied. Since GEMINI was used to calculate the de-excitation stage, the BNV + GEMINI calculations also overestimate the average mass for each element and underestimate both the width of the Z distribution as a function of velocity and the width of the isotope distribution for each element. The cause of and solutions to these differences are discussed in detail in section 4.2.1.4.

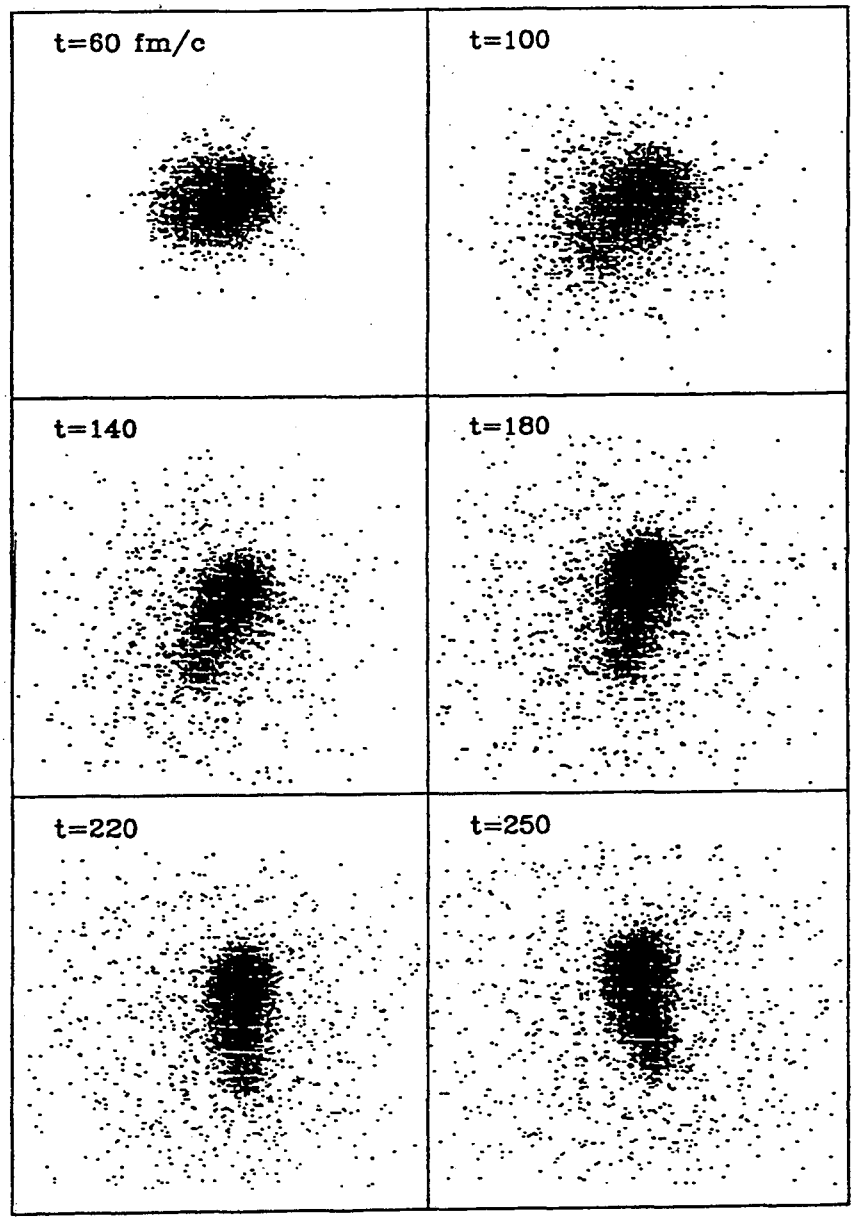

Figure 4.7: Density distributions from the BNV calculations for the system of 26 MeV/nucleon ^{129}Xe+Al at an impact parameter of b = 5 fm. The beam direction is vertical.

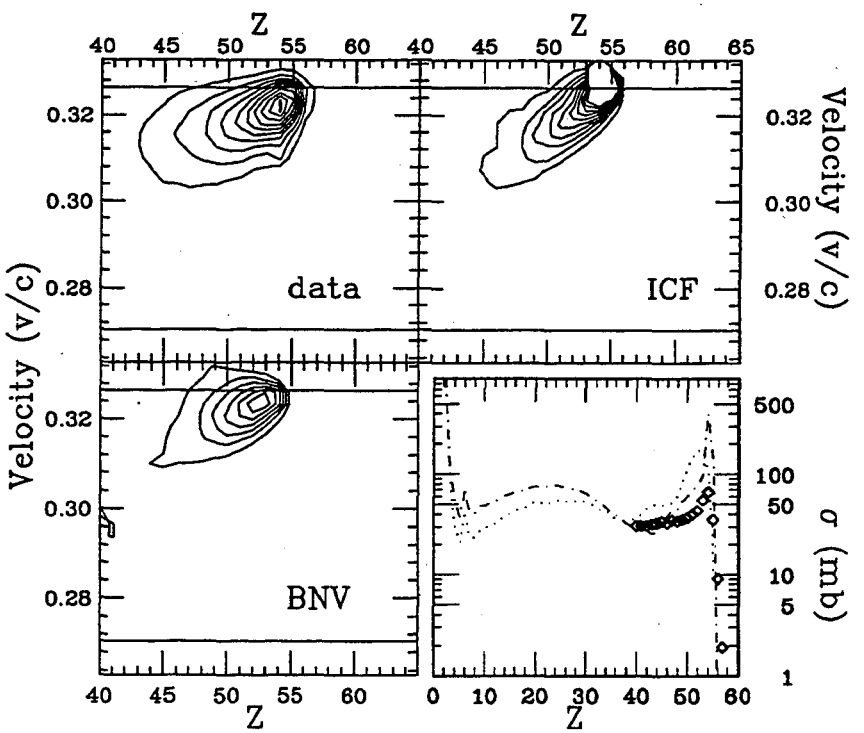

Figure 4.8: The upper left frame shows the cross sections in the Z versus velocity plane from the 50 MeV/nucleon ^{129}Xe + Al reaction. The upper horizontal line corresponds to the velocity of the beam. The lower horizontal line corresponds to the velocity of the center of mass. The upper right frame shows the same distribution predicted by the ICF calculation. The lower left frame shows the distribution predicted by the BNV calculation. The contour lines are linearly spaced. The lower right frame shows the elemental cross sections. The heavy residue cross sections from the current work are shown as diamonds; the ICF predictions, as a dashed line; and the BNV predictions, as a dotted line.

4.3 CONCLUSION

In general, the differences between the ICF and BNV predictions are fairly small; however, there is one significant difference between the predictions of the BNV and ICF models. The ICF model predicts the production of a target remnant over a large range of impact parameters, whereas the BNV model predicts the production of a target remnant for only very peripheral reactions. For more central collisions ($b = 4$ fm), where the ICF model predicts a target remnant, the BNV model predicts that the mass not in the primary fragment is left in a few very small fragments ($Z \leq 2$) and many single nucleons. The present experiment is capable of detecting neither the target-like remnant nor a large number of single nucleons and thus can not distinguish between the ICF and the BNV model predictions.

The answers to the first two questions that were posed at the beginning of this chapter are now clear. The first two questions were:

1. Do the heavy residues come from the same source as the complex fragments, or do they result from a different type of reaction?

2. Can the models that successfully predicted the complex fragment production also predict the heavy residue data?

It has been shown that heavy residues are produced in complete and incomplete fusion reactions. Models of these reaction mechanisms have predicted the complex fragment data well. These models also predict many aspects (e.g., the elemental cross sections, the cross sections as a function of Z value and velocity, and isotopically resolved momentum distributions) of the heavy residue data reasonably well. The exception

to this is that both models predict less than 50 nanobarn production cross section for the very proton-rich nuclei observed in this experiment. This point leads to the third question that was posed at the beginning of the chapter:

3. What is the source of the extremely proton-rich nuclei seen recently at slightly higher beam energies?

These models are able to reproduce the proton-rich nuclei only if currently accepted input parameters of the statistical decay calculation are strongly varied; however, these large variations are not physically justifiable. This suggests that the source of these extremely proton-rich nuclei must be a reaction that produces cold proton-rich nuclei. The details of this reaction mechanism are not understood within either model examined here.

Chapter 5

Conclusions

The production cross sections of the residues with $Z > 39$, as a function of Z, A, and momentum, from the 26, 40, and 50 MeV/nucleon ^{129}Xe + Be, C, and Al reactions were measured by using a magnetic spectrometer. Including the present data and previous data, experimental cross sections spanning almost the entire range of Z values produced in these reactions have now been measured. The current data have been compared to those from previous works utilizing similar reactions. Although the elemental cross sections do not overlap previous measurements, they seem to be consistent with them. The isobaric cross sections generally agree with previous γ-ray spectroscopy measurements of the isobaric cross sections for similar systems.

Measurements of the isotopic cross sections by γ-ray spectroscopy have had to assume a smoothly varying cross section distribution to extract the cross sections for the undetectable isotopes. The need for this premise results from the inability of γ-ray spectroscopy to detect short-lived isotopes ($t_{1/2} < 5$ minutes). The symmetry of the experimental isotopic cross sections (Figure 3.4) for each element and the smooth variation between elements confirm the validity this assumption.

The experimental Z value versus velocity distributions are consistent with the

Z_{total} versus v_{source} distributions determined from complex fragment coincidence data. This study provides a determination of the relative amounts of incomplete and complete fusion that is complementary to that implied in studies of complex fragments. Events with very low excitation energies are easily detected in the present work, since no fission-like decay is required. These distributions provide strong evidence for an incomplete fusion reaction mechanism.

5.1 Reaction Mechanism

Many features of the current data were reproduced by an incomplete fusion (ICF) model coupled to a statistical decay calculation. This calculation was able to reproduce the shapes of the heavy residue elemental cross sections and the Z value versus velocity distributions. The complex fragment emission velocities and cross sections from the 40 and 50 MeV/nucleon La + C reactions and the 26 MeV/nucleon Xe + C and Al reactions were well reproduced. The ICF calculation also predicted the independence from the entrance channel of the average mass for each element. The primary failures of this model are its overestimation of the average mass for each element and its underestimation of the widths of the Z distributions as a function of velocity and of the isotope distribution for each element. The momentum distributions provide a new test of the reaction model. The most proton-rich nuclei are predicted to have less than 50 nanobarn production cross section and thus have no predicted momentum distribution. The average mass isotope for each element typically has its momentum distribution well predicted by the model calculation. The heavier isotopes of each element are not as well predicted, as the predicted centroid values are too large.

The difference between the experimental and predicted average isotopes for each element can be eliminated by small, but systematic, variation of the input parameters for the statistical decay calculation. The width of the Z distribution as a function of velocity and the width of the isotope distribution for each element can not be reproduced with reasonable input parameters for the calculation. Overall, the incomplete fusion model coupled to a statistical decay model gives a good representation of the data.

A Boltzman–Nordheim–Vlasov (BNV) model coupled to a statistical decay model yields essentially the same prediction as the ICF model for the heavy residue data from the 40 and 50 MeV/nucleon ^{129}Xe + Be, C, and Al reactions. Both models predict that the heavy residues produced in this energy region result from incomplete fusion-like reactions (i.e. the projectile nucleus picked up mass from the smaller target nucleus). There is one significant difference between the predictions of the BNV and ICF models. The ICF model predicts the production of a target remnant over a large range of impact parameters, whereas the BNV model predicts the production of a target remnant for only very peripheral reactions. For more central collisions ($b = 4$ fm), where the ICF model predicts a target remnant, the BNV model predicts that the mass not in the primary fragment is left in a few very small fragments ($Z \leq 2$) and many single nucleons. The present experiment is capable of detecting neither the target-like remnant nor a large number of single nucleons and thus can not distinguish between the ICF and the BNV model predictions.

The very proton-rich nuclei detected in the present study are predicted to have less than 50 nanobarn production cross section by both models. The production mechanism for these very proton-rich nuclei, as well as the mechanism producing the

extremely proton-rich nuclei observed recently, is not understood within the reaction mechanisms studied here. The models can predict the production of these proton-rich nuclei only if the statistical model input parameters are varied beyond the physically possible range. Therefore, these nuclei must be produced in a collision that makes the nuclei with almost no excitation energy. Any moderate amount of excitation energy would enable the nucleus to evaporate a proton and become less proton rich.

5.2 Speculation on Future Work

An experiment capable of detecting the low-velocity target remnant or the total particle multiplicity in coincidence with the heavy residue would be able to distinguish between the predictions of the incomplete fusion model and the Boltzman–Nordheim–Vlasov model. A novel approach to detecting the target remnant would be to use colliding beams. With this technique, both the "target" and projectile remnants would have large laboratory velocities and would be easily detected. Unfortunately, no such colliding beam facility exists. It would be easier to detect the light fragments in coincidence with a heavy residue. This could be done by using a large solid-angle detector placed around the target to detect the light particles and a magnetic spectrometer to detect the heavy residues. The Z_{total} of the light charged particles could be constructed and compared to that in the ICF and BNV model predictions.

The isotopes detected from these reactions are very proton rich. The isotopic cross section distribution compared fairly well with the limited distributions measured by Yennello et al. [yen92]. A similar experiment with a more proton-rich beam, such as ^{124}Xe instead of ^{129}Xe, and running at slightly higher energy may have a good chance at locating several new proton-rich isotopes near the proton drip-line in the $Z = 50$

region.

Measurements of the ground-state masses of the proton-rich nuclei would be valuable. Along with providing a check of the mass model predictions, these masses would give better values for the proton and neutron binding energies used in the statistical model as input parameters. Improved knowledge of the input parameters would allow accurate determination of which isotopes can be produced in statistical decay of excited nuclei. This would allow the accurate determination of which isotopes are produced from nonstatistical processes and the examination of the reactions that produce the very proton-rich nuclei.

Appendix A

Momentum distributions

The momentum distributions for representative light, medium, and heavy isotopes of all elements with $Z > 39$ from the 50, 40, and 26 MeV/nucleon ^{129}Xe + Be, C, and Al reactions are shown in the following nine figures.

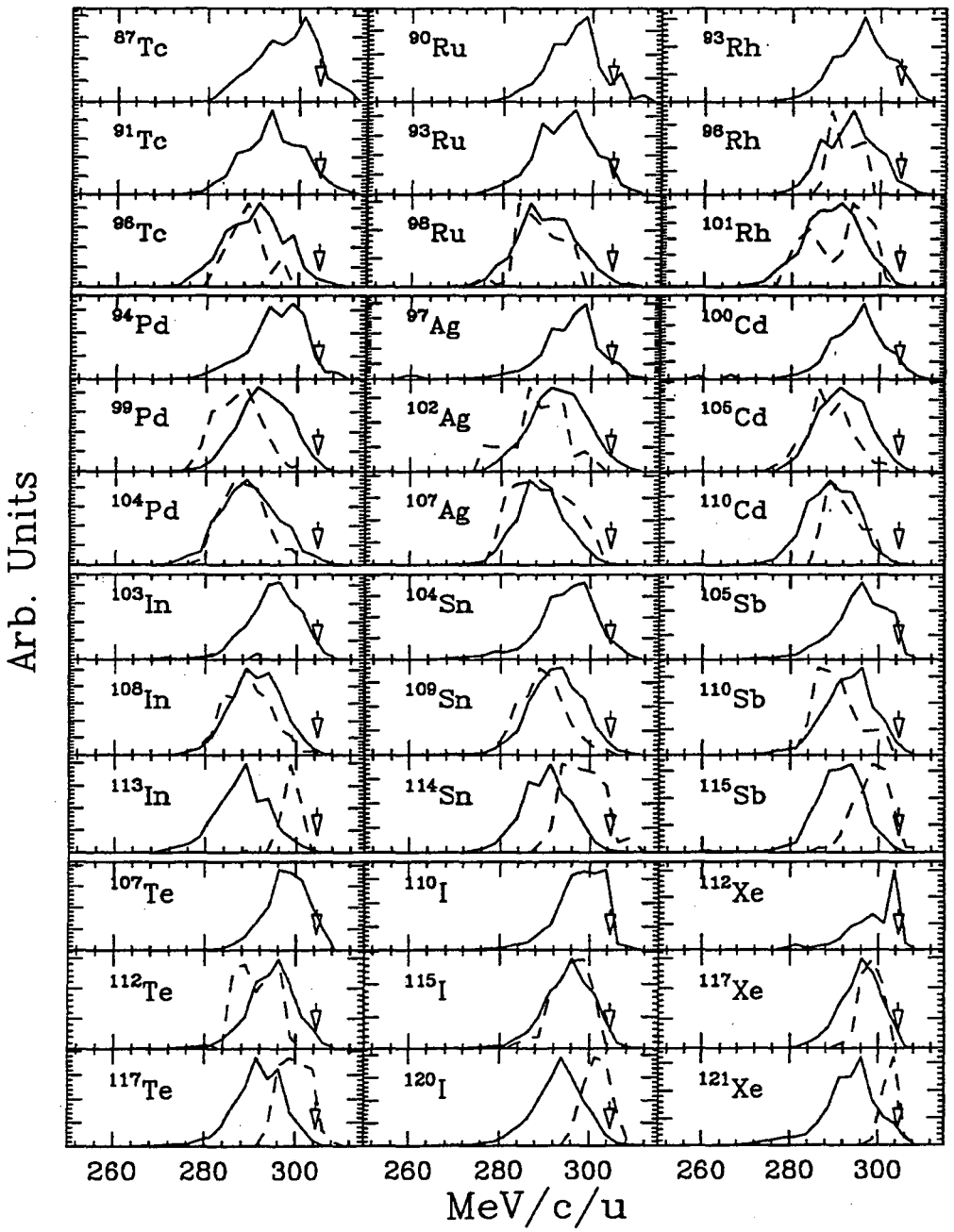

Figure A.1: The continuous curves are momentum distributions for representative light, medium, and heavy isotopes of all elements from the 50 MeV/nucleon ^{129}Xe+Be reaction. The dashed curves are the results of a model calculation (see Chapter 4). The arrow is at the momentum of the beam in each frame. The momentum of the center of mass for this system is 284.8 MeV/c/u.

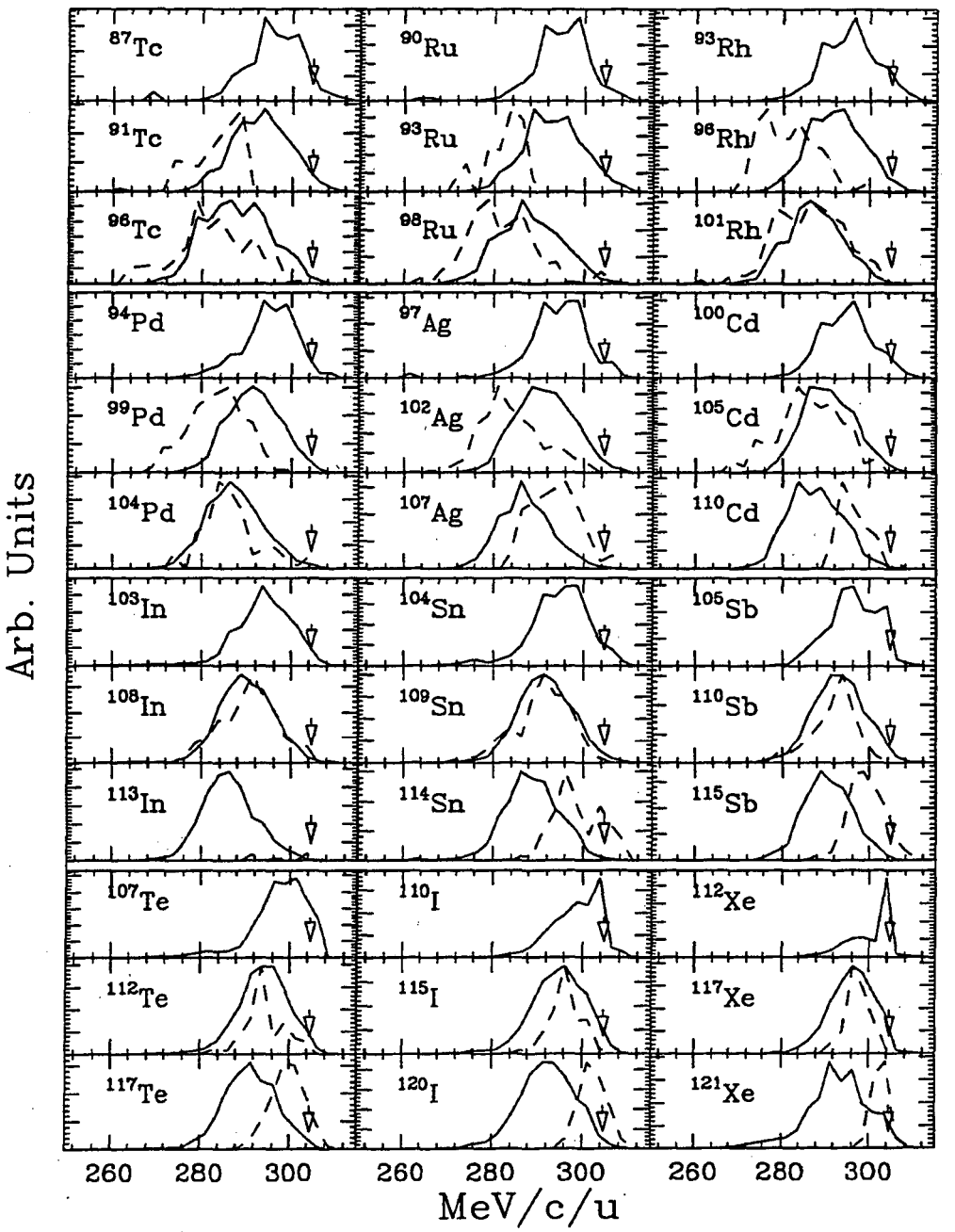

Figure A.2: The continuous curves are momentum distributions for representative light, medium, and heavy isotopes of all elements from the 50 MeV/nucleon ^{129}Xe+C reaction. The dashed curves are the results of a model calculation (see Chapter 4). The arrow is at the momentum of the beam in each frame. The momentum of the center of mass for this system is 278.7 MeV/c/u.

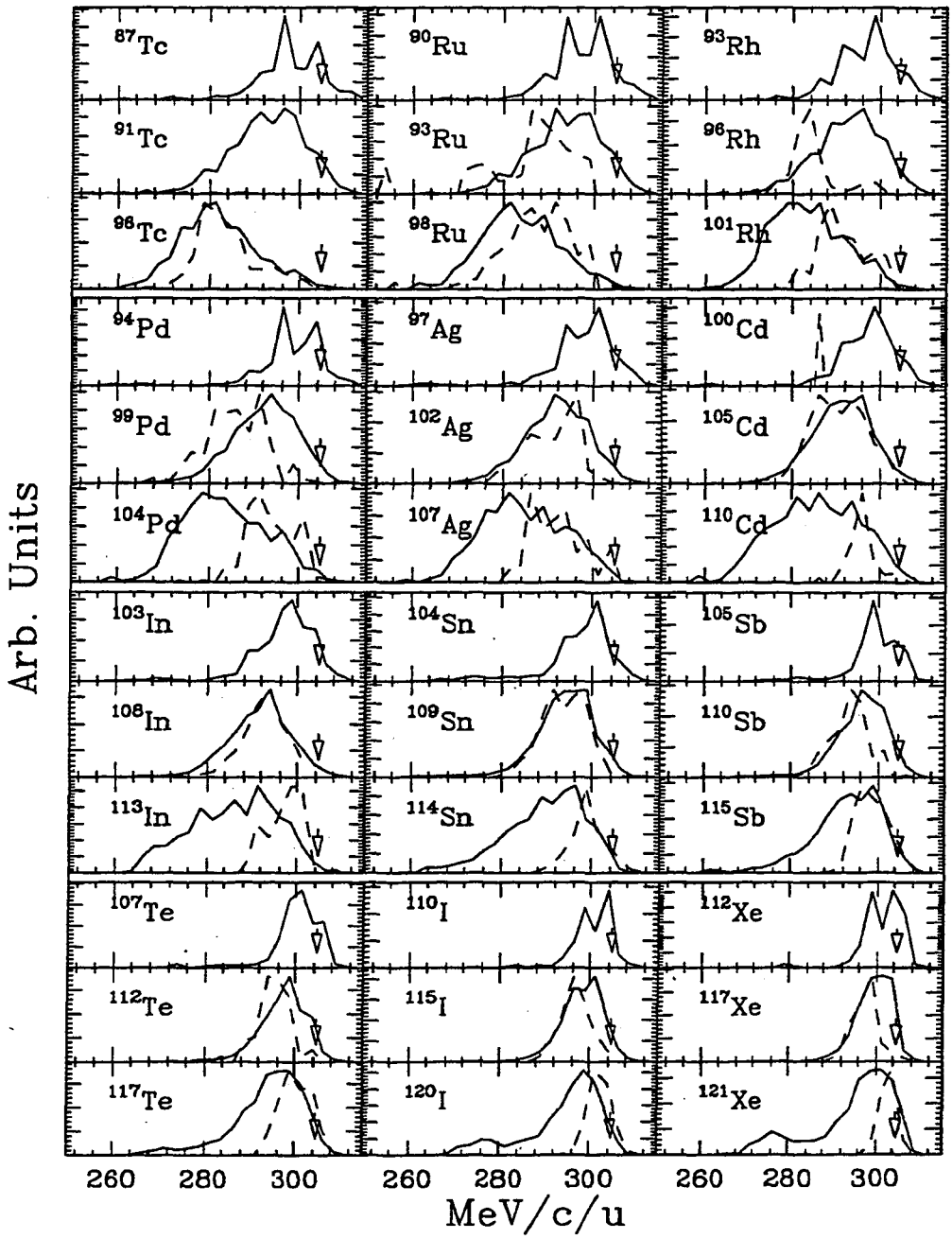

Figure A.3: The continuous curves are momentum distributions for representative light, medium, and heavy isotopes of all elements from the 50 MeV/nucleon ^{129}Xe+Al reaction. The dashed curves are the results of a model calculation (see Chapter 4). The arrow is at the momentum of the beam in each frame. The momentum of the center of mass for this system is 251.9 MeV/c/u.

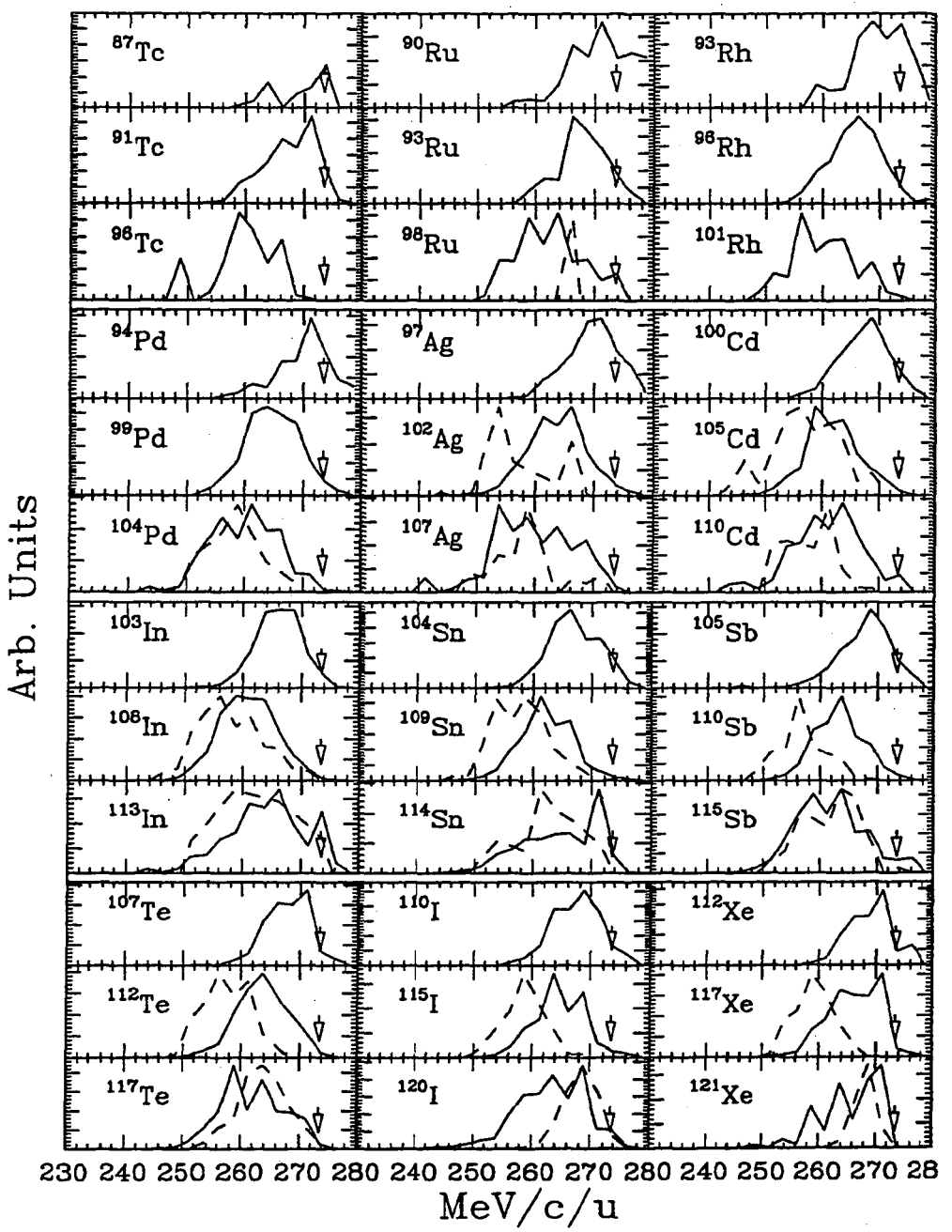

Figure A.4: The continuous curves are momentum distributions for representative light, medium, and heavy isotopes of all elements from the 40 MeV/nucleon ^{129}Xe+Be reaction. The dashed curves are the results of a model calculation (see Chapter 4). The arrow is at the momentum of the beam in each frame. The momentum of the center of mass for this system is 255.7 MeV/c/u.

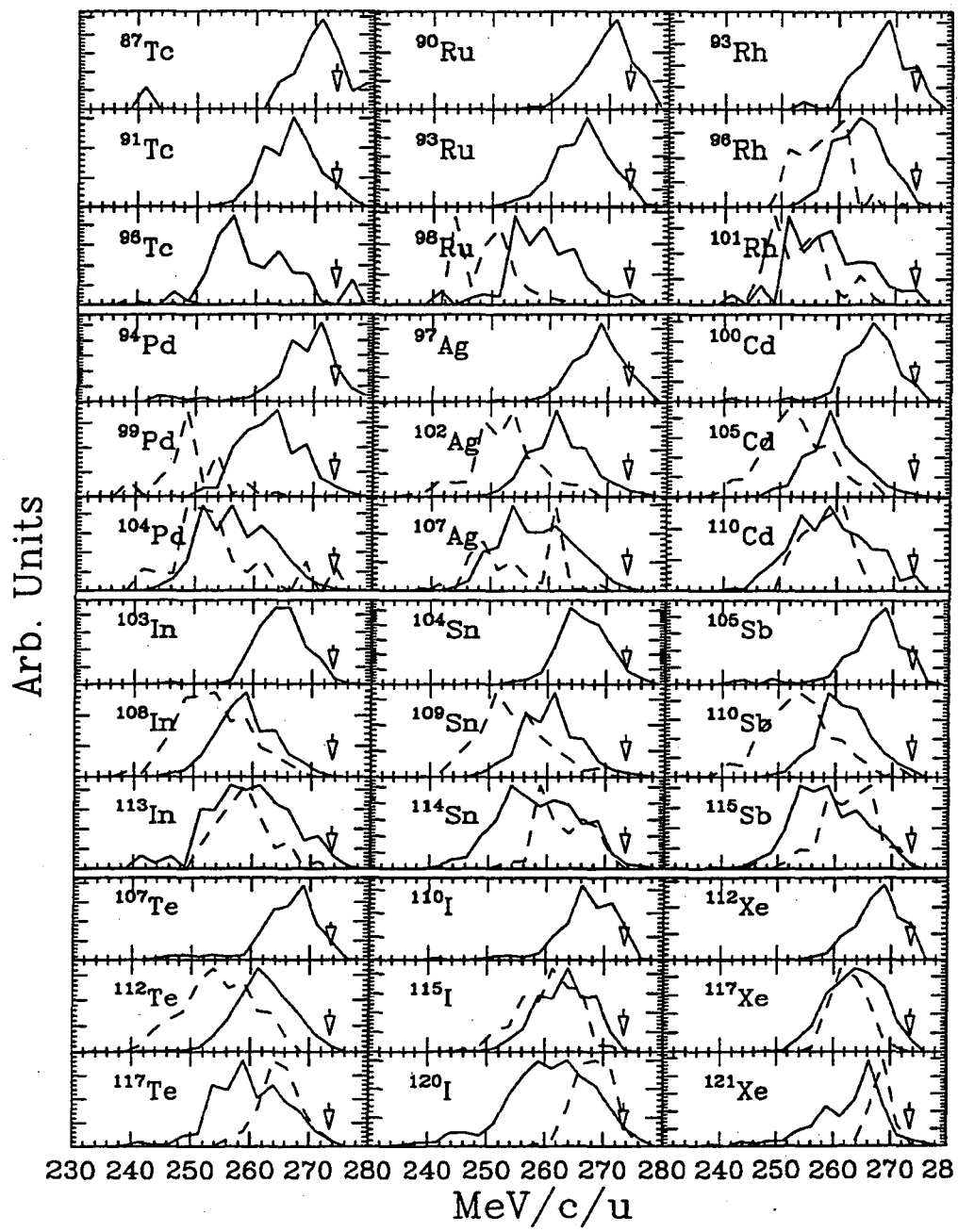

Figure A.5: The continuous curves are momentum distributions for representative light, medium, and heavy isotopes of all elements from the 40 MeV/nucleon ^{129}Xe+C reaction. The dashed curves are the results of a model calculation (see Chapter 4). The arrow is at the momentum of the beam in each frame. The momentum of the center of mass for this system is 250.3 MeV/c/u.

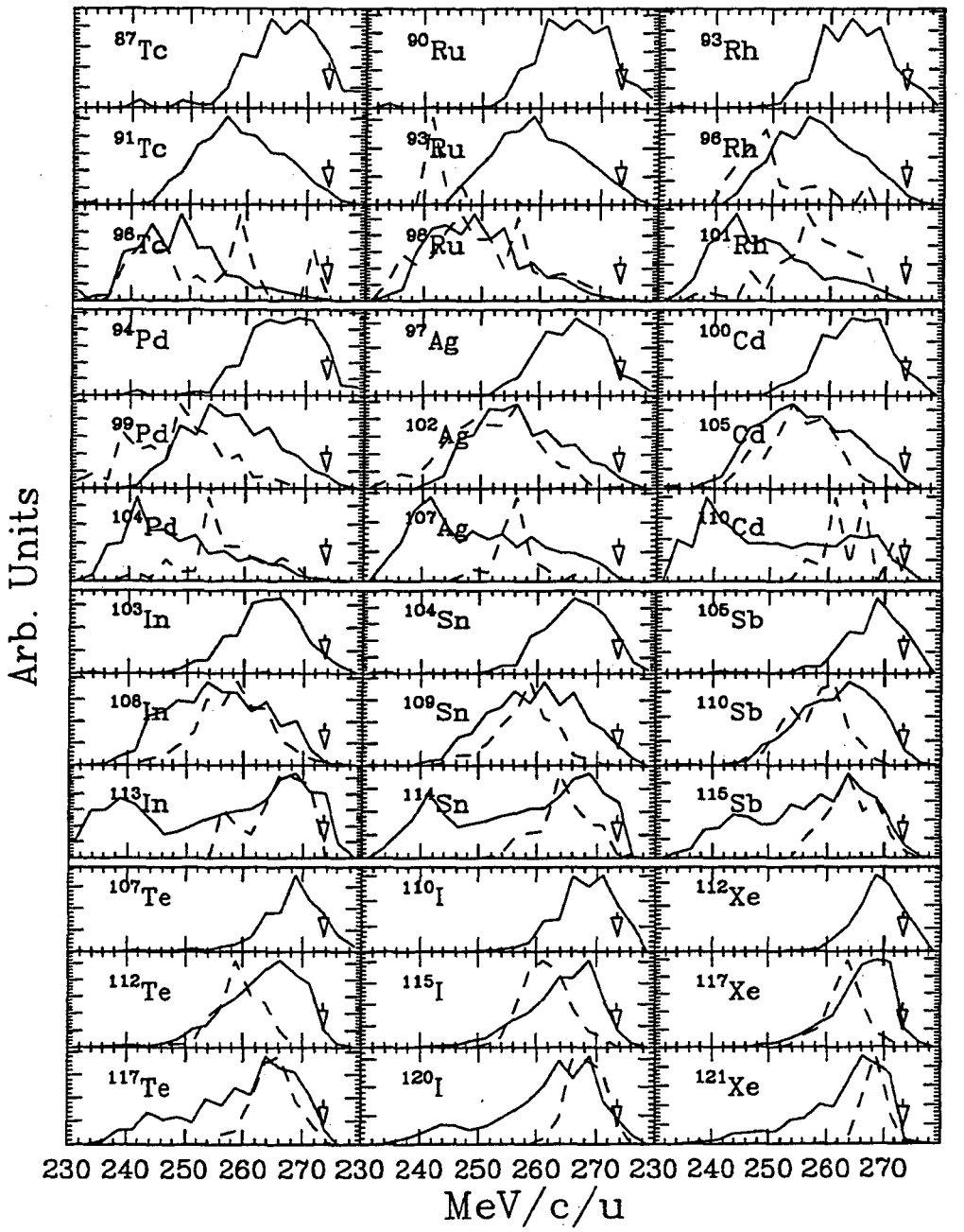

Figure A.6: The continuous curves are momentum distributions for representative light, medium, and heavy isotopes of all elements from the 40 MeV/nucleon ^{129}Xe+Al reaction. The dashed curves are the results of a model calculation (see Chapter 4). The arrow is at the momentum of the beam in each frame. The momentum of the center of mass for this system is 226.2 MeV/c/u.

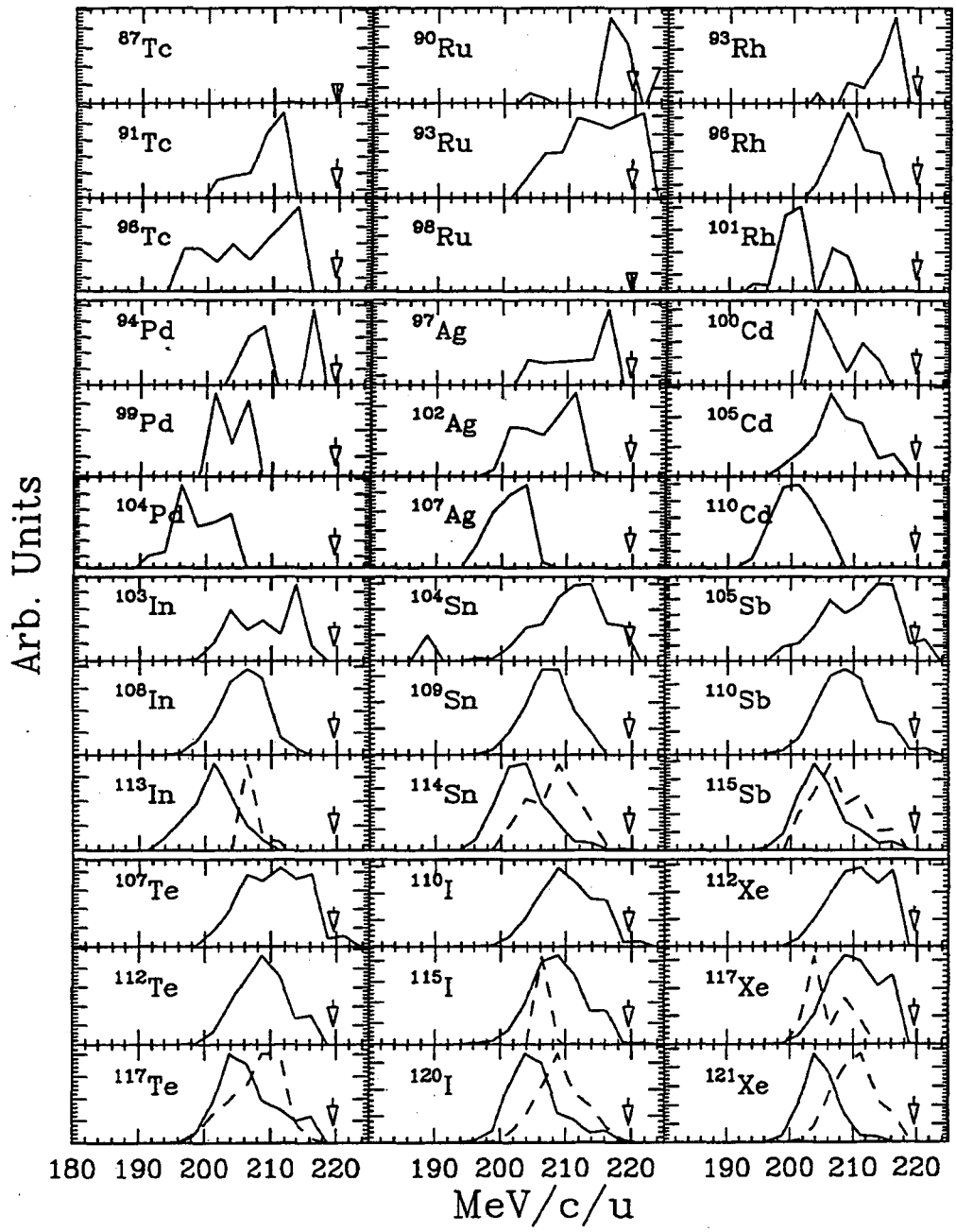

Figure A.7: The continuous curves are momentum distributions for representative light, medium, and heavy isotopes of all elements from the 26 MeV/nucleon ^{129}Xe+Be reaction. The dashed curves are the results of a model calculation (see Chapter 4). The arrow is at the momentum of the beam in each frame. The momentum of the center of mass for this system is 205.0 MeV/c/u.

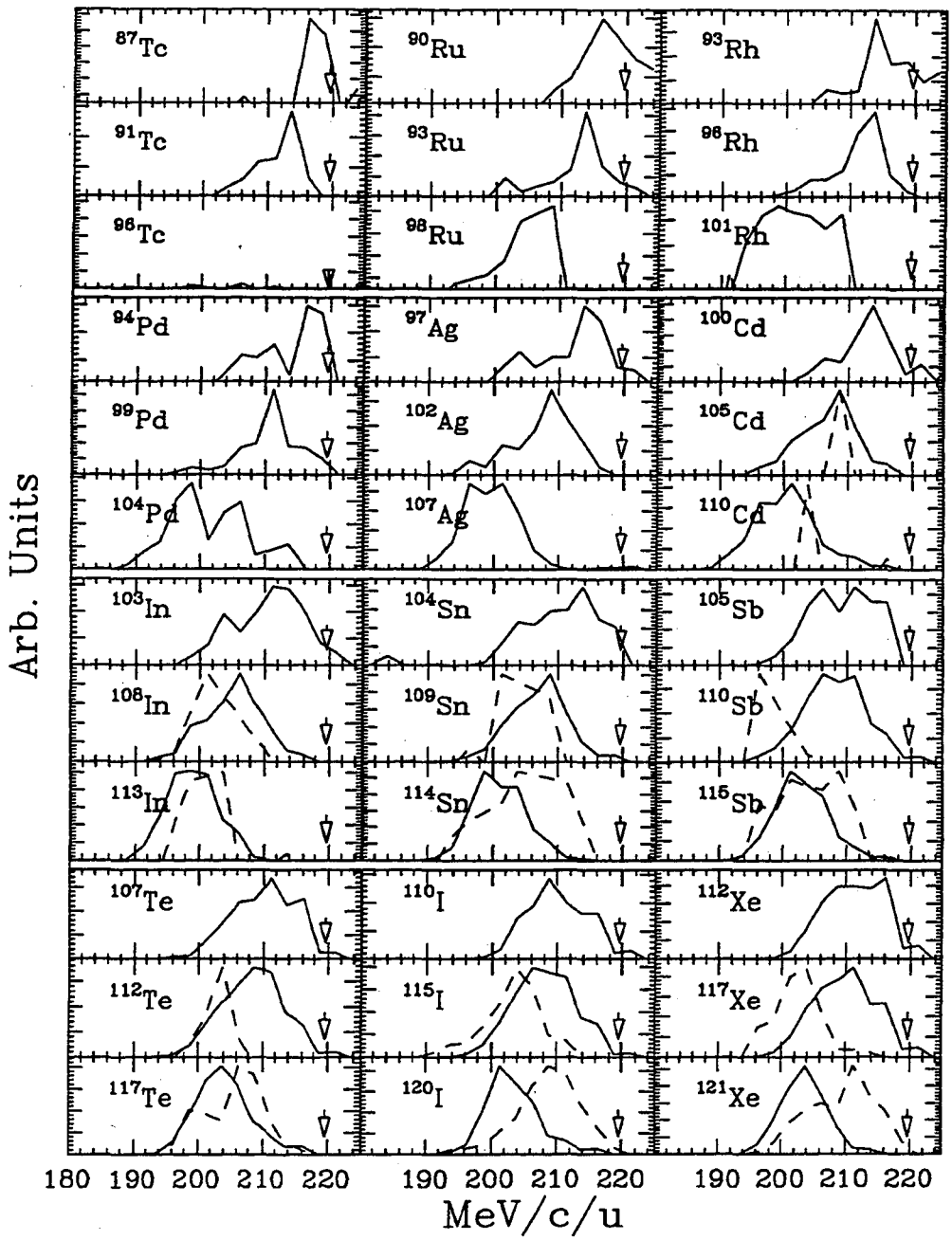

Figure A.8: The continuous curves are momentum distributions for representative light, medium, and heavy isotopes of all elements from the 26 MeV/nucleon ^{129}Xe+C reaction. The dashed curves are the results of a model calculation (see Chapter 4). The arrow is at the momentum of the beam in each frame. The momentum of the center of mass for this system is 200.9 MeV/c/u.

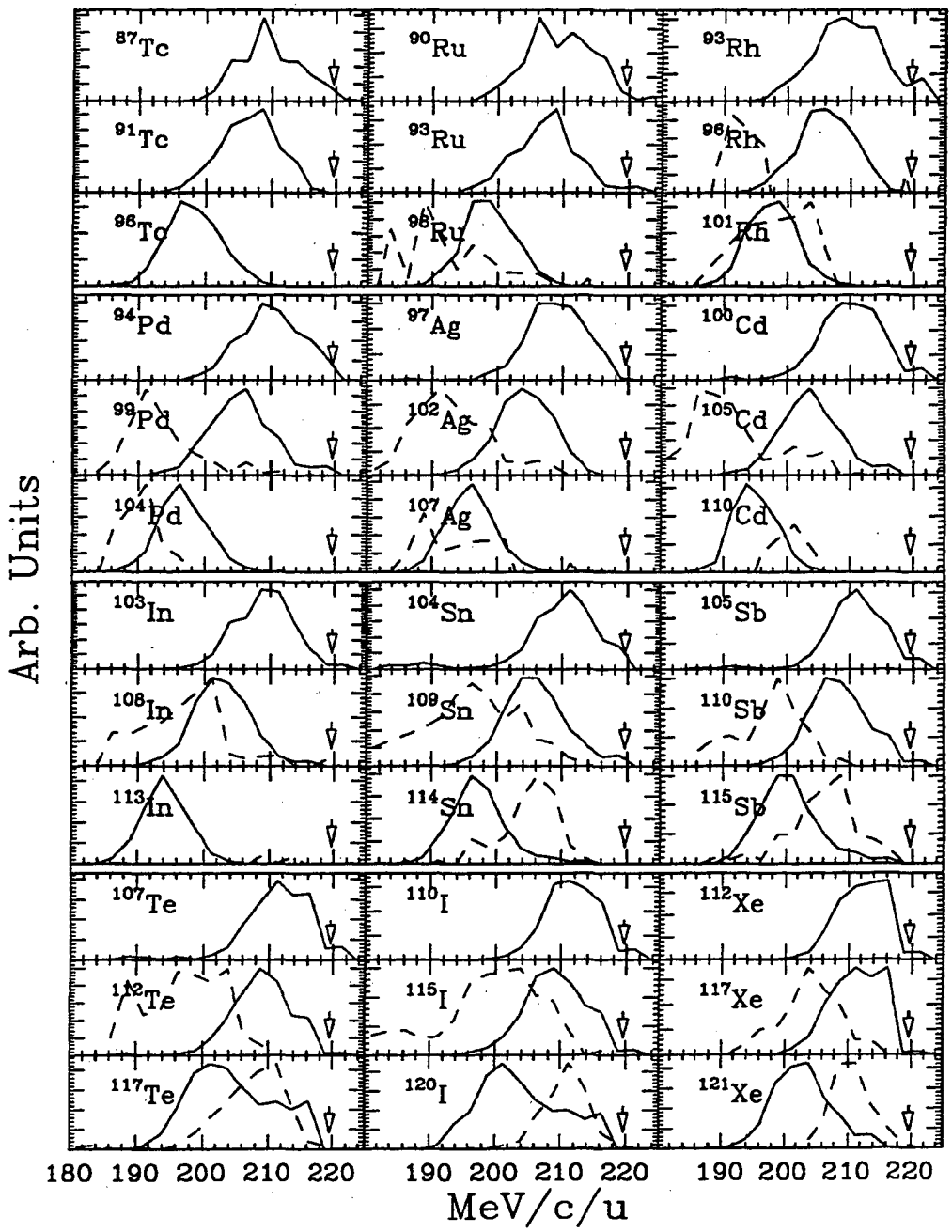

Figure A.9: The continuous curves are momentum distributions for representative light, medium, and heavy isotopes of all elements from the 26 MeV/nucleon ^{129}Xe+Al reaction. The dashed curves are the results of a model calculation (see Chapter 4). The arrow is at the momentum of the beam in each frame. The momentum of the center of mass for this system is 181.6 MeV/c/u.

References

[aug87] F. Auger, B. Berthier, A. Cunsolo, A. Foti, W. Mittig, J.M. Pascaud, E. Plagnol, J. Quebert, and J.P. Wieleczko, *Phys. Rev. C* **35**, 190 (1987).

[bab76] R. Babinet, L.G. Moretto, J. Galin, R. Jared, J. Moulton, and S.G. Thompson, *Nucl. Phys.* **A258**, 172 (1976).

[baz90] D. Bazin et al., *Nucl. Phys.* **A515**, 349 (1990).

[bec89] C. Beck et al., *Phys. Rev. C* **39**, 2202 (1989).

[ber88] G.F. Bertsch and S. Das Gupta, *Phys. Rep.* **160**, 189 (1988) and references contained therein.

[ber84] G.F. Bertsch et al., *Phys. Rev. C* **29**, 673 (1984).

[bet36] H.A. Bethe, *Phys. Rev.* **50**, 332 (1936).

[bir83] J.R. Birkelund and J.R. Huizenga, *Annl. Rev. Nucl. Part. Phys.* **33**, 265 (1983) and references therein.

[blu91] Y. Blumenfeld et al., *Phys. Rev. Lett.* **66**, 576 (1991).

[boh69] A. Bohr and B. Mottleson, Nuclear Structure, vol. 1, Benjamin, NY. (1969).

[boh39] N. Bohr and J.A. Wheeler, *Phys. Rev.* **56**, 426 (1939).

[bon90a] A. Bonasera, G.F. Burgio, and M. DiToro, *Phys. Lett.* **B221**, 233 (1989)

[bon90b] A. Bonasera, G. Russo, and H.H. Wolter, *Phys. Lett.* **B246**, 337 (1990).

[bor88] B. Borderie, M. Montoya, M.F. Rivet, D. Jouan, C. Cabot, H. Fuchs, D. Gardes, H. Gauvin, D. Jacquet, and F. Monnet, *Phys. Lett.* **B205**, 26 (1988).

[bou88] R. Bougault et al., *Nucl. Phys.* **A488**, 255c (1988).

[bou87] R.Bougault, D. Horn, C.B. Chitwood, D.J. Fields, C.K. Gelbke, D.R. Klesch, W.G. Lynch, M.B. Tsang, and K. Kwiatkowski, *Phys. Rev. C* **36**, 830 (1987).

[bow92] D.R. Bowman et al., *Phys. Rev. C* **46**, 1824 (1992).

[bow91a] D.R. Bowman et al., *Nucl. Phys.* **A523**, 386 (1991).

[bow91b] D.R. Bowman et al., *Phys. Rev Lett.* **67**, 1527 (1991).

[bow89] D.R. Bowman, Thesis, University of California at Berkeley, Lawrence Berkeley Laboratory report number LBL-27691 (1989).

[bow73] J.D. Bowman, W.J. Swiatecki, and C.E. Tsang, Lawerence Berkeley Laboratory report LBL-2908 (1973).

[cha88a] R.J. Charity et al., *Nucl. Phys.* **A483**, 371 (1988).

[cha88b] R.J. Charity, D.R. Bowman, Z.H. Liu, R.J. McDonald, M.A. McMahan, G.J. Wozniak, L.G. Moretto, S. Bradley, W.L. Kehoe, and A.C. Mignerey, *Nucl. Phys.* **A476**, 516 (1988).

[cha90] R.J. Charity et al., *Nucl. Phys.* **A511**, 59 (1990).

[chi83] C. Chitwood, D.J. Fields, C.K. Gelbke, W.G. Lynch, A.D. Panagiotou, M.B. Tsang, H. Utsunomiya, and W.A. Freidman, *Phys. Lett.* **B131**, 289 (1983).

[chu91] Y.H. Chung, S.Y. Cho, and N.T. Porile, *Nucl. Phys.* **A533**, 170 (1991).

[col93] N. Colonna, private communication (1993).

[col92a] M. Colonna, P. Roussel-Chomaz, N. Colonna, M. Di Toro, L.G. Moretto, and G.J. Wozniak, *Phys. Lett.* **283**, 180 (1992).

[col92b] M. Colonna, M. Di Toro, V. Lataora, and N. Colonna, *Nucl. Phys.* **A545**, 111 (1992) and *Nucl. Phys.* **A541**, 295 (1992).

[col89] N. Colonna et al., *Phys. Rev. Lett.* **62**, 1833 (1989).

[cus93] D. Cussol et al., *Nucl. Phys.* **A561**, 561 (1993).

[day86] R. Dayras et al., *Nucl. Phys.* **A460**, 299 (1986).

[dav85] K.T. Davies and A.J. Sierk, *Phys. Rev. C* **31**, 915 (1985).

[del91] D.N. Delis et al., *Nucl. Phys.* **A534**, 403 (1991).

[des91] R.T. de Souza et al., *Phys. Lett.* **B268**, 6 (1991).

[dur92] D.O. Durand et al., *Nucl. Phys.* **A541**, 266 (1992).

[eth91] T. Ethvignot et al., *Phys. Rev. C* **43**, R2035 (1991).

[fat87] M. Fatyga et al., *Phys. Rev. Lett.* **58**, 2527 (1987).

[fie89] D.E. Fields et al., *Phys. Lett.* **B220**, 356 (1989).

[fie84] D.J. Fields, W.G. Lynch, C.B. Chitwood, C.K. Gelbke, M.B. Tsang, H. Utsunomiya, and J. Aichelin, *Phys. Rev. C* **30**, 1912 (1984).

[fox89] R. Fox, R. Au, and A. VanderMolen, *IEEE Trans. Nucl. Sci.* **36**, 1562 (1989).

[gal75] J. Galin, *Nucl. Phys.* **A255**, 472 (1975).

[gai91] J.J. Gaimard and K.H. Schmidt, *Nucl. Phys.* **A531**, 709 (1991) and references therein.

[gil92] G.P. Gilfoyle et al., *Phys. Rev. C* **46**, 265 (1992).

[gon87] A. Gonin et al., *Phys. Lett.* **B217**, 406 (1987).

[gos77] J. Gosset, H.H. Gutbrod, W.G. Mayer, A.M. Poskanzer, A. Sandoval, R. Stock, and G.D. Westfall, *Phys. Rev. C* **16**, 629 (1977).

[gos50] S.N. Goshal, *Phys. Rev.* **80**, 939 (1950).

[hag88] A. Hagel et al., *Nucl. Phys.* **A486**, 424 (1988).

[han89] H.Y. Han, K.X. Jing, E. Plagnol, D.R. Bowman, R.J. Charity, L. Vinet, G.J. Wozniak, and L.G. Moretto, *Nucl. Phys.* **A492**, 138 (1989).

[han93] K. Hanold, L.G. Moretto, G.F. Peaslee, G.J. Wozniak, D.R. Bowman, M.F. Mohar, and D.J. Morrissey, *Phys. Rev. C* **48**, 723 (1993).

[hau52] H. Hauser and H. Feshbach, *Phys. Rev.* **87**, 336 (1952).

[hub80] F. Hubert, A. Fleury, R. Bimbot, and D. Gardes, *Ann. de Physique* **5**, 1 (1980).

[hui77] J.R. Huizenga and W.U. Schroeder, *Annl. Rev. Nucl. Part. Phys.* **27**, 465 (1977) and references therein.

[hyd71] E.K. Hyde, G.W. Butler, and A.M. Poskanzer, *Phys. Rev. C* **4**, 1759 (1971).

[jac83] B.V. Jacak, G.D. Westfall, C.K. Gelbke, L.H. Harwood, W.G. Lynch, D.K. Scott, H. Stoker, M.B. Tsang, and T.J.M. Symons, *Phys. Rev. Lett.* **51**, 1846 (1983).

[jin94] K.X. Jing, private communication, work being written for publication (1994).

[keh89] W.L. Kehoe, Thesis, Univ. of Maryland, report number DOE/ER/40321-5 (1989).

[kin91] Y.D. Kin et al., *Phys. Rev Lett.* **67**, 14 (1991).

[kor73] R.G. Korteling, C.R. Toren, and E.K. Hyde, *Phys. Rev. C* **7**, 1611 (1973).

[kra79] H.J. Krappe, J.R. Nix, and A.J. Sierk, *Phys. Rev. C* **20**, 992 (1979).

[lew93] M. Lewitowicz et al., *Nouvelles du GANIL* **48**, 7 (1993).

[lle88] A. Lleres, Thesis, L'University Scientifique Technologique et Medicale de Grenoble (1988).

[lot92] B. Lott et al., *Phys. Rev. Lett.* **68**, 3141 (1992).

[lov87] W. Loveland, K. Aleklett, L. Shiver, Z. Xu, and G.T. Seaborg, "Formation of Large Target Residues in Intermediate Energy Nuclear Collisons", preprint LBL-23365 (1987).

[lyn82] U. Lynen et al., *Nucl. Phys.* **A387**, 129c (1982).

[mal91] A. Malki et al., *Z. für Phys.* **339**, 283 (1991).

[mcm85] M.A. McMahan, L.G. Moretto, M.L. Padgett, G.J. Wozniak, L.G. Sobotka, and M.G. Mustafa, *Phys. Rev. Lett.* **54**, 1995 (1985).

[mcm86] M.A. McMahan et al., *Nucl. Instr. Meth.* **A253**, 1 (1986).

[mey80] W.G. Meyer, H.H. Gutbrod, C. Lukner, and A. Sandoval, *Phys. Rev. C* **22**, 179 (1980).

[mil53] J.M. Miller and G. Friedlander, *Phys. Rev.* **91**, 485 (1953).

[moh91] M.F. Mohar et al., *Phys. Rev. Lett.* **66**, 1571 (1991).

[mol81] P. Möller and J.R. Nix, *Nucl. Phys.* **A361**, 117 (1981).

[mor94] D.J. Morrissey, private communication.

[mor93] L.G. Moretto and G.J. Wozniak, *Ann. Rev. Nuc. Part. Sci.*, **43** 379 (1993) and references therein.

[mor92] L.G. Moretto, Kin Tso, N. Colonna, and G.J. Wozniak, *Phys. Rev. Lett.* **69**, 1884 (1992).

[mor88] L.G. Moretto and G.J. Wozniak, *Prog. Part. Nucl. Phys.* **21**, 401 (1988) and references therein.

[mor86] L.G. Moretto and D.R. Bowman, *Proceedings of the XXIV International Winter Meeting on Nuclear Physics, Bormio, Italy, I. Iori, ed., Ricerca Scientifica ed Educazione Permanente*, **49**, 126 (1986).

[mor81] L.G. Moretto and R.P. Schmitt, *Rep. Prog. Phys.* **44**, 533 (1981).

[mor78] D.J. Morrissey, W.R. Marsh, R.J. Otto, W. Loveland, and G.T Seaborg, *Phys. Rev. C* **18**, 1267 (1978).

[mor75] L.G. Moretto, *Nucl. Phys.* **A247**, 211 (1975).

[mor72] L.G. Moretto, *Phys. Lett.* **B40**, 185 (1972).

[oli79] L.F. Oliveira, R. Donangelo, and J.O. Rasmussen, *Phys. Rev. C* **19**, 826 (1979).

[orr92] N.A. Orr et al., *Phys. Rev. Lett.* **69**, 2050 (1992).

[pha92] L. Phair et al., *Phys. Lett.* **B285**, 10 (1992).

[pea93] G.F. Peaslee, private communication (1993).

[pla91] E. Plasecki et al., *Phys. Rev. Lett.* **66**, 1291 (1991).

[pla89] E. Plagnol et al., *Phys. Lett.* **B221**, 11 (1989).

[pos71] A.M. Poskanzer, G.W. Butlet, and E.K. Hyde, *Phys. Rev. C* **3**, 882 (1971).

[riv88] M.F. Rivet, B. Borderie, C. Gregoire, D. Jouan, and B. Remaud, *Phys. Lett.* **B215**, 55 (1988).

[rou93] P. Roussel-Chomaz et al., *Nucl. Phys.* **A551**, 508 (1993).

[rud66] G.Rudstam, *Z. Naturforsh* **A21**, 1027 (1966).

[sai81] M. de Saint Simon et al., *Phys. Rev. C* **26**, 2447 (1982).

[sie89] R.H. Siemssen "Incomplete Fusion Reactions at Low and Intermediate Energies." Preprint KVI-809, Kernfysisch Versneller Instituut (1989).

[sie86] A.J. Sierk, *Phys. Rev. C* **33**, 2039 (1986).

[she90] B.M. Sherrill, W. Benenson, D. Mikolas, D.J. Morrissey, J.A. Nolen Jr, and J.A. Winger, Proceedings of the Internaional Conference on Accelerator Applications, Denton, Texas, *Nucl. Instr. Meth.* Nov. 1990. See also Radioactive Nuclear Beams, The First International Confernce, W.D. Myers, J.M. Nitschke, and E.B. Norman, eds. Berkeley, Ca., Oct. 1989, World Scientific Publishing, p. 72.

[she93] B.M. Sherrill, private communication (1993).

[sob83] L.G. Sobotka, M.L. Padgett, G.J. Wozniak, G. Guarino, A.J. Pacheco, L.G. Moretto, Y. Chan, R.G. Stokstad, I. Tserruya, and S. Wald, *Phys. Rev. Lett.* **51**, 2187 (1983).

[sob84] L.G. Sobotka, M.A. McMahan, R.J. McDonald, C. Signarbieux, G.J. Wozniak, M.L. Padgett, J.H. Gu, Z.H. Liu, Z.Q. Yao, and L.G. Moretto, *Phys. Rev. Lett.* **53**, 2004 (1984).

[sug54] N. Sugarman, R.B. Duffeild, G. Friedlander, and J.M. Miller, *Phys. Rev.* **95**, 1704 (1954).

[tas91] L. Tassan-Got et al., *Nucl. Phys.* **A524**, 121 (1991).

[tas93] L. Tassan-Got, private comunication (1993).

[tsa85] M.B. Tsang et al., *Phys. Rev. C* **40**, 1685 (1989).

[vaz84] L. Vaz and J.M. Alexander, *Z. Phys.* **A318**, 231 (1984).

[vio89] V.E. Viola, *Nucl. Phys.* **A502**, 531 (1989) and references therein.

[vie84] D.J. Vieira, G.W. Butler, J.M. Wouters, and D.S. Brenner, *Annual Report Progress at LAMPF* p.192 (1984).

[vin90] M.F. Vineyard et al., *Phys. Rev. C* **41**, 1005 (1990).

[wei37] V.F. Weisskopf, *Phys. Rev.* **52**, 195 (1937).

[wes76] G.D. Westfall, R.G. Sextro, A.M. Poskanzer, A.M. Zebelman, G.W. Butler, and E.K. Hyde, *Phys. Rev. C* **17**, 1368 (1978).

[whe63] J.A. Wheeler, Fast Neutron Physics, Vol II, Interscience, New York, p. 2051 (1963).

[wil92] J.L. Wile et al., *Phys. Rev. C* **45**, 2300 (1992).

[wil91] J.L. Wile et al., *Phys. Lett.* **B264**, 26 (1991).

[wil80] W.W. Wilcke, J.R. Birkelund, A.D. Hoover, J.R. Huizenga, W.U. Schröder, and H.J. Wollersheim, UR-NSRL-221, University of Rochester, Nuclear Structure Research Laboratory.

[wol56] R. Wolfgang, E.W. Baker, A.A. Caretto, J.B. Cumming, G. Friedlander, and J. Hudis, *Phys. Rev.* **103**, 394 (1956).

[yen92] S.J. Yennello, J.A. Winger, T. Antaya, W. Benenson, M.F. Mohar, D.J. Morrissey, N.A. Orr, and B.M. Sherrill, *Phys. Rev. C* **46**, 2620 (1992).

[win93] J.A. Winger et al., *Phys. Rev. C* **48**, 3097 (1993).

[zah91] M. Zahar et al., *Z. Für Phys.* **339**, 465 (1991).

[zeb75] A.M. Zebelman, A.M. Poskanzer, J.D. Bowman, R.G. Sextro, and V.E. Viola, *Phys. Rev. C* **11**, 1280 (1975).

LAWRENCE BERKELEY LABORATORY
UNIVERSITY OF CALIFORNIA
TECHNICAL INFORMATION DEPARTMENT
BERKELEY, CALIFORNIA 94720